COO-1112-3

THE UNIVERSITY OF MICHIGAN
COLLEGE OF LITERATURE, SCIENCE, AND THE ARTS
Department of Physics

Technical Report

FOUR- AND FIVE-PARTICLE PRODUCTION IN 3.7 BeV/c π^-p COLLISIONS

William D. C. Moebs, III

ORA Project 04938

under contract with:

U. S. ATOMIC ENERGY COMMISSION
CHICAGO OPERATIONS OFFICE
CONTRACT NO. AT(11-1)-1112
ARGONNE, ILLINOIS

administered through:

OFFICE OF RESEARCH ADMINISTRATION ANN ARBOR

September 1965

This report was also a dissertation submitted in partial fulfillment of the requirements for the degree of Doctor of Philosophy in The University of Michigan, 1965.

TABLE OF CONTENTS

TABLE OF CONTENTS (Concluded)

LIST OF TABLES

LIST OF FIGURES

LIST OF FIGURES (Continued)

LIST OF FIGURES (Concluded)

ABSTRACT

In an exposure of the BNL 20-inch hydrogen bubble chamber to a 3.7 π^- beam, 805, 1025, and 489 events of the reaction type: (1) $\pi^- + p \rightarrow \pi^- + \pi^- + \pi^+ + p$, (2) $\pi^- + p \rightarrow \pi^- + \pi^- + \pi^+ + p + \pi^\circ$, and (3) $\pi^- + p \rightarrow \pi^- + \pi^- + \pi^+ + \pi^+ + n$, respectively, have been observed. The two-three- and four-body mass spectra have been studied in a search for short-lived resonant states involving the various particle combinations.

In reaction (1) there are peaks corresponding to the ρ°, the 1238 and 1512 MeV isobars, and the A_1 and A_2 mesons. It is found that both the ρ° and the 1238 MeV isobar channels can be analyzed by means of the one-pion-exchange model, and consequently, the pion-pion interaction is studied for both.

Reaction (2) is found to be dominated by ρ^- and ω° production. It is observed that both of these mesons are produced in conjunction with nucleon isobars. The ρ^- channel furnishes examples of the higher nucleon isobars decaying into a pion and the 1238 MeV (π^+,p) resonance, which in turn breaks up into a π^+ and a p. A peak is also found in the (π^-,ω°) mass spectrum at 1250 MeV, but serious questions are raised about its interpretation as a (π^-,ω°) resonance.

Cross sections for the three reactions and the various resonance channels are also presented.

CHAPTER I

INTRODUCTION

1. INTRODUCTORY REMARKS

During the past four years a vast amount of high-energy physics research has been devoted to the search for and the investigation of resonant states existing between the elementary particles. In this short period of time experimenters have discovered approximately thirty resonances, many of which have more than one charge state.

The first elementary particle resonance was discovered in 1952 when it was found that the pion-proton elastic scattering cross section goes through a broad maximum centered at a beam momentum of approximately 200 MeV.[1] This resonance, which is called the N*(1238), has since been found in multiparticle production by examining the invariant mass plots of the pion-proton system.

In the years from 1952 to 1960, with the exception of pion-nucleon elastic scattering studies, there was virtually no work done in the field of resonance production. Then in 1960, while analyzing the reaction

$$K^- + p \rightarrow \Lambda^\circ + \pi^- + \pi^+, \qquad (1.1)$$

Alston et al.,[2] found that the (π,Λ) system forms a resonant state at 1385 MeV. A short time later two meson resonances, the ρ° and ω°, were discovered by many different groups.[3-6] The search for both of

these was inspired by their predicted existence in order to explain the charge structure of the nucleon.[7-9]

Since these initial discoveries many additional resonant states have been found. These include the η°, various pion-nucleon states, the A and B mesons, and many others. For a complete list of all elementary particles and resonant states known at this time, the reader is referred to a recent article in Reviews of Modern Physics.[10]

Along with the ever-increasing list of new particles, many theoretical models have been brought forth in an attempt to explain resonance production.[11-13] These have been somewhat confined to elastic scattering and single-pion production processes such as

$$\pi^- + p \rightarrow \pi^- + \pi^+ + n, \tag{1.2}$$

and no decent explanation of multiple-particle processes has been formulated. It is of interest, therefore, to attempt to relate the many-particle states to simpler two- and three-body states. If this simplification can be made, it is then possible to apply the existing theoretical models to these higher multiplicities. This has been done with some success by J. Alitti et al.,[14] and N. Schmitz[15] who were able to study the (π^-,π^-) interaction by applying the one-pion-exchange model (see the Feynam diagram of Figure 1(a)) to the reaction

$$\pi^- + p \rightarrow \pi^- + \pi^- + N^*_{3,3} \rightarrow \pi^+ + p. \tag{1.3}$$

Also, a recent refinement of the meson-exchange models to include

absorptive effects arising from coupling between different channels[16,17] is now being tested in various experiments. This version of the ρ^--exchange model (see Figure 1(b)) has been applied to ω° production in the reaction

$$\begin{aligned} \pi^+ + n &\rightarrow p + \omega^\circ \\ &\rightarrow \pi^- + \pi^+ + \pi^\circ \end{aligned} \qquad (1.4)$$

and gives good estimates of the production cross section and decay properties of the ω°.[18]

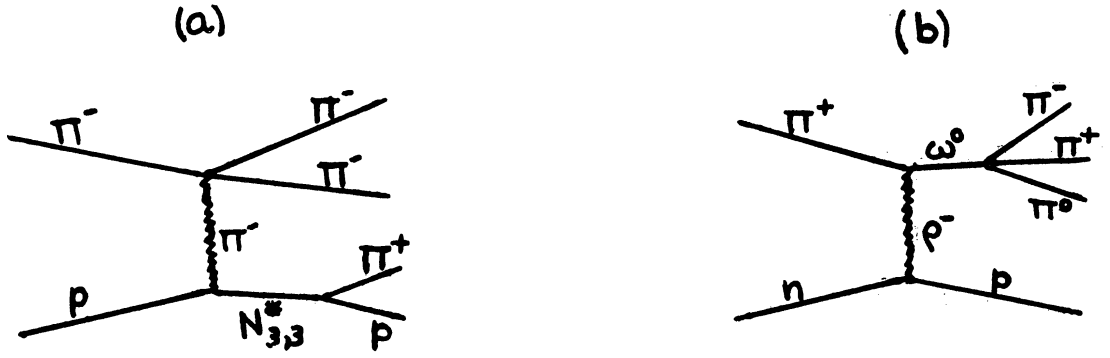

Figure 1. One-meson-exchange diagrams for (a) $\pi^- + p \rightarrow \pi^- + \pi^- + N^*_{3,3}$ and (b) $\pi^+ + n \rightarrow p + \omega^\circ$.

In addition to the dynamical models for particle production, many mass schemes and formulas have been proposed which attempt to place the particles in some systematic pattern.[19,20] Since there is no real understanding of the strong interaction, a basic assumption that nature choses her mass states in some well-ordered manner underlies all of these classification methods. At the present time the most promising of these is the "eightfold way" (SU3)[21,22] which is based on the mathematical properties of Lie algebras and Lie groups. This system places particles of the same spin and parity into a group and then

conjectures a mass formula connecting the members of the group. So far, multiplets consisting of one, eight, and ten members have been described quite accurately by SU3. Undoubtedly, the theory's most striking success is the experimental confirmation of the baryon decuplet with the spin-parity assignment $J^{p} = 3/2^{+}$. At the time that SU3 was introduced, only the quartet (the 1238 MeV $N^{*}_{3,3}$) and the Σ triplet (the 1385 MeV($\pi\Lambda$) resonance of Alston et al. [2]) had been seen. Since the mass rule predicts approximately equal mass intervals between the members of the group, there should be a $\equiv$ doublet at 1530 MeV and an Ω^{-} singlet, which is stable under strong and electromagnetic interactions, at 1676 MeV (see Figure 2). These have both been found[23,24] and furnish striking evidence of the eightfold way's validity—even though the spin and parity of the Ω^{-} have not yet been measured.

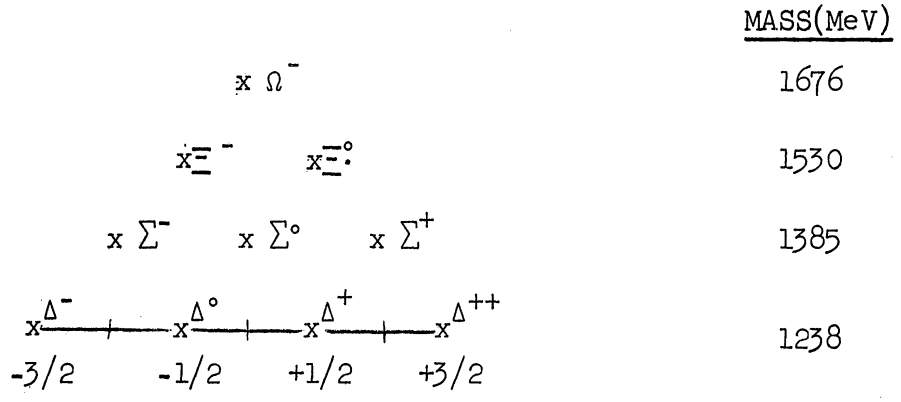

Figure 2. The $J=3/2^{+}$ decuplet with mass represented by the vertical axis and the Z component of isotopic spin represented by the horizontal axis.

The formalism of the eightfold way satisfies the rules of a Lie algebra which has eight independent quantum numbers. These eight

quantities are the hypercharge Y, the three components of isotopic spin I, and four other symmetries which have not yet been identified with known observables. The basic assumption of SU3 is that the strong interaction can be divided into two parts—one preserves all eight symmetries, and the other violates the symmetries associated with the four new quantum numbers while preserving Y and I. If there weren't this symmetry breaking, all strongly interacting particles of a spin—parity multiplet would have the same mass; a given group just represents different states of the same particle.

A simple but instructive analogue to SU3 is furnished by the properties of the spinless hydrogen atom. The rotational invariance of this system is characterized by the conservation of angular momentum L and can be expressed mathematically by the rules of the Lie algebra for the group called SU2. When the atom is placed in a Z-directed magnetic field B_Z, only the symmetries associated with the Z direction are preserved ($[H,L_i] \neq 0$, unless $L_i = L_Z$), and additionally, the energy degeneracy associated with a given angular momentum state is broken. The similarity with SU3 is quite clear if one associates the unperturbed Hamiltonian with the particle mass operator, the perturbing term B_Z with the mass splitting, L with the set of new quantum numbers, and L_Z with the set {Y,I}. Just as the magnetic field destroys most of the rotational symmetry and causes energy splitting in the atom, some part of the strong interaction executes an analogous influence on the symmetries and mass states of the SU3 system.

2. AREA OF INVESTIGATION

The purpose of this report is to discuss the results of a detailed study of certain pion-pion and pion-nucleon resonances found in a hydrogen bubble chamber experiment. Sixty-thousand pictures were taken in the Schutt 20-inch chamber using a 3.7 BeV/c separated π^- beam. The reactions

$$\pi^- + p \rightarrow \pi^- + \pi^- + \pi^+ + p, \tag{1.5}$$

$$\rightarrow \pi^- + \pi^- + \pi^+ + p + \pi^\circ, \tag{1.6}$$

and

$$\rightarrow \pi^- + \pi^- + \pi^+ + \pi^+ + n \tag{1.7}$$

are considered here. The complete results on the reactions

$$\pi^- + p \rightarrow \pi^- + \pi^+ + n, \tag{1.8}$$

$$\rightarrow \pi^- + \pi^\circ + p, \tag{1.9}$$

$$\rightarrow \pi^- + p, \tag{1.10}$$

plus preliminary results on both types have been reported elsewhere.[25-31]

Reaction (1.5) is found to be dominated by resonance production, with only 22% of the events not having at least one mass value in either the $N^*_{3,3}(1238)$ or ρ° peak. The production of these two resonances is represented by the reactions

$$\pi^- + p \rightarrow \pi^- + \pi^- + N^*_{3,3}(1238) \tag{1.11}$$

$$\rightarrow \pi^+ + p$$

*The notation $N^*_{i,j}(1238)$ will be used throughout the text and represents a nucleon isobar of mass 1238 MeV with total isotopic spin i/2 and Z component j/2.

and

$$\pi^- + p \rightarrow \pi^- + p + \rho^\circ \qquad (1.12)$$
$$\rightarrow \pi^- + \pi^+.$$

Both (1.11) and (1.12) are found to occur by means of a single-pion-exchange process,[11] and therefore, a detailed analysis of the upper verticies in Figures 3(a) and 3(b) is undertaken.

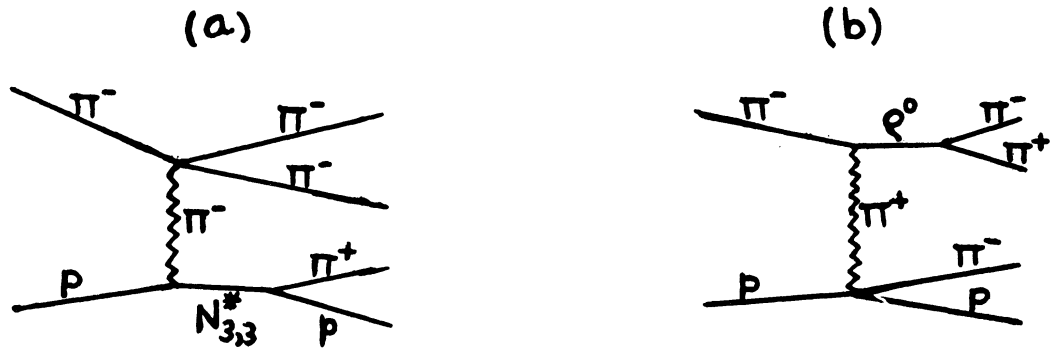

Figure 3. One-pion-exchange diagrams for (a) reaction (1.11) and (b) reaction (1.12).

The pion-pion vertex is analyzed by means of a partial wave expansion for both, and with the aid of the Chew-Low[32] method and reaction (1.11), the (π^-,π^-) cross section is determined as a function of center-of-mass energy. It is also found that the ρ° is frequently produced in two-body final states via the modes

$$\pi^- + p \rightarrow \rho^\circ + N^*_{3,-1}(1238) \qquad (1.13)$$
$$\rightarrow \pi^- + p,$$

$$\rightarrow \rho^\circ + N^*_{1,-1}(1512) \qquad (1.14)$$
$$\rightarrow \pi^- + p,$$

$$\rightarrow p + A_1 \qquad (1.15)$$
$$\rightarrow \rho^\circ + \pi^-,$$

and

$$p + A_2 \qquad (1.16)$$
$$\rightarrow \rho^\circ + \pi^-.$$

In reaction (1.6) a large fraction of the events involve the production of the ω° and ρ^- mesons through the processes

$$\pi^- + p \rightarrow \pi^- + p + \omega^\circ \qquad (1.17)$$
$$\rightarrow \pi^- + \pi^+ + \pi^\circ$$

and

$$\rightarrow \pi^- + \pi^+ + p + \rho^- \qquad (1.18)$$
$$\rightarrow \pi^- + \pi^\circ.$$

Again two-body final states are prominent, with a significant number of events belonging to the channels

$$\pi^- + p \rightarrow \omega^\circ + N^*_{3,-1}(1238) \qquad (1.19)$$
$$\rightarrow \pi^- + p,$$

$$\rightarrow \omega^\circ + N^*_{1,-1}(1512) \qquad (1.20)$$
$$\rightarrow \pi^- + p,$$

$$\rightarrow \omega^\circ + N^*_{1,-1}(1688) \qquad (1.21)$$
$$\rightarrow \pi^- + p,$$

$$\rightarrow \rho^- + N^*_{1,1}(1512) \qquad (1.22)$$
$$\rightarrow \pi^- + N^*_{3,3}(1238)$$
$$\rightarrow \pi^+ + p,$$

$$\rightarrow \rho^- + N^*_{1,1}(1688) \qquad (1.23)$$
$$\rightarrow \pi^- + N^*_{3,3}(1238)$$
$$\rightarrow \pi^+ + p,$$

and

$$\rightarrow \rho^- + N^*_{3,1}(1920) \qquad (1.24)$$
$$\rightarrow \pi^- + N^*_{3,3}(1238)$$
$$\rightarrow \pi^+ + p.$$

In the (ω°,π^-) mass plot an enhancement appears at approximately 1250 MeV which corresponds to the B meson. It will be seen, however, that there are very serious questions about this peak which make its inter-

pretation very indefinite.

The analysis of (1.7) does not show the prolific resonance production that characterizes the other two reactions. There is a strong peak in the (π^-,n) system due to the reaction

$$\pi^- + p \quad \pi^- + \pi^+ + \pi^+ + N^*_{3,-3}(1238) \quad (1.25)$$
$$\rightarrow \pi^- + n,$$

but this is the only resonant state found.

Other pion-proton experiments[33-39] of this type have been performed at various beam momenta in the range 2-5 BeV/c. All of these see the strong ρ° and $N^*_{3,3}(1238)$ production in (1.5), the ω° peak in (1.6), and the $N^*_{3,-3}(1238)$ in (1.7). There is also general agreement on the existence of the two peaks in the (π^-,ρ°) mass plots at 1090 and 1310 MeV. The ρ^- peak in (1.6) is one serious source of disagreement between this and other experiments. All other results indicate virtually no evidence of charged ρ production in the multipion final states. Because the production and decay processes represented by reactions (1.22-1.24) are heretofore unseen, there is a definite necessity for further data, either to confirm or to destroy this result.

CHAPTER II

THE EXPERIMENT AND THE DATA

1. THE BEAM

The beam used in this experiment was obtained in a parasitic run at the Brookhaven Alternating Gradient Synchrotron. A small fraction of the internal proton beam was deflected onto an aluminum target which was 0.1 inch in height, 0.25 inch wide, and 2.0 inches long. Before reaching the bubble chamber, the beam travelled 270 feet through a beam transport section, two separation stages, and a beam shaping section. At the target the beam was composed of mostly pions with less than 10% contamination due to K^- and $\bar{p}$.[39] After the two beam separation stages all but a negligible amount of the K^- and $\bar{p}$ had been eliminated, and the only contamination, the result of μ^- produced in the decays of the beam pions, was less than 4%.[40] A detailed description of the beam can be found in the reference.[41]

2. THE CHAMBER

The Schutt 20-inch hydrogen bubble chamber was used as the source of data for this experiment. The chamber is rectangular with 10 inch sides and 20 inches long, the beam entrance being on one of the 10 x 10 inch sides. There are windows on both 20 x 10 inch sides, with four fiducial marks on the front window and seven on the back window. For illumination there is a mercury arc placed behind the rear window which

flashes a short time (140 μsec for this experiment) after expansion. The light from the mercury arc is scattered off the bubbles into four cameras which are placed in front of the chamber and focused on a plane in the center of the chamber. The optical axes of the cameras are perpendicular to the front window and intersect it at the four corners of a 9 inch square. For momentum measurements and charge identification there is a 17.2 kilogauss field whose direction is perpendicular to the chamber windows. More complete descriptions of the chamber can be found elsewhere.[42,43]

3. THE SCANNING

The scanning machines project the film images directly onto a green translucent screen. Two of the three machines furnish images approximately 1.3 times life size for the hydrogen film, and the third projects an image about equal to actual size. All three machines are able to project simultaneously two views onto the screen and then superimpose one view on the other. With this device it is very easy to distinguish tracks which stop in the chamber from those which leave through either of the windows.

The scanning of the film was accomplished in the following manner:

a) All interactions within a defined fiducial volume were recorded on scan sheets. This included events with zero, two, four, and six prongs, plus one eight-prong event. If there were defining characteristics such as decaying tracks, stopping tracks, "V particles"

pointing to the interaction, gamma rays, etc., these facts were also noted on the scan sheets.

b) If the picture had more than 20 but less than 30 beam tracks, this was noted by the scanners. If the picture had more than 30 beam tracks, it was not used in order to eliminate scanning and measuring difficulties that occur because of overcrowded pictures.

c) The film was then rescanned independently by a second scanner.

d) The two scan sheets were then compared and all disagreements were recorded. The frames in which a track count had been noted by the scanners were also considered for placement on the disagreement sheets with the following set of rules:

1) If both scanners counted less than 23 tracks, the picture was considered to be acceptable.

2) If both scanners counted more than 27 tracks, the picture was considered too crowded and the events on that picture were discarded.

3) If one or both scanners had between 23 and 27 tracks, that frame was recorded on the disagreement sheet.

e) The disagreement sheets were then looked at by a physicist who decided on the proper disposal of this set of events. For the frames with a track count disagreement the physicist accepted those with 25 or less tracks, and he discarded those with more than 25 tracks.

f) Measurement sheets were then prepared for all acceptable two- and four-prong events.

The fiducial volume was defined so that an appreciable length of track could be measured. This was necessary to keep the measuring errors as small as possible. Because of the relative ease in finding four-prong events, scanning biases were not important.

4. THE MEASURING

The machines used to measure the events also project the picture image onto a green translucent screen. These machines have the same film superposition device as the scanning machines. The picture projection is more complicated, however, as the film is loaded in a horizontal plane approximately perpendicular to the screen. This requires the employment of a series of mirrors to reflect the image onto the green screen. The measuring machines have both a high and low magnification, with the high magnification furnishing an image approximately 2.6 times life size for the hydrogen film. High magnification is used for the measuring.

The measuring is accomplished by moving the stage on which the film is loaded. This causes the film image to move on the green screen, and the measurer sets on points of the film with a cross hair. The coordinates of these points are then recorded by means of a Moiré fringe counting device or a disc encoder. These coordinates are then automatically punched on IBM cards. The machines can measure to an accuracy of a few microns on the film.

After two views for each track were measured, the punched cards were then fed into an IBM program called CHECK.[44] Besides coordinate points, the cards also contained the frame number, view number, charges of the tracks, and whether the tracks stopped or not. The program did some simple checks on the data which caught and corrected many format errors. CHECK then punched out new cards in the proper format for the track reconstruction program.

5. GEOMETRY, KINEMATICS, AND EVENT IDENTIFICATION

The track reconstruction was furnished by the computer program TRED.[45] This program uses the coordinates furnished by the measurement to find the momentum and direction of each track at its point of origin.

As a first step in understanding the program, it is necessary to acquaint oneself with the physical arrangement of the chamber and cameras. Figure 4 shows a simplified version of the chamber, with just its main body, front window, and two of the four cameras depicted. A point in the chamber, e.g., a bubble, is represented by B, fiducial marks on the inside of the front window are given by F_1 and F_2, R_1 and R_2 represent light rays from B to the cameras C_1 and C_2, and I_1 and I_2 give the points of intersection of the light rays with the inside of the front window. Since the positions of C_1, C_2, F_1, and F_2 are known, it is possible to find the coordinates of B by measuring the positions of I_1 and I_2 relative to the two fiducial marks and then re-

tracing the light rays back from C_1 and C_2 until they intersect. This point of intersection is B.

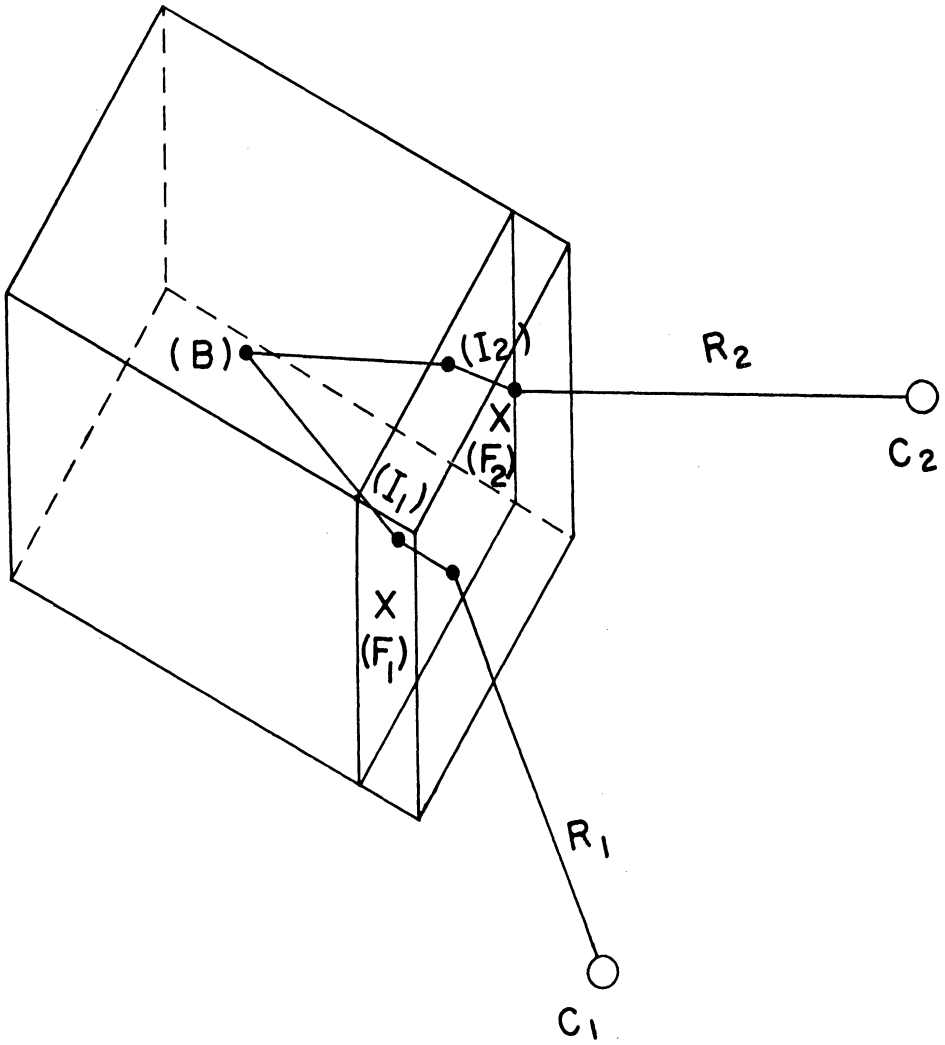

Figure 4. A simplified sketch of the bubble chamber and its cameras. F_1 and F_2 represent fiducial marks on the inside of the front glass, C_1 and C_2 represent two cameras outside the chamber, and B represents a point in the chamber. Light rays R_1 and R_2, emanating from B, enter the front glass at I_1 and I_2.

With this rather rudimentary knowledge of the optical system's physical properties, one is now able to understand the basic operations of TRED. First let the discussion be restricted to one view, e.g., that corresponding to camera C_1. By measuring the positions of F_1

and F_2 on the film, the orientation of a given coordinate system on the inside of the front glass is defined relative to the planar coordinate system of the measuring machine. This in turn defines the proper transformation for changing the machine coordinates of any measured point to the coordinates of the front glass. If the projection of point B on the film of camera C_1 is measured, this gives the coordinates of the point I_1, which can then be transformed to the chamber's front-window system. This then defines the point B as lying somewhere in the chamber along the ray R_1.

To get the actual position in the chamber of the point B, the same procedure is repeated for another view such as that of camera C_2. This defines the ray R_2. The intersection of the rays R_1 and R_2 now defines the bubble chamber coordinates of B.

So far, the problem has been restricted to a point in the chamber which can be identified on the two measured views. In an actual measurement this is very seldom the case--only when a point can be identified by some characteristic such as the end point of a stopping track. Ordinarily, there are points measured along the track on two views, none of which are corresponding. To find the momentum and direction of the track at its origin, the following steps are executed:

a) First a given track is measured in two views. With a knowledge of the fiducial-mark coordinates, these measurements define the intersections of the light rays with the front glass for both cameras (see Figure 5).

Figure 5. A given track as seen by the two cameras C_1 and C_2. The cross marks represent measured points on the tracks.

b) Circles are fit through all sets of three consecutive points on C_2.

c) A measured point on C_1 (Pc_1) is then projected parallel to the line between the cameras C_1 and C_2 onto the appropriate circle of C_2. Call this point Pc_1c_2. This point is a first approximation to the corresponding point of Pc_1.

d) Pc_1 and Pc_1c_2 are then projected back into the chamber along light rays which are constructed by using the coordinates of the cameras and the points Pc_1 and Pc_1c_2.

e) The point of closest approach is then found for the two rays. Call this point P.

f) Using the computed coordinates of P and the given coordinates of the cameras, light rays are constructed for the two measured views. Next the intersections of these rays with the front window are computed. If these intersections are found to be sufficiently close to both Pc_1 and Pc_1c_2, then P is chosen to be a point in space for the

track. If they do not agree a new value for Pc_1c_2 is tried, and this is continued until a suitable fit for the point P is found.

g) This same procedure is applied to all points on C_1. This gives a sequence of points in space corresponding to the path of the particle (see Figure 6). A parabola is then fit to these points, and errors for the fitted variables are computed.

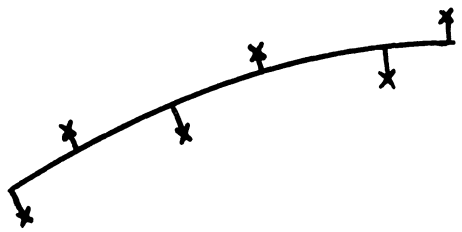

Figure 6. An example of a track fitted to the measured points in space. The deviations of the points from the fitted track define the errors in the momentum and direction.

h) For a stopping track range-energy relationships are used to compute momentum. For a particle which leaves the chamber, TRED finds momentum from curvature at the midpoint of the measured portion of the track and then computes the momentum at the track's origin by using the range-energy relationships. Since these are mass dependent, a different momentum is computed for each particle assignment.

The kinematical analysis for this experiment was handled by the Brookhaven modification of the program KICK.[45,46] This program takes the momentum and direction assignments plus their errors, assumes a mass assignment for each track, and then adjusts the track variables so that energy and momentum conservation are satisfed. The modification

is restricted to rather limited changes in the variables by requiring a small χ^2. This quantity is given by:

$$\chi^2 = \sum_{i,j=1}^{n} (X_i - X_i^m) G_{ij}^{-1} (X_j - X_j^m), \qquad \text{(II.1)}$$

where

G_{ij} = $\delta X_i \delta X_j$, a product of the errors in X_i and X_j,

X_i = the fitted value of the i'th variable,

X_i^m = the measured value of the i'th variable,

and

n = the number of measured variables.

From the definitions it is seen that the requirement of minimal changes in the track variables is equivalent to requiring a small value for χ^2. Also, because of the inverse square influence of the errors, it is clear that larger adjustments are possible for the poorly measured variables than for the well-measured variables.

Using the method of Lagrange multipliers, the fitting process can be formulated mathematically by searching for the minimum of the function

$$M(X_1 \cdots X_n, \alpha_1 \cdots \alpha_k) = \chi^2 + \sum_{j=1}^{K} \alpha_j F_j(X_1 \cdots X_n), \qquad \text{(II.2)}$$

where K = the number of constraints,

$F_j(X_1 \cdots X_n) = 0$ are the constraint equations,

and α_j = Lagrange multipliers.

For each track assignment of interest KICK finds the minimum χ^2 by means of an iterative procedure. The iteration is either stopped by

the inability to find the minimum after many steps or by a successful fit. There are, of course, many other criteria, e.g., an inconsistent missing mass, which cause an hypothesis rejection, often before the χ^2 fit is even attempted.

In this experiment all of the four-prong data was tested with the hypotheses

$$\pi^- + p \rightarrow \pi^- + \pi^- + \pi^+ + p \qquad (2.1)$$

$$\rightarrow \pi^- + \pi^- + \pi^+ + p + \pi^\circ \qquad (2.2)$$

$$\rightarrow \pi^- + \pi^- + \pi^+ + \pi^+ + n, \qquad (2.3)$$

and a large percentage of the data was also tested with the hypothesis

$$\pi^- + p \rightarrow K^+ + K^- + \pi^- + p. \qquad (2.4)$$

Because of energy and momentum conservation χ^2 for reactions (2.1) and (2.4) was minimized subject to four constraint equations (4C fit). For reactions (2.2) and (2.3), since three of the four equations were used to compute the neutral particle's momentum and direction, χ^2 was minimized subject to one constraint equation (1C fit). The maximum χ^2 allowed for the 1C and 4C fits was 5.4 and 11.7, respectively. Both of these values correspond to a χ^2 probability of 2%. Most of the χ^2 failures were due to interactions with two or more neutral particles leaving the vertex. Typical examples of this type are

$$\pi^- + p \rightarrow \pi^- + \pi^- + \pi^+ + p + \pi^\circ + \pi^\circ \qquad (2.5)$$

and

$$\pi^- + p \rightarrow \pi^- + \pi^- + \pi^+ + \pi^+ + n + \pi^\circ. \qquad (2.6)$$

These could not be fitted because of an insufficient number of constraint equations. Those events which satisfied the χ^2 test for one or more of the above hypotheses (reactions 2.1—2.4) were studied by physicists in order to make the final decision on the event type. The decision was made on the basis of bubble density.

Bubble density is defined as the number of bubbles formed per unit length by a charged track and is approximately proportional to the inverse square[47,48] of the particle's velocity. It is defined relative to the 3.7 BeV/c beam track which is arbitrarily given the value 1.0. The value used is actually the true density divided by the cosine of the track's dip angle. This corrects for the fact that bubble chamber pictures are two-dimensional and in the plane of the front window.

After the bubble density check each event was placed in one of the following categories:

a) The χ^2 test and bubble density check satisfied only one of the hypotheses (unambiguous event).

b) The χ^2 test and bubble density check satisfied two or more of the hypotheses (ambiguous event).

c) The event failed either the χ^2 test or the bubble density check (rejected event).

d) The event was self-ambiguous; i.e., the two positive tracks were acceptable as either (π^+,p) or (p,π^+).

Table I summarizes the event classification. The χ^2 distributions for the unambiguous events of reactions (2.1), (2.2), and (2.3) are shown

in Figures 7(a-c) along with the theoretical curves.[49] The distribution for reaction (2.1) also includes the ambiguous events for reasons which will be explained below.

TABLE I

EVENT CLASSIFICATION AFTER THE BUBBLE DENSITY CHECK.
THE $K^+K^-\pi^-p$ FIT WAS TRIED FOR ONLY TWO-THIRDS OF THE DATA

CATEGORY	NUMBER
$\pi^-\pi^-\pi^+p$	520
$\pi^-\pi^-\pi^+p\pi^\circ$	1021
$\pi^-\pi^-\pi^+\pi^+n$	489
$K^-K^+\pi^-p$	20
$\pi^-\pi^-\pi^+p$, $\pi^-\pi^-\pi^+p\pi^\circ$ Amb.	277
$\pi^-\pi^-\pi^+p$, $\pi^-\pi^-\pi^+\pi^+n$ Amb.	5
$\pi^-\pi^-\pi^+p\pi^\circ$, $\pi^-\pi^-\pi^+\pi^+n$ Amb.	121
$\pi^-\pi^-\pi^+p$ Self-amb.	3
$\pi^-\pi^-\pi^+p\pi^\circ$ Self-amb.	4
Rejected	1020

Those events which are ambiguous between the 4C and the 1C fits will all be considered as belonging to the 4C case in the following analysis. The reasoning behind this selection is based on the following results:

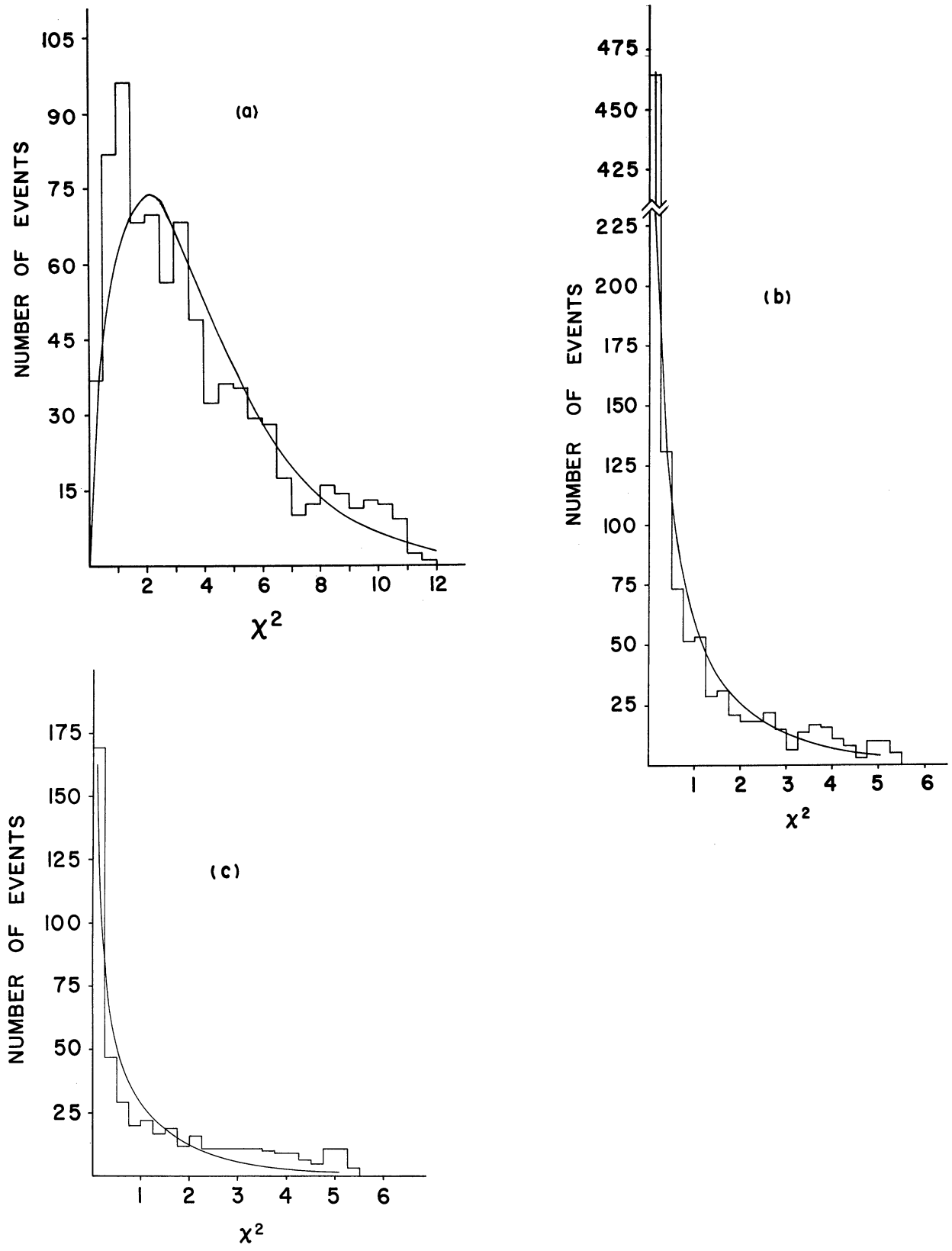

Figure 7. The χ^2 distributions for the good events as given in Table II. (a) $\pi^-\pi^-\pi^+p$, (b) $\pi^-\pi^-\pi^+p\pi^\circ$, and (c) $\pi^-\pi^-\pi^+\pi^+n$.

a) Only a very few of the events that passed the χ^2 test for the 4C fit alone were rejected because of the wrong bubble density.

b) All ambiguities between the 4C and 1C cases that could be resolved on the basis of bubble density belonged to the 4C category.

c) As is seen from Table I, most of the 4C ambiguities are with reaction (2.2). Figure 8, which shows the π° kinetic energy distribution along with phase space, clearly favors the assumption.

The ambiguities between (2.2) and (2.3) could not be resolved (see Figure 9). Consequently, any graphs drawn for these reactions will have the ambiguous events plotted separately so that the reader can observe their effect on the data. It will be seen, however, that there are no results which in any way depend on the treatment of this set of events. For the few self-ambiguous events one of the two fits has been eliminated in a random manner. After making the above changes the total number of events for the four reactions along with their cross sections are as given in Table II.

The total cross section for the four-prong events was found by counting tracks on every twenty-fifth picture and then computing the total track length scanned. There were corrections made and errors estimated due to beam attenuation, tracks coming in and going out the side of the fiducial volume, the varying depth of the beam in the chamber, and the purity[40] of the beam ($.97 \pm .02$). For the beam attenuation the total cross section of Diddens et al.,[50] was used, and the density of hydrogen was assumed to be $.0637 \pm .0020$ gm/cm.^{3}

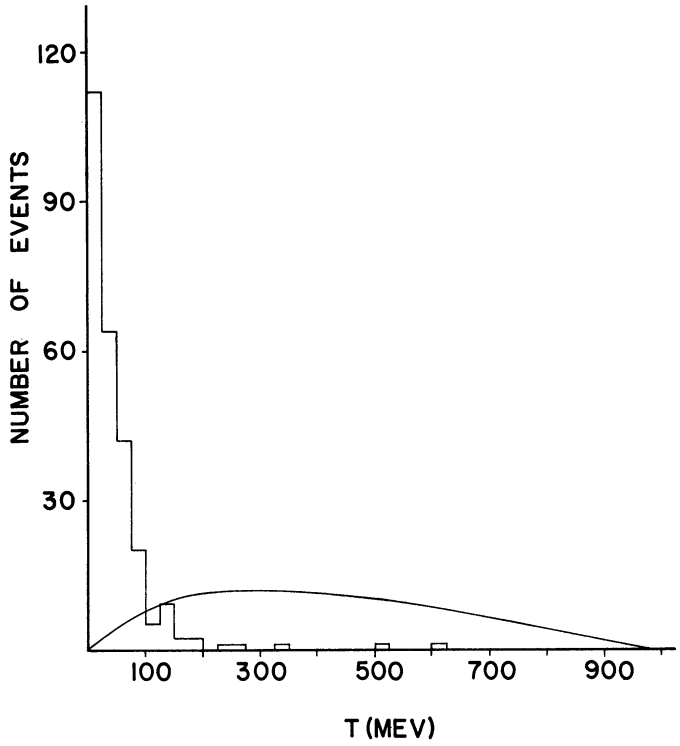

Figure 8. The π° kinetic energy for events ambiguous between $(\pi^-,\pi^-,\pi^+,p.\pi^\circ)$ and (π^-,π^-,π^+,p).

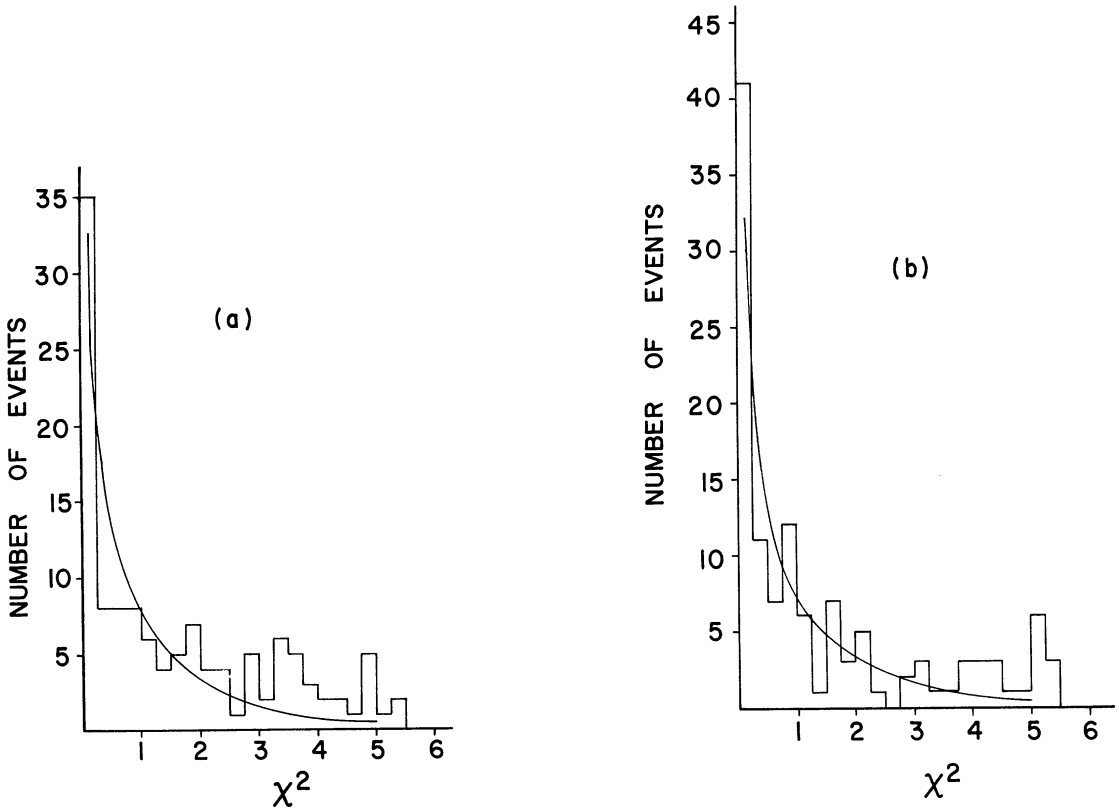

Figure 9. The χ^2 distributions for events ambiguous between $(\pi^-,\pi^-,\pi^+,p,\pi^\circ)$ and $(\pi^-,\pi^-,\pi^+,\pi^+,n)$. (a) if $(\pi^-,\pi^-,\pi^+,p,\pi^\circ)$ is assumed, and (b) if $(\pi^-,\pi^-,\pi^+,\pi^+,n)$ is assumed.

TABLE II

THE FINAL DISPOSITION OF EVENTS ALONG WITH THE PARTIAL CROSS SECTIONS

(The column labelled "Number" represents the actual number found in each category, while the column labelled "Adjusted Number" gives the corrected number of events after the two-percent addition is made. Note the comment in Table I for the $K^+K^-\pi^-p$ fit)

Event Type	Number	Adj. Number	Cross Section in mb.
$\pi^-\pi^-\pi^+p$	805	821	1.68±.09
$\pi^-\pi^-\pi^+p\pi^\circ$	1025	1046	2.14±.10
$\pi^-\pi^-\pi^+\pi^+n$	489	499	1.02±.06
$K^+K^-\pi^-p$	20	20	.06±.03
$\pi^-\pi^-\pi^+p\pi^\circ$ / $\pi^-\pi^-\pi^+\pi^+n$ Amb.	121	124	.25±.03
Rejected	1020	970	1.99±.10
Total	3480	3480	7.13±.26

The partial cross sections were found by multiplying the total cross section by the fraction of events for the appropriate channels. The numbers in all fitted categories were increased by 2% to correct for the χ^2 rejection level, and the total number in the unfitted category was reduced by the corresponding amount.

CHAPTER III

DEFINITIONS, NOTATION, AND PHASE SPACE

1. INTRODUCTION

In the following chapters, wherein this report focuses on the results of the data analysis, certain quantities and their notation will be used repeatedly. Although most of these are quite familiar to the reader, the multiple particle states to be considered here furnish numerous notational pitfalls which must be eliminated. Therefore, all commonly used quantities will now be defined precisely, and a standard method for representing them will be explained.

2. MASS

The effective mass, a Lorentz invariant, of a group of particles is given by

$$\text{Effective Mass} = \sqrt{\left(\sum_i E_i\right)^2 - \left(\sum_i \vec{P}_i\right)^2}, \qquad \text{(III.1)}$$

where E_i is the energy and $\vec{P}_i$ the vector momentum of the i'th particle. The mass of any combination of particles can be identified by the symbol "M", with the names of the constituents written as subscripts. For example, the mass of the (π^-,π^+) system is represented by $M_{\pi^-\pi^+}$ and the mass of the (π^-,π^-,p) system by $M_{\pi^-\pi^-p}$.

3. PHASE SPACE AND DALITZ PLOTS

Suppose there exists an initial quantum state $|i\rangle$ which consists of a set of particles so far apart that they do not interact, e.g., the π^- beam and target proton before interaction. Now let these initial-state particles collide and form a new state which will be called $|f\rangle$ when all particles are sufficiently separated so that they do not interact. It is believed that the probability of forming $|f\rangle$ from $|i\rangle$ can be represented by a unitary operator S:

$$p(i \to f) = |\langle f|S|i\rangle|^2 \qquad \text{(III.2)}$$

In order to describe completely the quantum states $|f\rangle$ and $|i\rangle$, it is necessary to specify momenta, spin, isotopic spin, etc. All of these are fixed values for any one state. If a specific reaction such as

$$\pi^- + p \to \pi_a^- + \pi_b^- + \pi^+ + p \qquad (3.1)$$

is considered, then Formula III.2 can be written

$$p(\pi^- + p \to \pi_a^- + \pi_b^- + \pi^+ + p) = |\langle \pi_a^- \pi_b^- \pi^+ p|S|\pi^- p\rangle|^2, \qquad \text{(III.2a)}$$

where all variables necessary to specify the states are fixed.

The transition probability which is usually desired is that from an initial fixed-momentum state—e.g., a beam of fixed momentum on a stationary target—to all final states of a given type—e.g., all possible states of the type $(\pi_a^-, \pi_b^-, \pi^+, p)$. To compute this transition probability, a sum has to be made over all final states and an average taken over all possible initial states. Let this be written as

$$\mathcal{P}(\pi^- + p \to \pi_a^- \pi_b^- \pi^+ p) = \sum_{|i>}{}' \sum_{|f>} \int d\rho \, |\langle \pi_a^- \pi_b^- \pi^+ p | S | \pi^- p \rangle|^2, \quad \text{(III.3)}$$

where

$\mathcal{P}(\pi^- p \to \pi_a^- \pi_b^- \pi^+ p)$ represents the total transition probability,

$\sum_{|i>}{}'$ represents an average over the initial states,

$\sum_{|f>}$ represents a sum over all final states except for the momentum sum,

and

$\int d\rho$ represents the sum over all possible final-state momenta which satisfy energy and momentum conservation. A sum over initial momenta is not needed since these are assumed to be constant.

Because very little is known about the form of S for strong interactions, its functional dependence is often assumed to be such that it can be pulled outside the integral and summations and given some average value $\bar{S}$. Although it might be argued that this is a good approximation because of the large number of states involved in the summation, probably the most convincing argument for this assumption is simply that it works for many cases.

The transition probability can now be written

$$\mathcal{P}(i \to f) \; \alpha \int d\rho. \quad \text{(III.4)}$$

The differential $d\rho$ is called the phase space distribution and can be shown to be given by[51]

$$d\rho \alpha \frac{d^3\vec{P}_1}{2E_1} \cdots \frac{d^3\vec{P}_n}{2E_n} \delta^4(P_f - P_i), \qquad \text{(III.5)}$$

where

$\vec{P}_1 \ldots \vec{P}_n$ are the vector momenta of the n particles in the final state,

$E_1 \ldots E_n$ are the energies of these particles,

P_f and P_i are the final and initial four-momenta of the system,

and

$\delta^4(P_f - P_i)$ is the Dirac delta function which here expresses conservation of energy and momentum.

In Appendix A the methods for evaluation of this integral are discussed, with emphasis placed on the phase-space mass distributions. It is also shown that for a three-body state (Call it A, B, and C) obeying phase space, a scattergram of M^2_{AB} vs. M^2_{BC} should be uniformly populated within the calculable kinematic limits.

4. RESONANCES

The distinguishing feature of resonant particles is their very short lifetimes, most of which are on the order of 10^{-23} seconds. Because of this the resonance doesn't travel much farther than a nuclear diameter before it decays, and consequently, only its decay products can be seen with the detection devices available to the experimenter.

By far the most common method of resonance detection is to plot the effective mass of a given combination of particles and then to examine the histogram for a surplus of events above phase space. This is illustrated in the next chapter where reaction (3.1) is discussed.

The $M_{\pi^-\pi^+}$ plot of Figure 10(a) shows a strong enhancement in the region from 660 to 820 MeV and is a consequence of ρ° production. Contrast this with the $M_{\pi^-\pi^-}$ distribution of Figure 10(c) where there is no evidence of a resonant state.

Another useful tool for resonance study is the Dalitz plot. This is only applicable to three-body final states such as

$$\pi^- + p \rightarrow \rho^\circ + \pi^- + p, \qquad (3.2)$$

and its utility is therefore more limited than the mass histogram. Since phase space implies a uniform population of points inside the boundaries of the Dalitz plot, a resonance appears as an overpopulated band perpendicular to one of the axes of constant mass-squared.

It must be emphasized that every deviation from phase space cannot be immediately interpreted as a consequence of resonance production. Indeed, one of the major tasks of the experimenter is to decide whether such deviations are due to real particles, or instead, whether they are caused by some kinematical or dynamical effect. Examples of this type will be encountered later for the $M_{\pi^-\pi^-p}$ distribution (see Figure 11(a)) of reaction (3.1) and the Dalitz plot (Figure 38) representing the three-pion decay of the ω°. It will be seen that the peak in the $M_{\pi^-\pi^-p}$ histogram is caused by the kinematics of reaction (3.2), and the density of points for the Dalitz plot will be shown to depend on the ω° spin-parity assignment. Because of angular momentum barriers this assignment affects the dynamics of the decay in such a way that the matrix element $\langle\omega^\circ|S|\pi^-\pi^+\pi^\circ\rangle$ cannot be ignored.

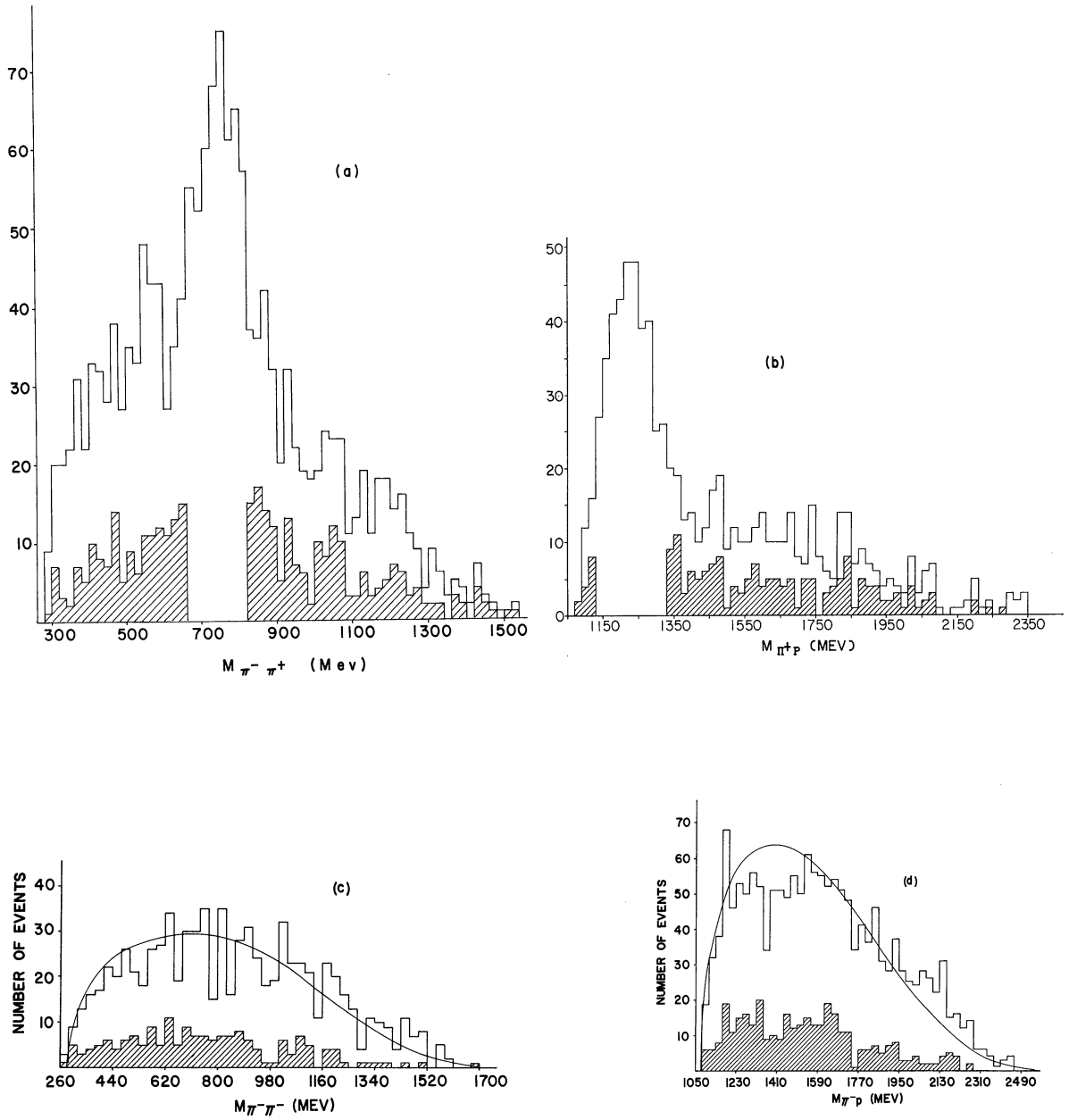

Figure 10. The two-body masses for the final state (π^-,π^-,π^+,p). The shaded area represents the 176 events which have no mass value in either the ρ° or $N^*_{3,3}(1238)$ peaks.

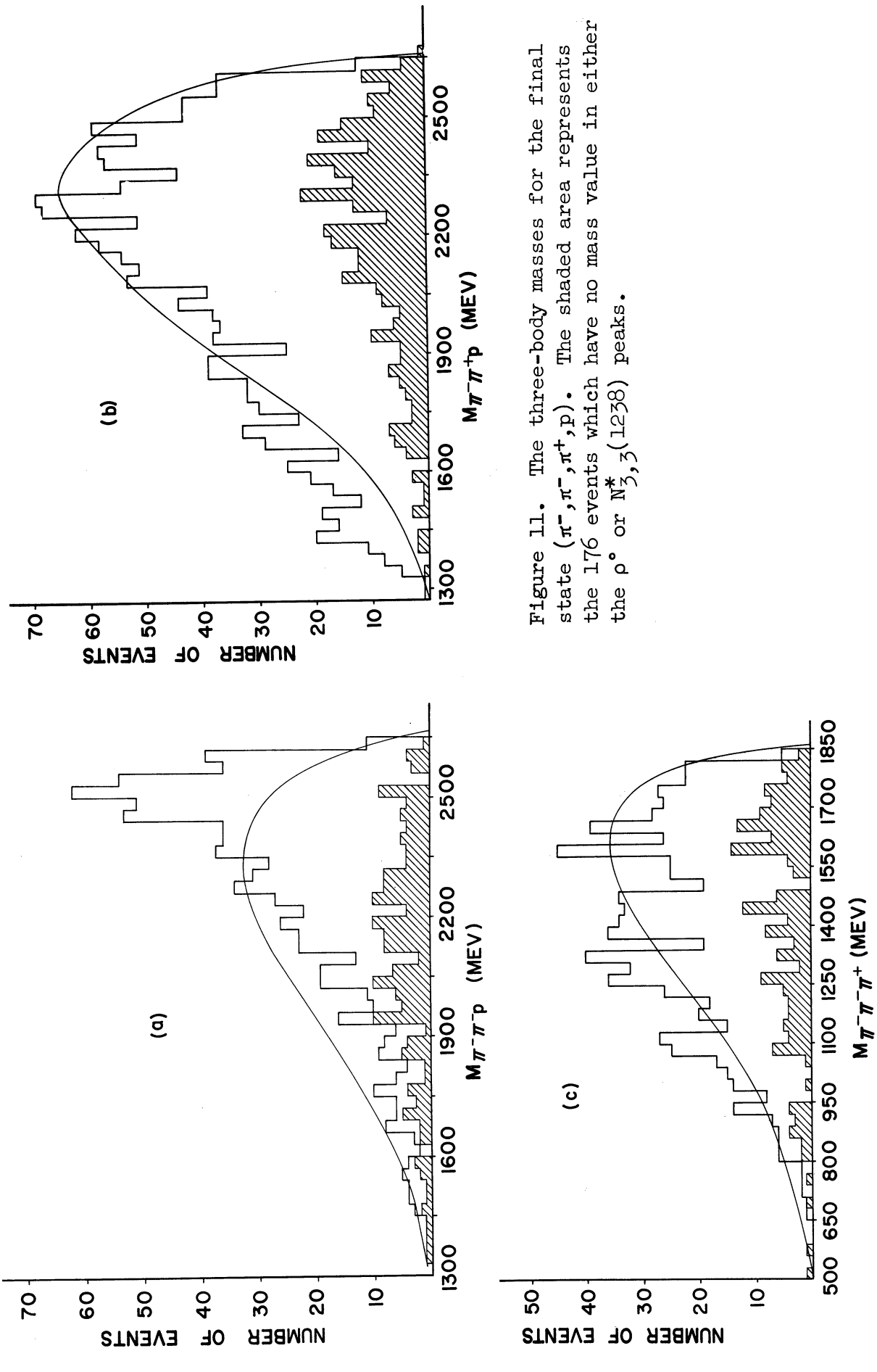

Figure 11. The three-body masses for the final state (π^-,π^-,π^+,p). The shaded area represents the 176 events which have no mass value in either the ρ^0 or $N^*_{3,3}(1238)$ peaks.

In the above discussion the resonances are referred to in terms of mass intervals rather than specific values. This spread in mass arises from two independent effects:

a) The Heisenberg uncertainty principle states that the accuracy of an energy measurement for a system is limited by the time that the system exists. This limitation is given by

$$\Delta E \, \Delta t \geq \hbar, \qquad \text{(III.6)}$$

where ΔE is the energy uncertainty,

Δt is the lifetime of the system,

and

$\hbar = 6.58 \times 10^{-22}$ MeV.Sec., Planck's constant.

Since the lifetime of a particle is given in the center-of-momentum frame ($\sum \vec{P}_i = 0$), Formula III.6 can be rewritten as

$$\Delta M \, \Delta t \geq \hbar \qquad \text{(III.7)}$$

This can be seen immediately upon inspection of Formula III.1. Because the lifetime of a strongly decaying particle is typically 10^{-23} second, Formula III.7 requires it to have an experimentally detectable mass spread of approximately 100 MeV. There can, of course, be decay-inhibiting effects due to angular momentum barriers and phase-space factors which increase a particle's lifetime and thereby decrease its width.

b) Because of errors in the momentum and direction measurements, there are errors in the mass computations of the particle combinations. These errors are large enough so that the ω° (see Figure 37(a)), whose

inherent width due to Formula III.7 is less than 10 MeV,[52] is spread out over a 60 MeV mass range in this experiment.

5. THE METHOD FOR TREATING "DOUBLE-RESONANCE EVENTS"

It has already been mentioned that there is a strong peak in the $M_{\pi^-\pi^+}$ distribution of reaction (3.1). It is also found that the channel

$$\pi^- + p \rightarrow \pi_a^- + \pi_b^- + \pi^+ + p + \pi^\circ \qquad (3.3)$$

shows an ω° in the (π^-,π^+,π°) system, and this same reaction also furnishes a significant ρ^- peak in the $M_{\pi^-\pi^\circ}$ plot. All three of these have one property in common—they all include the π^-, a particle which appears twice in both reactions (3.1) and (3.3). Since these reasonances are defined in a mass interval, both $M_{\pi_a^-\pi^+}$ and $M_{\pi_b^-\pi^+}$ can fall in the ρ° peak of reaction (3.1), $M_{\pi_a^-\pi^+\pi^\circ}$ and $M_{\pi_b^-\pi^+\pi^\circ}$ can both be associated with the ω° of (3.3), and the same is also true for $M_{\pi_a^-\pi^\circ}$ and $M_{\pi_b^-\pi^\circ}$ in the ρ^- peak of (3.3).

This "double-resonance" situation introduces the problem of which mass combination is to be chosen as the actual resonance. Whenever any one of these peaks is studied, it is necessary to use consistently the same combination throughout the analysis. It is not wise to choose, for example, (π_a^-,π^+) to calculate one quantity and then for the same event, to choose (π_b^-,π^+) to make another calculation. For this report, since all results were printed so that those associated with π_a^- were listed first, the choice is simple. Whenever both mass

combinations fall in a given peak, the one which includes π_a^- is used. Thus the production angles, scattering angles, momentum transfer, etc., will always be associated with the π_a^- resonance and never with the π_b^- resonance. This is equivalent to arbitrarily choosing one of the two combinations.

Also, when cross sections are computed by counting events above phase space, a correction for the above situation has to be made. Since this problem is not handled the same way in every case, its solution will be explained at the appropriate places in the report.

6. MORE DEFINITIONS

a) The Scattering Angle—Given the elastic scattering process

$$A + B \rightarrow A' + B',$$

the scattering angle is defined by

$$\cos \Theta = (\vec{P}_A \cdot \vec{P}_{A'})/|\vec{P}_A||\vec{P}_{A'}|, \qquad \text{(III.8)}$$

where P_A and $P_{A'}$ are the vector momenta of particle A before and after the interaction in the center-of-momentum reference frame of the particles A and B.

b) The Production Angle—The production angle of a particle A is defined by

$$\cos \Theta = \frac{\vec{P}_A \cdot \vec{P}_B}{|\vec{P}_A||\vec{P}_B|}, \qquad \text{(III.9)}$$

where $\vec{P}_A$ and $\vec{P}_B$ are the vector momenta of the particle A and the beam B, respectively, in the overall center-of-momentum system.

c) The Trieman-Yang Angle--Consider a final state consisting of three or more particles, two of which are A and C. Assume these are produced by a beam B incident on a target T. Now define the following variables in the rest system of the beam particle:

$\vec{P}_A$ momentum of A.

$\vec{P}_C$ momentum of C.

$\vec{P}_R$ vector sum of all final-state particle momenta except A and C.

$\vec{P}_T$ momentum of the target.

The Trieman-Yang angle[53] is defined by

$$\cos(TY) = \frac{(\vec{P}_T \times \vec{P}_R)\cdot(\vec{P}_A \times \vec{P}_C)}{|\vec{P}_T \times \vec{P}_R||\vec{P}_A \times \vec{P}_C|}. \qquad \text{(III.10)}$$

If the interaction producing this final state procedes via unmodified one-pion exchange, then the distribution of this angle (not the cosine) should be flat. This is made intuitively obvious by an examination of Figure 12. Since the pion is spinless, it cannot carry any directional information between the verticies, except along its momentum vector. Thus the planes defined by the momentum vectors at each vertex are completely uncorrelated.

d) Momentum Transfer--Consider a beam B interacting with a target T and producing two or more particles. Divide the final-state particles into two groups A and C. Now define the following variables in any reference frame:

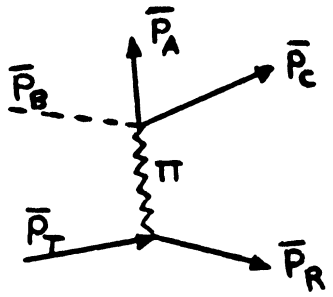

Figure 12. Diagram for an arbitrary single-pion-exchange process with all momenta given in the beam rest frame. The line representing the beam is dashed to emphasize that $\vec{P}_B=0$.

P_B beam four-momentum

P_T target four-momentum

P_A sum of the particle four-momenta for group A

P_C sum of the particle four-momenta for group C.

The momentum transfer from B to A is defined by

$$\Delta^2_{B\to A} = (P_B-P_A)^2 = (\vec{P}_B-\vec{P}_A)^2-(E_B-E_A)^2. \qquad \text{(III.11)}$$

Since momentum transfer is a Lorentz invariant, the coordinate system in which it is computed does not affect its value. Also, it follows from conservation of energy and momentum that

$$\Delta^2_{B\to A} = \Delta^2_{T\to C}. \qquad \text{(III.12)}$$

CHAPTER IV

THE REACTION $\pi^- + p \rightarrow \pi^- + \pi^- + \pi^+ + p$

1. THE MASS SPECTRA

The various two- and three-body mass spectra for the reaction

$$\pi^- + p \rightarrow \pi^- + \pi^- + \pi^+ + p \qquad (4.1)$$

are shown in Figures 10 and 11. The $M_{\pi^-\pi^+}$ plot shows a strong peak in the region from 660 to 820 MeV which can be attributed to the well-known ρ° meson. From the M_{π^+p} histogram it is seen that the $N^*_{3,3}(1238)$ resonance is also produced for a large fraction of the events which satisfy (4.1). Of the 805 events which belong to this channel, only 176 of them cannot be associated with at least one of the following two reactions:

$$\pi^- + p \rightarrow \pi^- + p + \rho^\circ \rightarrow \pi^- + \pi^+ \qquad (4.2)$$

$$\pi^- + p \rightarrow \pi^- + \pi^- + N^*_{3,3}(1238) \rightarrow \pi^+ + p. \qquad (4.3)$$

The mass spectra for these 176 events are represented by the shaded areas at the bottoms of the histograms. The other two-body mass combinations show no evidence for additional resonances. However, it will be seen later that there is some (π^-,p) isobar production associated with the ρ°.

In the three-body plots involving the proton, $M_{\pi^-\pi^-p}$ deviates from phase space at the high mass values, and $M_{\pi^-\pi^+p}$ shows an excessive

number of events at the low end of the spectrum. Both of these phase-space deviations are found to be primarily a reflection of reaction (4.2). The reasons for this are made quite clear when the production process for the ρ° is studied. In the overall center-of-mass reference frame it is found that the ρ° is produced chiefly in the beam direction, and the (π^-,p) state, in order to conserve momentum, goes opposite to the beam. Furthermore, the ρ° decay is characterized by a fast π^- almost parallel to the direction of motion and a much slower π^+ with a fairly random decay angle. A typical example of such a process is shown in Figure 13.

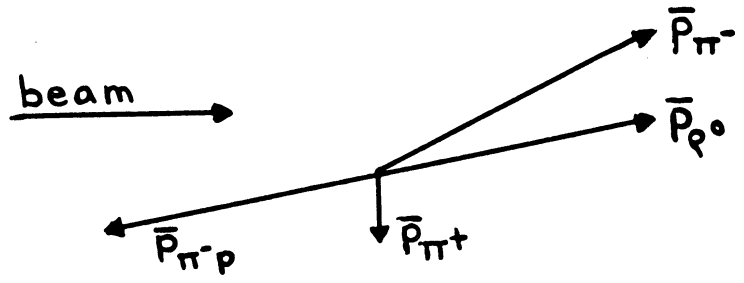

Figure 13. The momentum vectors for a typical reaction of type (4.2). $\vec{P}_{\pi^-}+\vec{P}_{\pi^+} = \vec{P}_{\rho^\circ}$ and $\vec{P}_{\pi^- p} + \vec{P}_{\rho^\circ} = 0$.

Because the momenta of the π^- and the (π^-,p) system are large, their corresponding energies are large, and the same is also true of the scalar sum $E_{\pi^-} + E_{\pi^- p}$ which represents the energy of the (π^-,π^-,p) state. Since $\vec{P}_{\pi^-}$ and $\vec{P}_{\pi^- p}$ are almost in opposite directions, their vector sum, which is $\vec{P}_{\pi^-\pi^- p}$, is small. Thus by Formula III.1, the resultant mass of the (π^-,π^-,p) system is concentrated at the high end of the spectrum for the ρ° events. On the other hand, for the (π^+,π^-,p)

state, since most of its energy and momentum contribution comes from the (π^-,p) combination, Formula III.1 gives an unusually large number of low values for $M_{\pi^+\pi^-p}$.

In the $M_{\pi^-\pi^-\pi^+}$ histogram there is some evidence for the A_1 and A_2 mesons, but the number of events above phase space is within two standard deviations for both peaks. It will be seen later that these peaks are significant, and that they are associated specifically with the (ρ°,π^-) combination in reaction (4.2) rather than the three-body state.

2. THE ρ°-$N^*_{3,3}$ (1238) SEPARATION AND THEIR CROSS SECTIONS

If a resonant state is considered to be a distinct particle, as will be done in this section, then for reaction (4.1) only one ρ° or one $N^*_{3,3}$ (1238) can be produced in a given event because of the single π^+. Thus some separation procedure has to be developed for those events which can be interpreted as belonging to either reaction (4.2) or reaction (4.3). In order to estimate production cross sections above phase space and to get certain angular distributions, the following method for the ρ°-$N^*_{3,3}$ (1238) overlap is used.

Figure 14(a) gives the M_{π^+p} spectrum for those events in which a ρ° is produced. Phase space is computed by assuming reaction (4.2), letting the ρ° decay into a π^- and a π^+, then computing M_{π^+p}, and finally, normalizing to that portion of the histogram where $M_{\pi^+p} \geq 1340$ MeV. This is accomplished by means of a Monte Carlo calculation, using

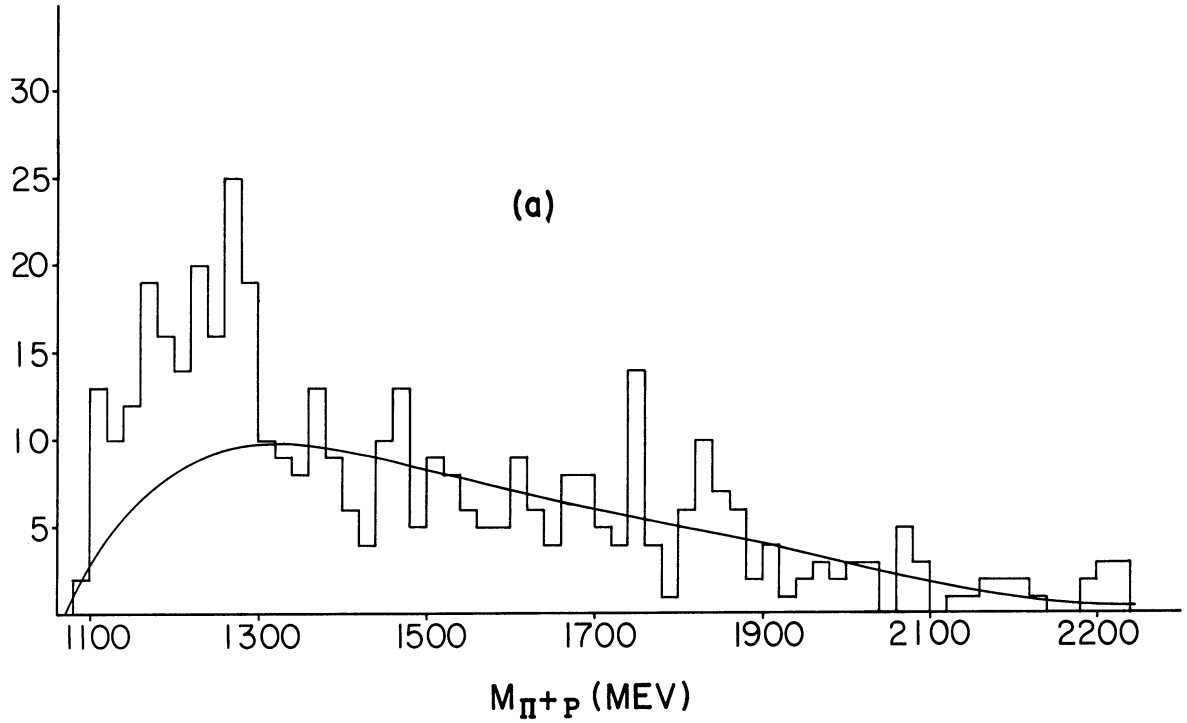

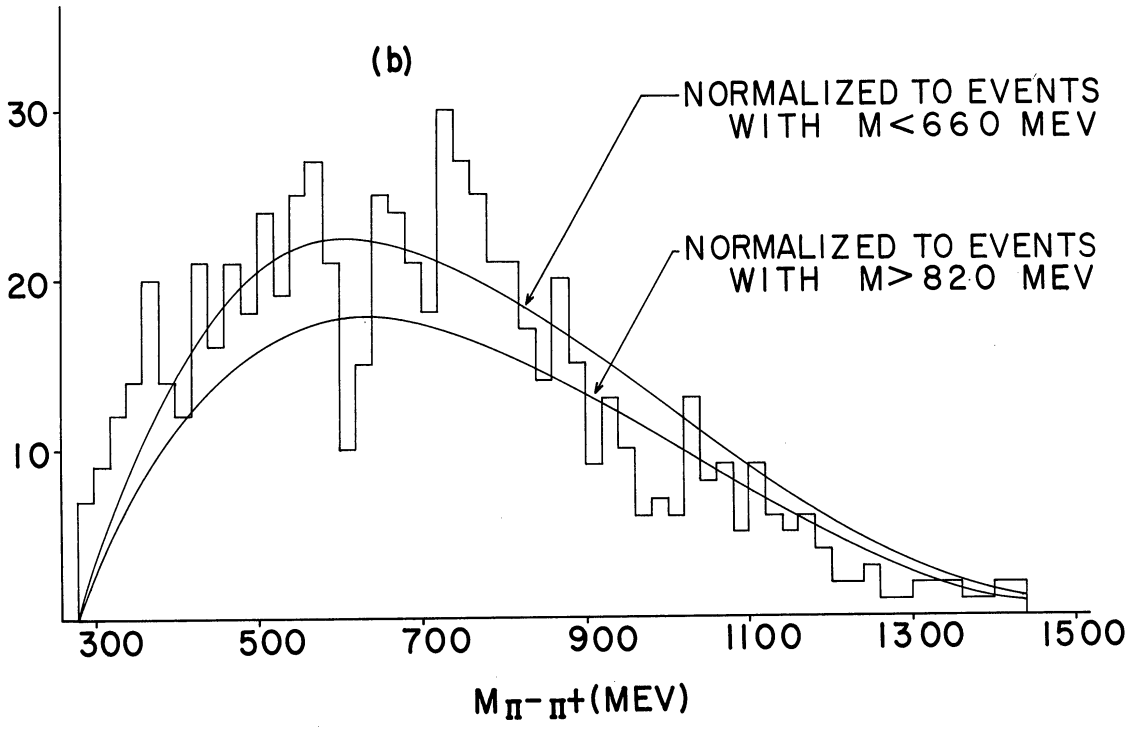

Figure 14. (a) M_{π^+p} for the ρ° events, and (b) $M_{\pi^-\pi^+}$ for the $N^*_{3,3}(1238)$ events.

two- and three-body programs [54,55] which generate events according to phase space. The ρ° is assumed to have the mass values 670, 690, 710... 810 MeV, and the results for each mass are then weighted according to the bin sizes in Figure 10(a).

Figure 14(b) represents the $M_{\pi^-\pi^+}$ spectrum for those events which satisfy reaction (4.3). Phase-space curve (1) is normalized to the events where $M_{\pi^-\pi^+} < 660$ MeV, and curve (2) is normalized to that portion of the histogram where $M_{\pi^-\pi^+} \geq 820$ MeV. Phase space is computed in the same manner as was done for the ρ°, only the initial three-body state (π^-, π^-, $N^*_{3,3}(1238)$) is assumed.

From Figure 14(a) it is estimated that the ρ° sample contains 85 ± 9 more $N^*_{3,3}(1238)$ events than there should be according to phase space. From Figure 14(b) it is estimated that there is an excess of 45 ± 9 ρ° events in the $N^*_{3,3}(1238)$ sample. Finally, since there are 162 events belonging to both the ρ° and $N^*_{3,3}(1238)$ peaks, there must be 32 ± 13 phase-space events of this type.

Of these 162 ρ° -$N^*_{3,3}(1238)$ overlap events, a total of 25 of them have both (π^-,π^+) combinations falling in the ρ° region. From the Monte Carlo calculations it is estimated that there should be 21 double- ρ° events in this sample. It is seen that the calculated and experimental numbers are in good agreement.

The assumed division of these 162 events is summarized below in Table III.

TABLE III

THE ESTIMATED DIVISION OF THE ρ°-$N^*_{3,3}(1238)$ OVERLAP EVENTS

Type	Number	Calculated Number of Double-ρ°'s
$\pi^- + p \rightarrow \pi^- + \pi^- + N^*_{3,3}(1238)$	85±9	11
$\pi^- + p \rightarrow \pi^- + p + \rho^\circ$	45±9	6
$\pi^- + p \rightarrow \pi^- + \pi^- + \pi^+ + p$	32±13	4

With these numbers it is now possible to find the proper normalization for phase space along with the ρ° and $N^*_{3,3}(1238)$ cross sections. The large 41% error in the number of ρ°-$N^*_{3,3}(1238)$ phase-space events will be implied in the normalization calculation but will be considered explicitly when the ρ° and $N^*_{3,3}(1238)$ cross sections are computed. The method used to find these quantities is best explained in the following step-by-step summary:

a) From the $M_{\pi^+ p}$ histogram (Figure 10(b)) all ρ° events are subtracted. This result is the unshaded area in Figure 15(a). The unshaded area in Figure 15(b) shows the $M_{\pi^- \pi^+}$ plot of Figure 10(a) with all $N^*_{3,3}(1238)$ events subtracted.

b) Out of 6,000 Monte Carlo events for the final state $(\pi^-, \pi^-, N^*_{3,3}(1238))$, 2583 ρ° mesons are generated. Therefore, if there are 32 ρ°-$N^*_{3,3}(1238)$ events in phase space, there are

$$\left(\frac{6000}{2583}\right) \times 36 = 84$$

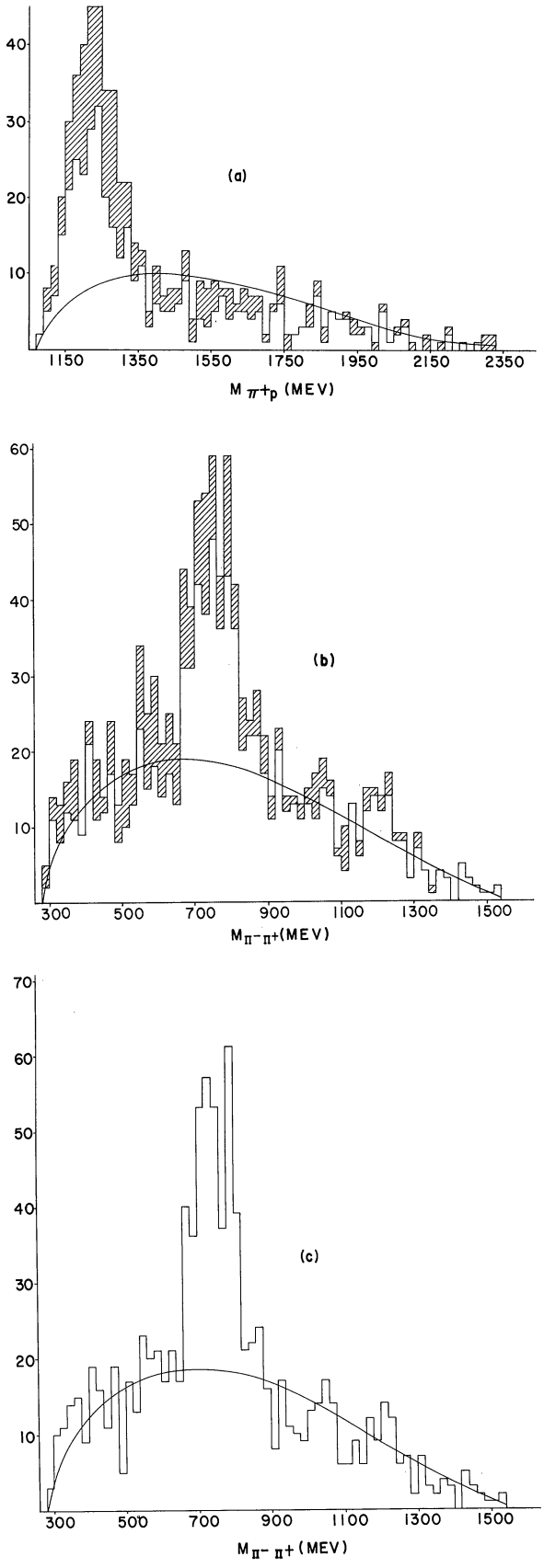

Figure 15. Various stages of ρ°-$N^{*}_{3,3}(1238)$ overlap estimates.

phase-space events satisfying reaction (4.3). The number 36 is used in this calculation because there are 4 double -ρ°'s in 32 ρ°-$N^{*}_{3,3}(1238)$ events.

c) In the (ρ°,π^{-},p) final state 6,000 Monte Carlo calculations generate 1490 events satisfying reaction (4.3). With this same final state 1090 ρ°'s are generated with the π^{+} from the ρ° decay and the π^{-} not involved in the decay.

Therefore, there are

$$\left(\frac{6000}{1490}\right) \times 32 = 129$$

phase-space events satisfying reaction (4.2). This corresponds to

$$\left(1 + \frac{1090}{6000}\right) \times 129 = 152$$

mass points in the ρ° region of phase space.

d) Now the proper normalizations for the $M_{\pi^-\pi^+}$ and M_{π^+p} phase-space distributions can be found. This is accomplished by taking the phase-space distributions calculated for the ($\pi^{-}\pi^{-}\pi^{+}$p) final state and normalizing $M_{\pi^-\pi^+}$ to 152 events between 660 and 820 MeV and M_{π^+p} to 84 events between 1130 and 1330 MeV. The two phase-space curves are drawn on the appropriate histograms in Figures 15(a) and 15(b).

Although only one of the two normalizations is necessary to get the phase-space curves for the two histograms, both are used in order to check the numbers found in the Monte Carlo calculations. This is accomplished by finding the ratio of the area under the $M_{\pi^-\pi^+}$ curve to

that under the M_{π^+p} curve. A numerical integration gives the result 760/377 which is very close to the correct value of 2/1.

e) Since many events have been incorrectly subtracted from the two mass distributions, these now have to be put back into the proper histograms. These additions, all of which are made to the unshaded portions of Figure 15(a) and 15(b) and represented by the shaded areas in these figures, are listed below:

1) From Table III it is seen that 85 events of the ρ°-$N^*_{3,3}(1238)$ overlap have to be added to the M_{π^+p} distribution.

2) Also from Table III, it is seen that 45 events of this same type have to be added to the $M_{\pi^-\pi^+}$ histogram. Since there are two (π^-,π^+) combinations per event, this addition totals 90 points, fifty-one of which are in the ρ° region.

3) Since there are 84 phase-space events satisfying reaction (4.3),

$$2 \times 84 = 168$$

points of this type have to be added to the $M_{\pi^-\pi^+}$ distribution. As a result of the division summarized in Table III, thirty-two of these have to be of the ρ°-$N^*_{3,3}(1238)$ overlap variety.

4) Because there are 129 phase-space events satisfying reaction (4.2), the M_{π^+p} histogram has to be increased by 129 points, with thirty-two of these belonging to the ρ°-$N^*_{3,3}(1238)$ overlap sample.

f) In Figure 15(b), with the shaded area now included, there are 244 events above phase space. For every one of these there is another (π^-,π^+) mass value which is not part of phase space and should therefore be subtracted from the histogram. Because of the double-ρ°

possibility this peak actually corresponds to

$$\left(\frac{6000}{6000+1090}\right) \times 244 = 206$$

ρ° events above phase space. Therefore, in order to represent the $M_{\pi^-\pi^+}$ distribution correctly, 206 events have to be subtracted from Figure 15(b), and thirty-eight of these must come from the ρ° region. After this subtraction is made, the $M_{\pi^-\pi^+}$ distribution shown in Figure 15(c) is obtained.

g) The M_{π^+p} and $M_{\pi^-\pi^+}$ distributions represented by Figures 15(a) and 15(c) can now be used to calculate the $N^*_{3,3}(1238)$ and ρ° cross sections. This is accomplished by simply counting the number of events above phase space. These cross sections along with their errors are given in Table IV. The large uncertainties are primarily due to the 41% error in the phase-space normalization.

TABLE IV

THE ρ° AND $N^*_{3,3}(1238)$ CROSS SECTIONS FOR THE REACTION $\pi^-+p\rightarrow\pi^-+\pi^-+\pi^+$+p

Type	Number Above Phase Space	Cross Section in mb.
$\pi^-+p\rightarrow\pi^-+\pi^-+N^*_{3,3}(1238)$	243±39	.51±.09
$\pi^-+p\rightarrow\pi^-+p+\rho^\circ$	206±65	.43±.14
$\pi^-+p\rightarrow\pi^-+\pi^-+\pi^+$+p	—	.74±.30

In the Monte Carlo calculations described above, the production angles for the ρ° and $N^*_{3,3}(1238)$ are distributed according to phase space. This is not found to be true for the real events, as the ρ° is produced primarily in the forward direction and the $N^*_{3,3}(1238)$ is produced primarily in the backward direction. In order to evaluate the influence of this effect on the above estimates, the phase-space mass distributions have also been computed for just those events in which the production angle of the ρ° is small ($\cos\theta > .9$) and the production angle of the $N^*_{3,3}(1238)$ is large ($\cos\theta < -.9$). It is found that these restrictions have virtually no effect on the phase-space estimates and can therefore be ignored.

3. THE TWO-PION DECAY OF THE ω°

Since the ω° has a negative G-parity, it cannot decay into two pions through the strong interaction. However, a two-pion electromagnetic decay, for which G-parity is not a good quantum number, is allowed for the ω°. Since phase space and angular momentum barriers favor this over the three-pion decay, it is possible that the two- and three-pion rates may be comparable in spite of the different decay mechanisms.

There have been many experiments with widely varying results which have attempted to detect this decay mode of the ω°. In a compilation of the data from several experiments, Lütjens and Steinberger[56] conclude that "there is no statistically significant indication for the

decay of the ω° into two pions." This is contrary to the results of some of the subsamples of their data, and it is in strong disagreement with the results of Fickinger, Robinson, and Salant.[57]

In this experiment a strong ω° peak is found in the reaction (see Chapter V)

$$\pi^- + p \rightarrow \pi^- + p + \omega^\circ \rightarrow \pi^- + \pi^+ + \pi^\circ. \tag{4.4}$$

Since ω° production for the (π^-,π^-,π^+,p) state also has to occur through the channel

$$\pi^- + p \rightarrow \pi^- + p + \omega^\circ \rightarrow \pi^- + \pi^+, \tag{4.5}$$

the branching ratio $R = \dfrac{\sigma(\pi^-+p\rightarrow\pi^-+p+\omega^\circ\rightarrow\pi^-+p+\pi^-+\pi^+)}{\sigma(\pi^-+p\rightarrow\pi^-+p+\omega^\circ\rightarrow\pi^-+p+\pi^-+\pi^++\pi^\circ)}$ can be computed. This experimental number, however, is only valid if there is no interference between the (π^-,π^+) states produced in the ω° and ρ° decays. Durand and Chiu[58] have pointed out that a very small R can lead to a fairly large change in the $M_{\pi^-\pi^+}$ spectrum at the ω° mass if interference is assumed. Thus the branching ratio computed here is only an upper limit on the true value.

In Figure 16(a) $M_{\pi^-\pi^+}$ is shown in 10 MeV bins for the region 600-840 MeV. The 770-800 MeV region shows a surplus of approximately 8± 10 events above a smooth background. Assuming 18 events above phase space, this corresponds to a branching ratio of $R \leq .18$ and is consistent with $R = 0$.

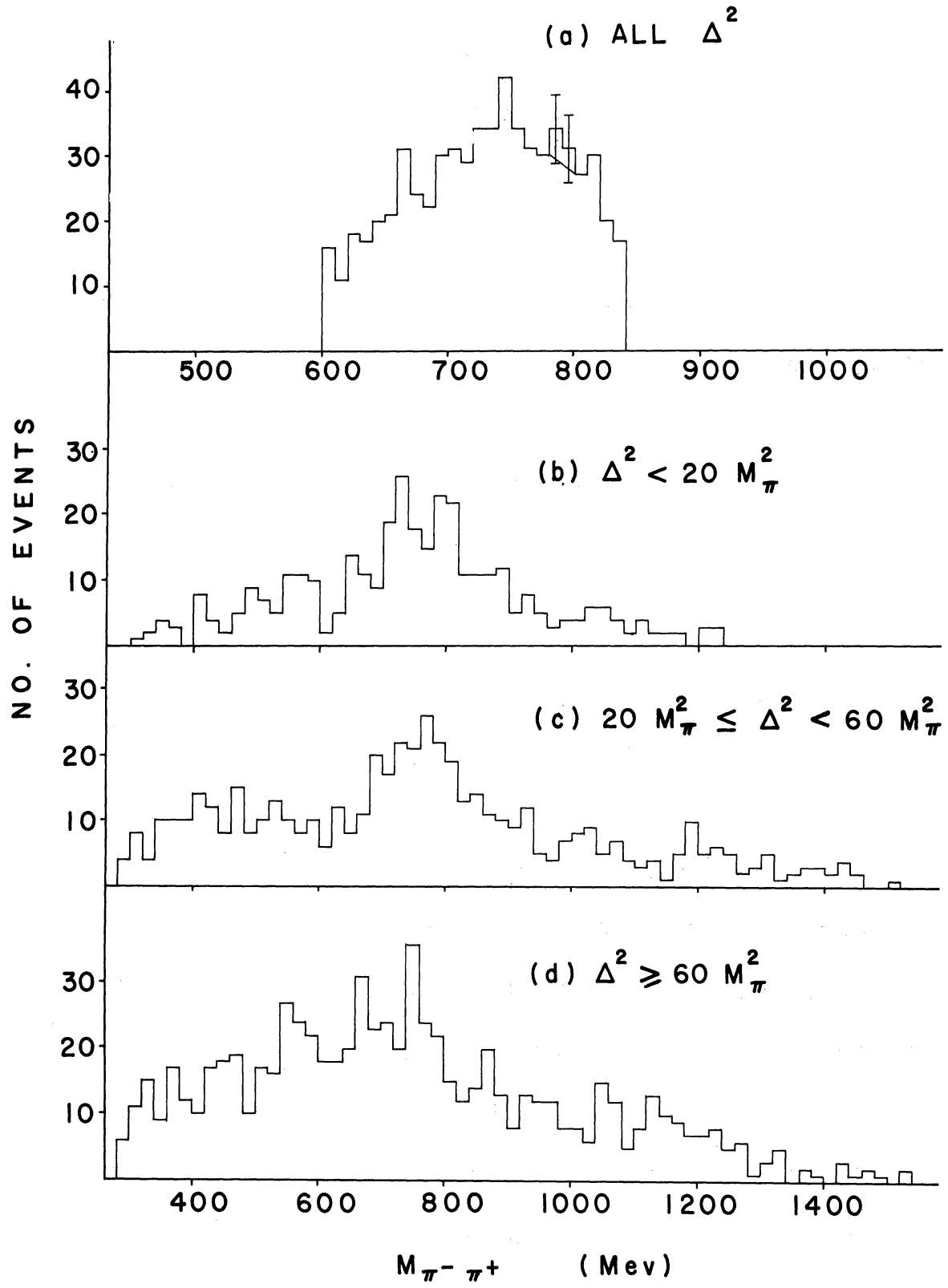

Figure 16. $M_{\pi^-\pi^+}$ for (a) all $\Delta^2_{\pi^-\to\pi^-\pi^+}$, (b) $\Delta^2_{\pi^-\to\pi^-\pi^+} < 20\ M_\pi^2$, (c) $20M_\pi^2 \leq \Delta^2_{\pi^-\to\pi^-\pi^+} < 60M_\pi^2$, and (d) $\Delta^2_{\pi^-\to\pi^-\pi^+} \geq 60M_\pi^2$.

$M_{\pi^-\pi^+}$ is presented in Figures 16(b), 16(c), and 16(d) for the three regions: (1) $\Delta^2_{p\to\pi^-p} < 20M_\pi^2$, (2) $20M_\pi^2 \leq \Delta^2_{p\to\pi^-p} < 60M_\pi^2$, (3) $60M_\pi^2 \leq \Delta^2_{p\to\pi^-p}$. In Figure 16(b) there is some structure to the ρ° region of the histogram which one might want to attribute to the ω°, but it is statistically no more significant than the two peaks of Figure 16(d) which cannot be associated with ω° production because of their masses.

Finally, it should be noted that the apparent structure in the mass plot of Figure 15(c) cannot be considered seriously because of the many additions and subtractions which were made to arrive at this histogram.

4. THE ρ° MESON

4.1 Introduction

Once the existence of a new particle has been established, an understanding of the mechanism responsible for its production then becomes desirable. This requires a study of quantities such as production angles, momentum transfer, etc., in order to compare their distributions against those predicted by the theoretical models. The purpose of this section is to discuss the results of such a study for the ρ° meson produced in reaction (4.1). The mass range chosen for the ρ° is from 660 to 820 MeV, and the method of Chapter III, Section 5 is used for picking one of the two possible (π^-,π^+) combinations when both of them fall in the ρ° region.

It will be found that the ρ° can be associated with many different production processes. Some are produced in the reactions

$$\pi^- + p \rightarrow \rho^\circ + N^*_{3,-1}(1238) \rightarrow \pi^- + p \tag{4.6}$$

and

$$\rightarrow \rho^\circ + N^*_{1,-1}(1512) \rightarrow \pi^- + p, \tag{4.7}$$

others are produced via the modes

$$\pi^- + p \rightarrow p + A_1 \rightarrow \rho^\circ + \pi^- \tag{4.8}$$

and

$$\rightarrow p + A_2 \rightarrow \rho^\circ + \pi^-, \tag{4.9}$$

and some can only be associated with reaction (4.2).

4.2 ISOBAR PRODUCTION IN ASSOCIATION WITH THE ρ° MESON

The first thing that should be examined is the distribution of $M_{\pi^- p}$ for reaction (4.2). This is shown in Figure 17(a) with phase space normalized to the total number of events. The shaded histogram corresponds to the 162 events which belong to both the ρ° and $N^*_{3,3}(1238)$ peaks.

Since it was concluded in Section (3) that 85 events of the ρ°-$N^*_{3,3}(1238)$ overlap should be placed in the $N^*_{3,3}(1238)$ category, a more accurate representation of $M_{\pi^- p}$ is obtained by subtracting approximately one-half (85/162) of these. The result of a random subtraction of 85 $N^*_{3,3}(1238)$ events is shown in Figure 17(b). Since the high-mass distribution follows phase space quite accurately, the normalization

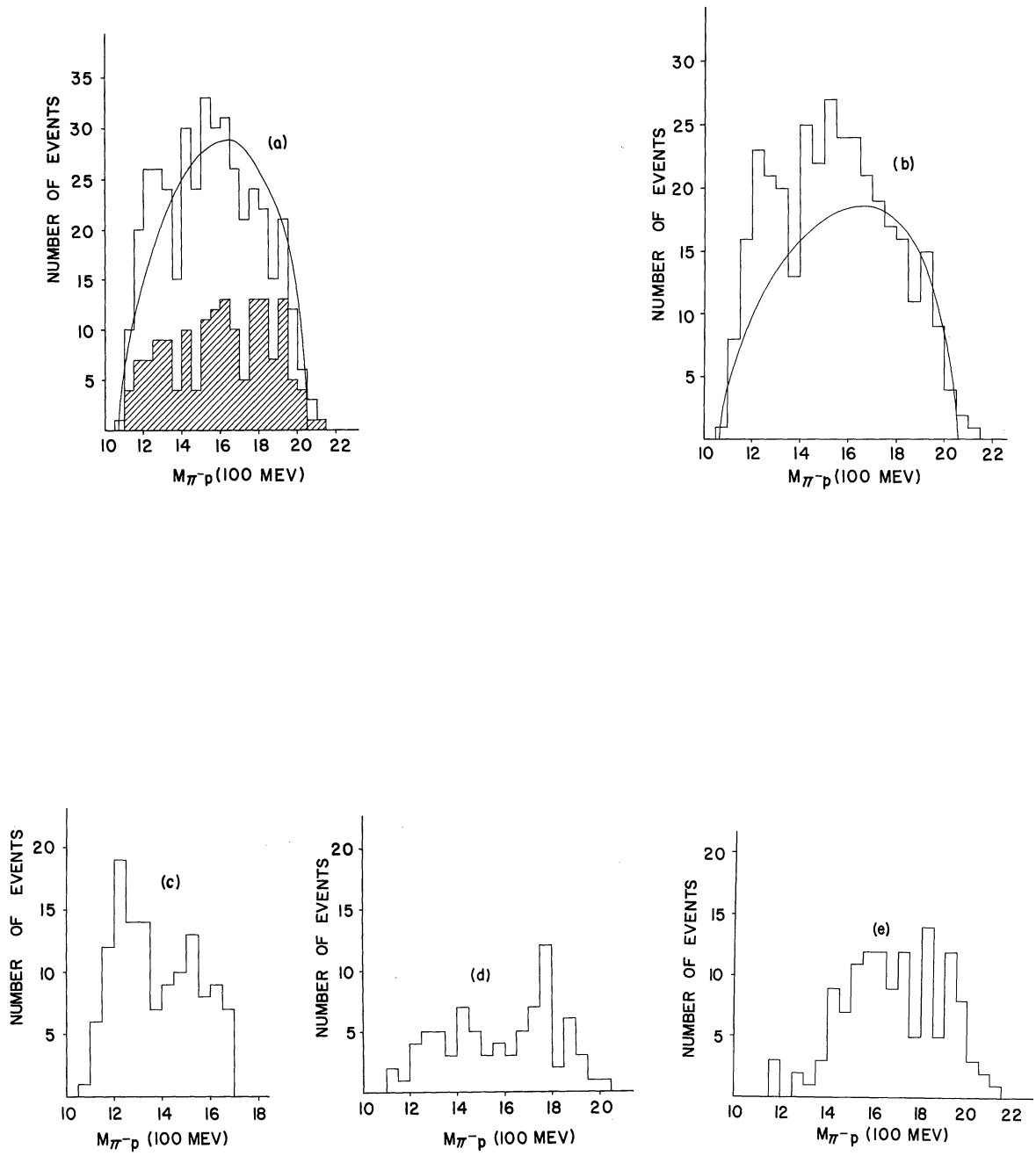

Figure 17. M_{π^-p} for the reaction $\pi^- + p \rightarrow \rho^\circ + \pi^- + p$. (a) all events. with the shaded area representing the $N^*_{3,3}(1238)$ overlap; (b) the distribution of (a) with 85 $N^*_{3,3}(1238)$ events subtracted and phase space normalized to $M_{\pi^-p} \geq 1700$ MeV; (c) $\Delta^2_{\pi^-\rightarrow\rho^\circ} < 20M^2_\pi$; (d) $20M^2_\pi \leq \Delta^2_{\pi^-\rightarrow\rho^\circ} < 40M^2_\pi$; and (e) $\Delta^2_{\pi^-\rightarrow\rho^\circ} \geq 40M^2_\pi$.

is made for the region where $M_{\pi^-p} > 1700$ MeV. If this normalization is assumed to be correct, it is then concluded that a fairly large number of the ρ° mesons are produced by means of reactions (4.6) and (4.7).

In Figures 17(c), 17(d), and 17(e) the M_{π^-p} distribution is given for three different ranges of $\Delta^2_{p\to\pi^-p}$: (1) for $\Delta^2_{p\to\pi^-p} < 20M_\pi^2$, (2) for $20M_\pi^2 \leq \Delta^2_{p\to\pi^-p} < 60M_\pi^2$, (3) for $\Delta^2_{p\to\pi^-p} \geq 60\ M_\pi^2$. From these histograms it is quite clear that reactions (4.6) and (4.7) dominate the production of ρ° mesons at low momentum transfer. Although it is not shown here, the $N^*_{3,3}(1238)$ contamination is just as large for these low $\Delta^2_{p\to\pi^-p}$ events as it is for the entire sample of reaction (4.2).

4.3 THE ρ° AND THE ONE-PION-EXCHANGE MODEL

In the last few years many pion production processes have been found to be consistent with the one-pion-exchange model.[11] This is based on the diagram shown in Figure 18(a), where the exchanged particle is the relatively light π meson. Since G-parity is conserved in strong interactions, only an even number of pions can come from the upper vertex. For reaction (4.1) this limits the number of possible cases to the two shown in Figures 18(b) and 18(c). Because ρ° and $N^*_{3,3}(1238)$ production require that the π^+ be associated with different verticies, the entire sample of 805 events cannot be explained by one diagram. Figure 18(b) is needed for the ρ° meson, while $N^*_{3,3}(1238)$ production, if it occurs by means of pion exchange, requires the mechanism of Figure 18(c).

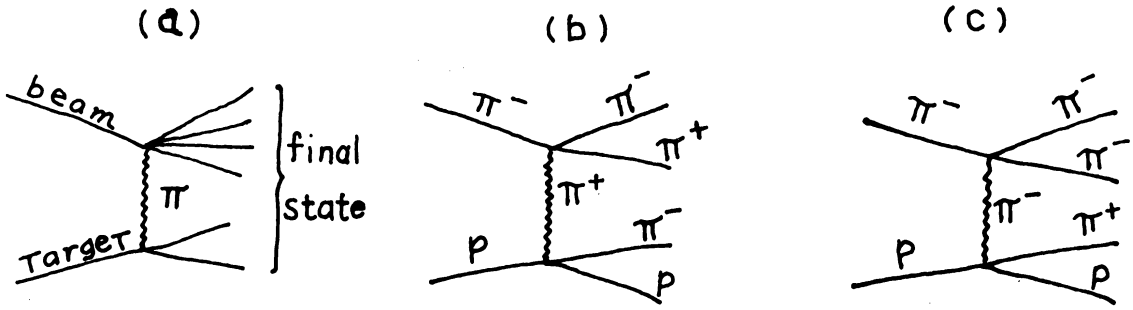

Figure 18. Pion-exchange diagrams for (a) an arbitrary process and (b and c) the possible cases of reaction (4.1).

The purpose of this section is to determine whether or not the ρ° can be analyzed in terms of a one-pion-exchange process; that is, the validity of the diagram of Figure 18(b) will now be investigated with the upper vertex restricted to the region $660 \leq M_{\pi^-\pi^+} < 820$ MeV (see Figure 3).

In a peripheral interaction such as that represented by the exchange of a low-mass particle, the net momentum at either vertex should not have a large transverse component. This property can be tested by examining the momentum transfer and production angle distributions for the resultant particle at either vertex. These distributions are shown in Figures 19 and 20 for the ρ° region, and they are both clearly consistent with the one-pion-exchange model.

The Trieman-Yang angle is shown in Figure 21(a). Ignoring absorptive effects, the distribution of this angle should be flat if reaction (4.2) is governed by one-pion exchange. It is apparent that this is not true for the entire ρ° sample. However, this plot cannot

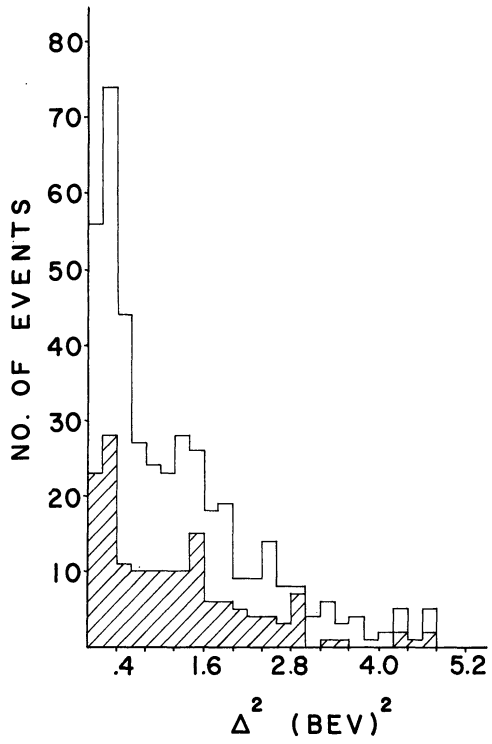

Figure 19. The $\Delta^2_{\pi^- \to \rho^0}$ distribution. The shaded area represents the $N^*_{3,3}(1238)$ overlap.

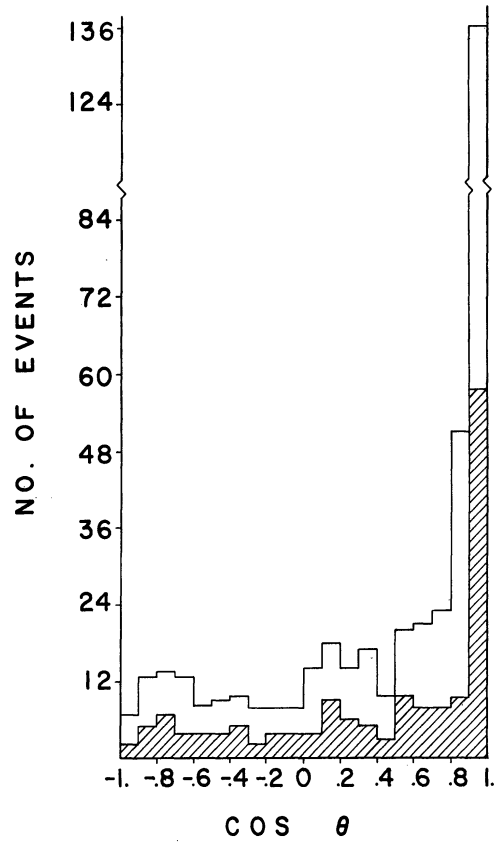

Figure 20. Production angle for the ρ^0. The shaded area represents the $N^*_{3,3}(1238)$ overlap.

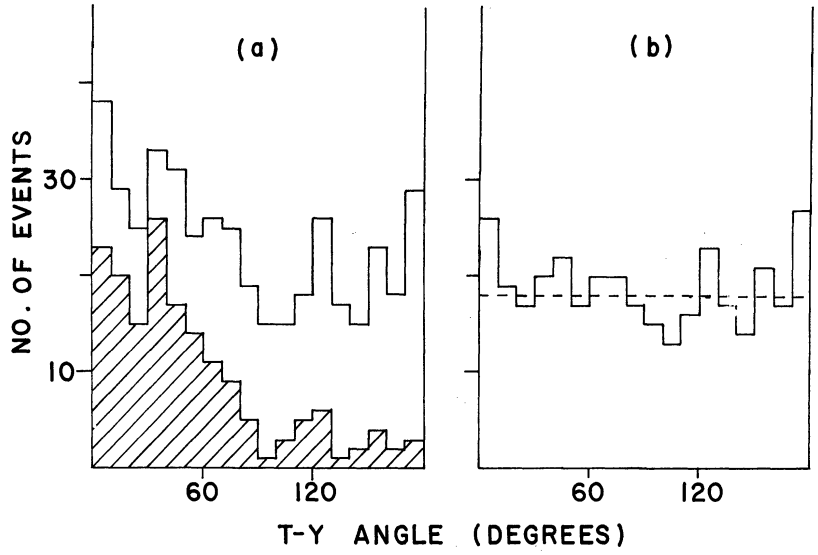

Figure 21. The Trieman-Yang angle for the ρ^0 events. (a) all events with the $N^*_{3,3}(1238)$ overlap shaded, and (b) after a subtraction of 85 $N^*_{3,3}(1238)$ events from (a).

be considered as representative of reaction (4.2) until the $N^*_{3,3}(1238)$ overlap is subtracted properly. After randomly subtracting 85 $N^*_{3,3}(1238)$ events, the result shown in Figure 21(b) is obtained. This shows a fairly uniform distribution with perhaps a slight overpopulation at the low and high angles. Since a straight-line fit to this plot yields a χ^2 probability of 74%, the Trieman-Yang test agrees very well with the one-pion-exchange assumption.

4.4 THE ρ° DECAY

Since the ρ° data is rendered so complex by the $N^*_{3,3}(1238)$ events and the multitude of reactions responsible for the meson's production, and furthermore, since a fairly pure ρ° sample is available in other final states, anything more than a rather qualitative investigation of its decay would be quite fruitless. A thorough analysis of this problem can be found in studies of the reaction[29]

$$\pi^- + p \rightarrow n + \rho^\circ \rightarrow \pi^- + \pi^+. \qquad (4.10)$$

If the one-pion-exchange model is assumed to be valid, and further, if the exchanged π^+ is assumed to be real, then the peak can be analyzed by means of a partial wave analysis for (π^-,π^+) scattering. Since Bose statistics require two pions to be in a symmetric state, even angular momentum corresponds to even isotopic spin and odd angular momentum to odd isotopic spin.

If Θ is defined as the scattering angle for the π^- in the ρ° center of mass, and if all angular momenta above L = 1 are ignored, then

$$\frac{d\,\sigma_{\pi^-\pi^+}}{d(\cos\Theta)} = \frac{2\pi}{k^2}\left| e^{i\delta_0}\sin\delta_0 + 3e^{i\delta_1}\sin\delta_1\cos\Theta\right|^2$$

$$= A + B\cos\Theta + C\cos^2\Theta, \qquad \text{(IV.1)}$$

where k is the propagation number of the pions in their center of mass, and δ_0 and δ_1 are the phase shifts of the s- and p- waves, respectively. The coefficients A, B, and C are given in terms of the phase shifts and the propagation number by

$$A = \frac{2\pi}{k^2}\sin^2\delta_0,$$

$$B = \frac{12\pi}{k^2}\sin\delta_0\sin\delta_1\cos(\delta_0-\delta_1), \qquad \text{(IV.2)}$$

and

$$C = \frac{18\pi}{k^2}\sin^2\delta_1.$$

In Figure 22(a) the cos Θ distribution is shown for all $\Delta^2_{\pi^-\to\rho^\circ}$. After subtracting 85 $N^*_{3,3}(1238)$ events in the same manner as was done for the Trieman-Yang angle, the distribution shown in Figure 22(b) is obtained. Both of these plots display the familiar forward-backward asymmetry that has been observed in many other experiments.[29,37]

In Figures 23(a-c) the scattering angle is given for three ranges of momentum transfer: $\Delta^2_{\pi^-\to\rho^\circ} < 20M_\pi^2$, (2) $20M_\pi^2 \leq \Delta^2_{\pi^-\to\rho^\circ} < 40M_\pi^2$, (3) $40M_\pi^2 \leq \Delta^2_{\pi^-\to\rho^\circ}$. Here it is seen quite clearly that the assymmetry is associated entirely with the low $\Delta^2_{\pi^-\to\rho^\circ}$ events. It should be noted,

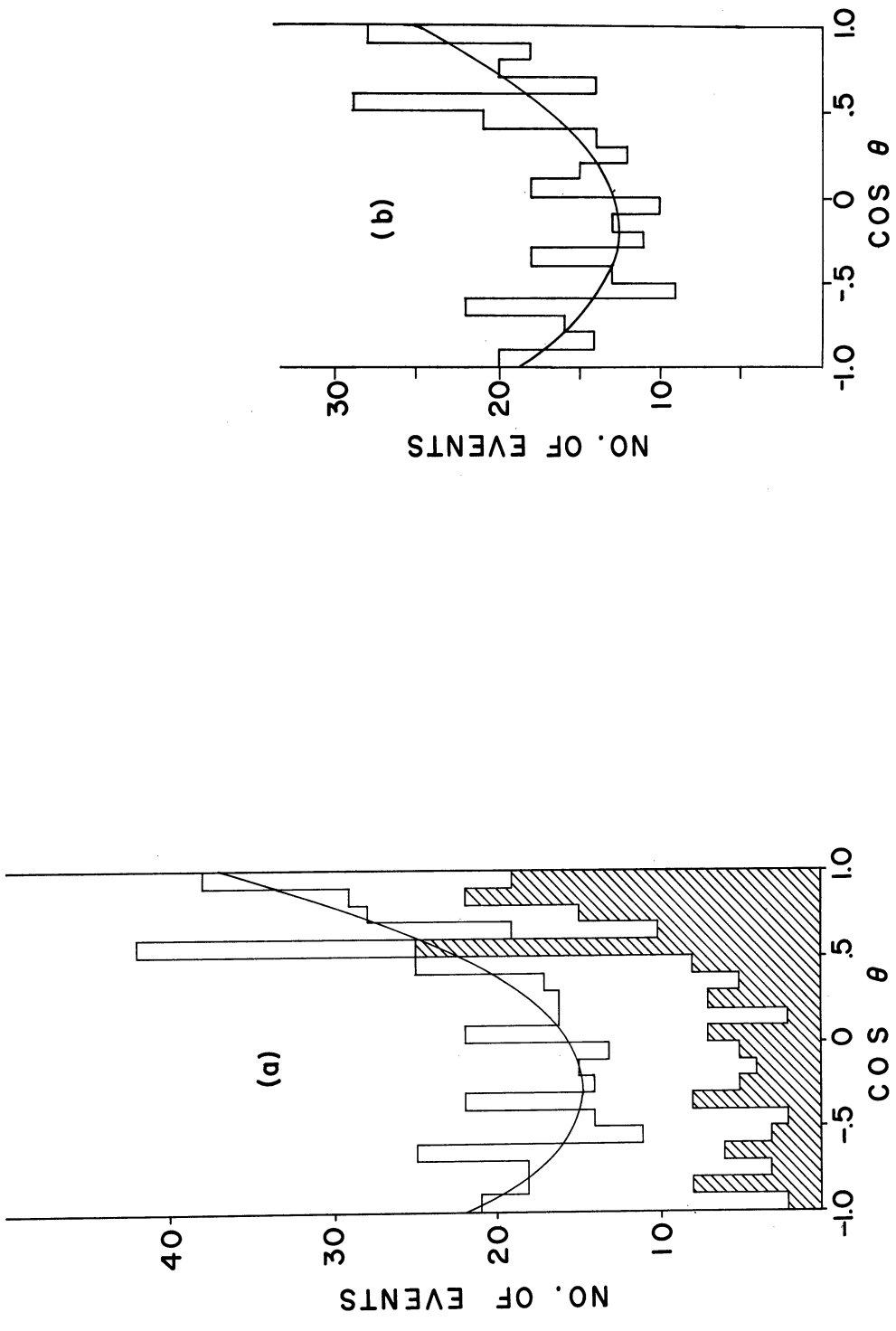

Figure 22. The scattering angle for the π^- in the ρ° center of mass. (a) all events with the $N^*_{3,3}(1238)$ overlap shaded, and (b) after a subtraction of 85 $N^*_{3,3}(1238)$ events.

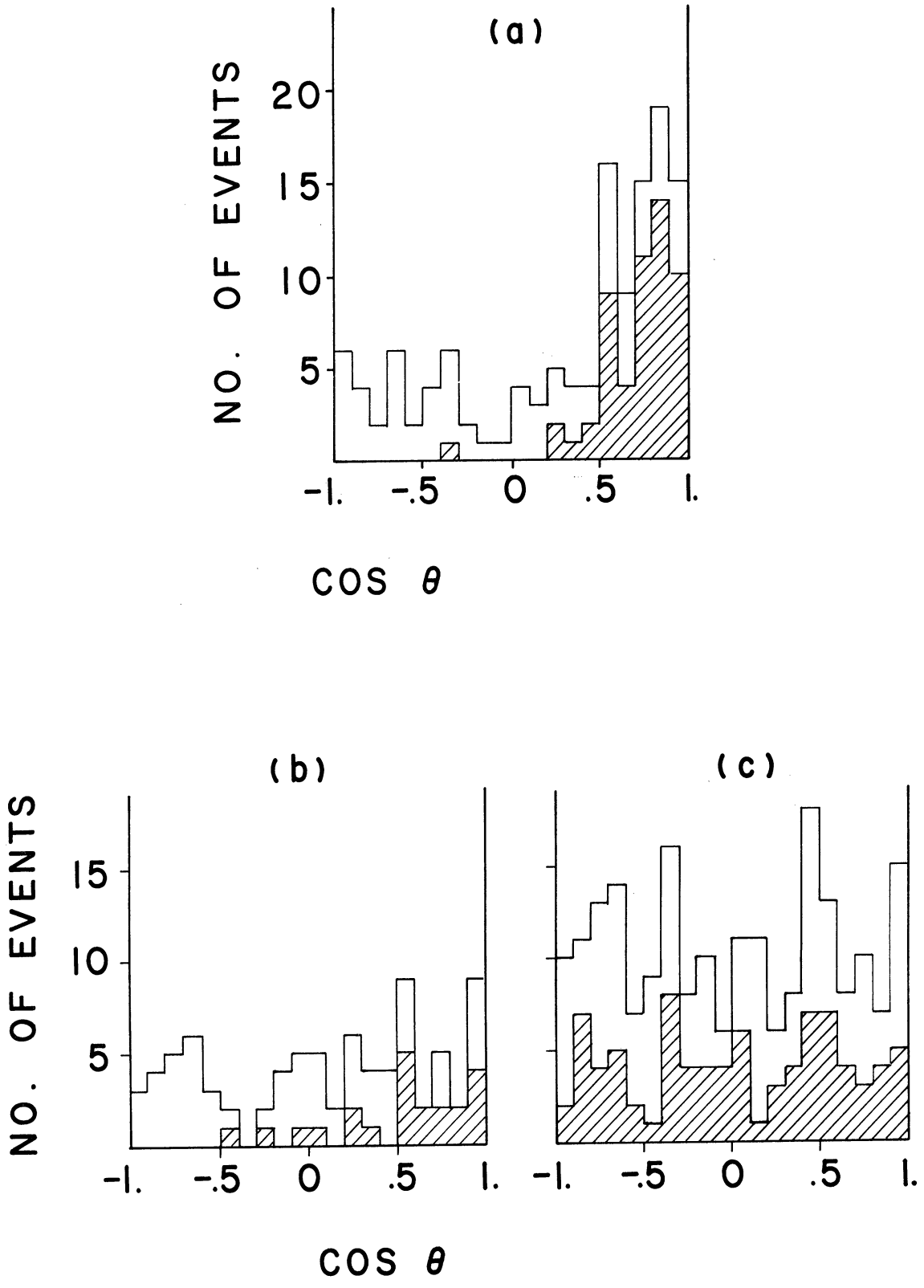

Figure 23. The scattering angle for the π^- in the ρ° center of mass. (a) $\Delta^2_{\pi\to\rho^\circ} < 20M^2_\pi$, (b) $20\ M^2_\pi \leq \Delta^2_{\pi\to\rho^\circ} < 40\ M^2_\pi$, and (c) $\Delta^2_{\pi\to\rho^\circ} \geq 40\ M^2_\pi$.

however, that this is not because the ρ° peak vanishes at higher momentum transfer (see Figures 16(b-d)). This change is probably due to the fact that the treatment of the dipion vertex as a scattering problem is only valid for low $\Delta^2_{\pi^- \to \rho^\circ}$.

In concluding the ρ° scattering discussion, the results of a χ^2 fit to IV.1 for the various distributions are summarized in Table V.

TABLE V

THE RESULTS OF χ^2 FITS TO (IV.1) FOR THE ρ° REGION WITH VARIOUS MOMENTUM TRANSFER CUTOFFS

Comments	A	B	C	χ^2
All events (Fig. 24(a))	15.72 ± 1.43	7.09 ± 1.90	13.18 ± 3.59	23%
All events with 85 $N^*_{3,3}(1238)$ subtractions (Fig. 24(b))	12.98 ± 1.30	3.32 ± 1.68	8.61 ± 3.22	38%
$\Delta^2_{\pi \to \rho} < 20$ (Fig. 25(a))	2.32 ± .65	5.63 ± 1.14	10.01 ± 1.97	57%
$20 \leq \Delta^2_{\pi \to \rho} < 40$ (Fig. 25(b))	2.39 ± .65	.90 ± .83	2.00 ± 1.60	23%
$\Delta^2_{\pi \to \rho} \geq 40$ (Fig. 25(c))	8.91 ± 1.07	-.44 ± 1.31	2.44 ± 2.49	48%

4.5 THE A_1 AND A_2 MESONS

In the past year many different experimental groups[59-61] have presented evidence for two peaks in the $(\rho^\circ,\pi^\pm)$ mass distribution. Their masses are centered at 1090 and 1310 MeV and they are called the A_1 and A_2, respectively. At this time the A_2 is believed to be a true particle state, but there is still some doubt concerning the A_1. The results to be presented here further confuse the status of the A_1, and in addition, introduce some serious questions about the A_2. It will be shown that almost all of the events of reaction (4.2) which satisfy

$$\pi^- + p \rightarrow A_1 + p \tag{4.8}$$

and

$$\rightarrow A_2 + p \tag{4.9}$$

can also be assumed to belong to one of the modes

$$\pi^- + p \rightarrow \rho^\circ + N^*_{3,-1}(1238), \tag{4.6}$$

$$\rightarrow \rho^\circ + N^*_{1,-1}(1512), \tag{4.7}$$

$$\rightarrow \rho^\circ + N^*_{1,-1}(1688), \tag{4.11}$$

and

$$\rightarrow \rho^\circ + N^*_{3,-1}(1920). \tag{4.12}$$

In Figure 24(a) $M_{\rho^\circ\pi^-}$ is shown for all events which satisfy reaction (4.2). Phase space is normalized to the total number of events. In this plot there is some evidence for A_2 production, but the peaking in the A_1 region is not statistically significant. However, when the mass is examined as a function of momentum transfer to the proton, the A mesons become quite prominent. A scattergram of

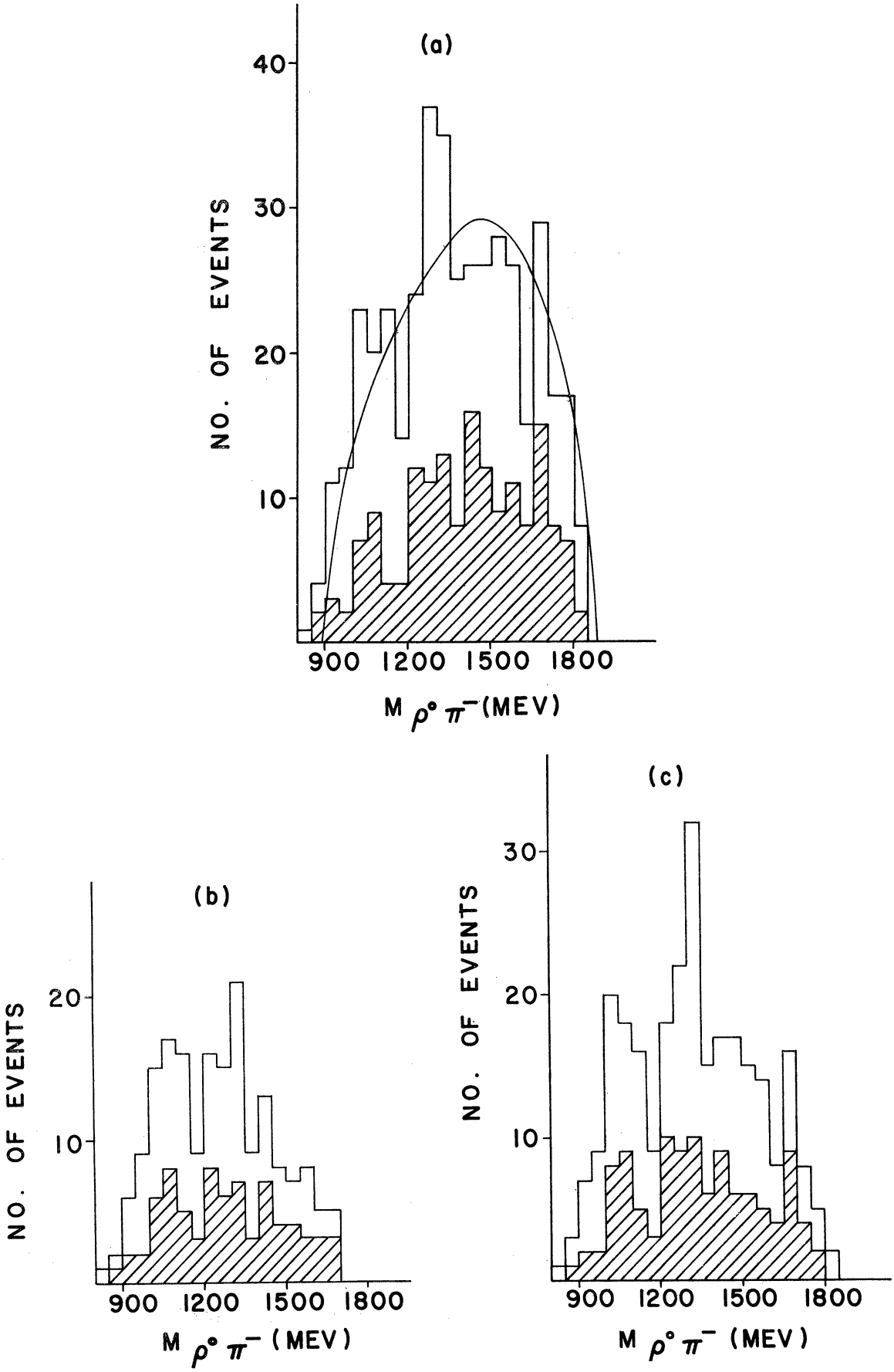

Figure 24. The $M_{\rho^\circ\pi^-}$ distribution for (a) all $\Delta^2_{p\to p}$, (b) $\Delta^2_{p\to p} < .4\ (\text{BeV})^2$. and (c) $\Delta^2_{p\to p} < .8(\text{BeV})^2$. The shaded area represents the $N^*_{3,3}(1238)$ overlap in all histograms.

$\Delta^2_{p\to p}$ vs. $M_{\rho^\circ\pi^-}$ has been studied, and the projections for the regions $\Delta^2_{p\to p} < .40(\text{BeV})^2$ and $\Delta^2_{p\to p} < .80(\text{BeV})^2$ are shown in Figures 24(b) and 24(c). Here a definite enhancement is noticed in the regions corresponding to the two mesons. This is especially evident in Figure 24(c) where $\Delta^2_{p\to p} < .80(\text{BeV})^2$. Since the A mesons cannot be produced by a one-pion-exchange mechanism, it is not too surprising that they appear in large number at higher momentum transfer than do the positive-G- parity particles such as the ρ°.

In addition to the ρ° events, $M_{\pi^-\pi^+\pi^-}$ has also been investigated for the rest of the data in reaction (4.1). It is found that neither of the A peaks exist except for the ρ° sample. Thus both of these resonances can be associated with a (π^-,ρ°) combination rather than a three-pion state.

Of the 129 events in which $\Delta^2_{\pi^-\to\rho^\circ} < 20M^2_\pi$, sixty-six of these also satisfy $1000 \leq M_{\rho^\circ\pi^-} < 1350$ MeV. If it is now recalled that the ρ° mesons produced at low momentum transfer appear to be made with (π^-,p) resonances (see Figure 17(c)), it becomes clear that the A peaks may be drastically affected by these isobars. In Figure 25(a) M_{π^-p} is plotted for all events in which $M_{\rho^\circ\pi^-}$ is in the range 1000-1350 MeV with no momentum transfer cutoff. Here one sees strong evidence for the $N^*_{3,-1}(1238)$ and also the possibility of an $N^*_{1,-1}(1512)$ peak. The M_{π^-p} distribution is shown in Figure 25(b) for the A_1 region ($1000 \leq M_{\rho^\circ\pi^-} < 1150$ MeV) and in Figure 25(c) for the A_2 region

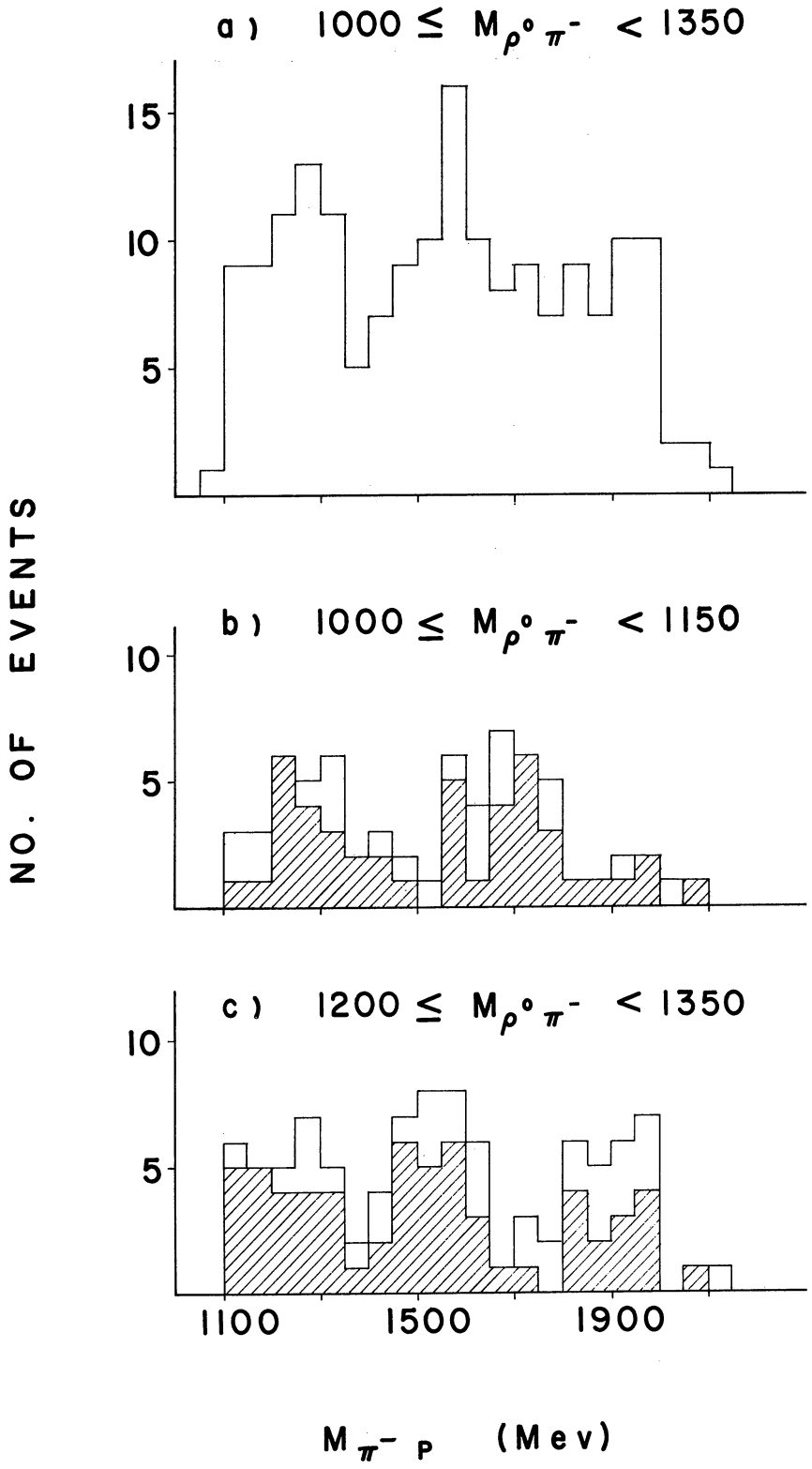

Figure 25. The M_{π}-p distribution when the A_1 and A_2 mesons are produced. (a) $1000 \leq M_{\rho^0\pi^-} < 1350$ MeV, (b) $1000 \leq M_{\rho^0\pi^-} < 1150$ MeV, and (c) $1200 \leq M_{\rho^0\pi^-} < 1350$ MeV. The shaded areas in (b) and (c) represent M_{π}-p after a complete $N^*_{3,3}(1238)$ subtraction.

($1200 \leq M_{\rho^0\pi^-} < 1350$ MeV). Again there is no momentum transfer cutoff. In these two plots there are obvious peaks at many different mass values. Besides the existence of these peaks, the very striking feature of them is their position on the mass axis. All of these are centered close to known pion-nucleon resonances—the 1238 and 1688 MeV isobars in Figure 25(b) and the 1238, 1512, and 1920 MeV isobars in Figure 25(c). Furthermore, these two histograms keep their general shapes when all $N^*_{3,3}(1238)$ events are subtracted (shaded areas*). χ^2 fits to the distributions of Figures 25(b) and 25(c) have been made for various hypotheses. These are summarized below:

a) Figure 25(b)

1) Assuming the phase-space distribution of reaction (4.8), the χ^2 probability is much less than 1%.

2) Assuming the phase space of reaction (4.8) plus some $N^*_{3,-1}(1238)$ with a Breit-Wigner distribution, the maximum χ^2 probability is 3% when there are 28 phase-space and 39 $N^*_{3,-1}(1238)$ events, respectively.

3) Assuming just $N^*_{3,-1}(1238)$ and $N^*_{1,-1}(1688)$, both with Breit-Wigner distributions, the maximum χ^2 probability is 68%. This is obtained assuming 33 events of type (4.6) and 34 events of type (4.11).

b) Figure 25(c)

1) Assuming the phase-space distribution of reaction (4.9), the χ^2 probability is slightly less than 1%.

*The shaded areas in Figures 25(b) and 25(c) represent those events which do not have a mass value in the $N^*_{3,3}(1238)$ peak. This is different than most of the histograms where the shaded area represents those events in the $N^*_{3,3}(1238)$ peak.

2) Assuming the phase space of (4.9) plus some $N^*_{3,-1}(1238)$ and $N^*_{1,-1}(1512)$ with Breit-Wigner distributions, the maximum χ^2 probability is 9%. This is obtained with 30, 28, and 37 events of type (4.9), (4.6), and (4.7), respectively.

3) Assuming just $N^*_{3,-1}(1238)$, $N^*_{1,-1}(1512)$, and $N^*_{3,-1}(1920)$, all with Breit-Wigner distributions, the maximum χ^2 probability is 84%. This is obtained assuming 28, 34, and 33 events of type (4.6), (4.7), and (4.12), respectively.

In Figure 26 a Dalitz plot is shown for the (ρ°,π^-,p) final state. Due to the width of the ρ° there are two boundaries for this plot. These have been fitted together to form a smooth curve which encloses all of the points. Upon close observation it appears that the density of points is unusually high where A meson and isobar bands overlap. This overlap contains so many of the points in the A bands that the regions between the isobars are almost empty (see Figures 25(a) and 25(b)). Both of the A peaks can be attributed entirely to the overlap regions, and additionally, the evidence for isobars is very, very meager outside the A bands. This is not what one would expect from independent (π^-,p) and (π^-,ρ°) resonances.

So far, there is one important point which has been ignored—the A_1 peak just appears when a $\Delta^2_{p\to p}$ cutoff is imposed. If it is assumed that only these low momentum transfer events should be considered, then the $N^*_{1,-1}(1688)$ can be disregarded. $M_{\pi\text{-}p}$ is plotted in Figure 27(a) for just those events in which: (1) $\Delta^2_{p\to p} < .80(\text{BeV})^2$ and (2) $1000 \leq M_{\pi\text{-}\rho^\circ} < 1350$ MeV. Although the other three (π^-,p) peaks

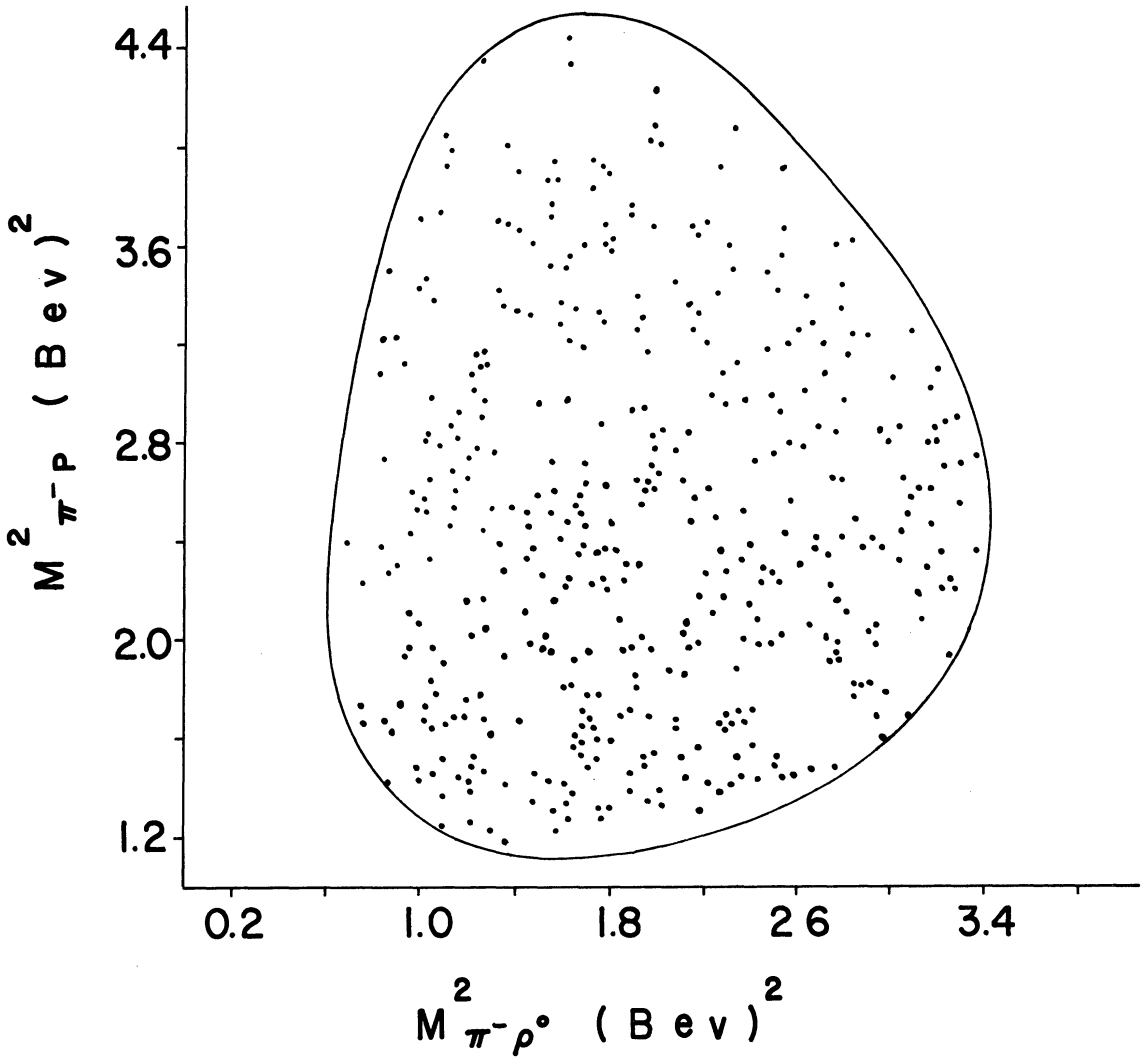

Figure 26. The Dalitz plot for the final state (ρ°,π^-,p).

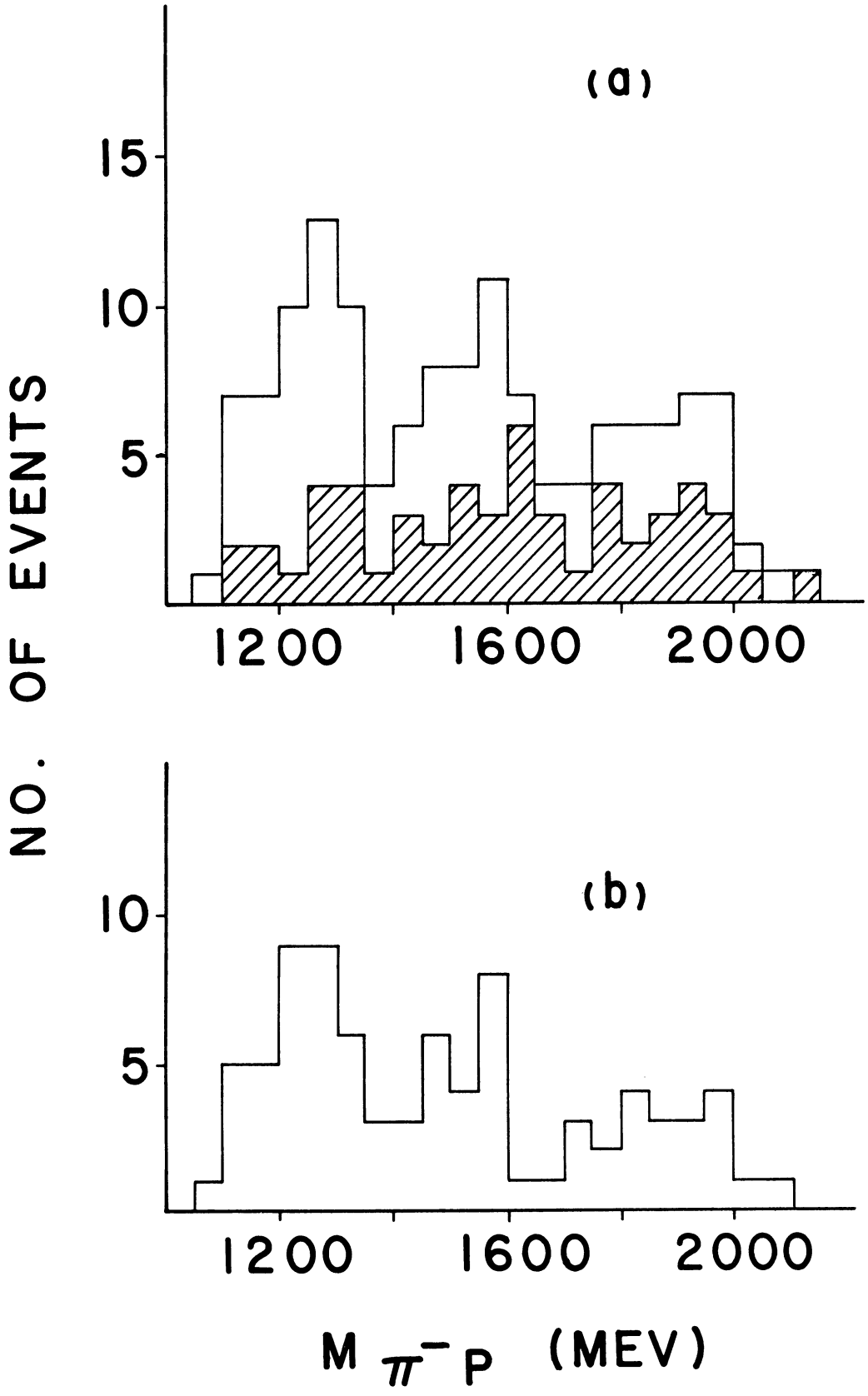

Figure 27. The M_{π^-p} distribution for low momentum transfer ($\Delta^{2}_{\pi^-\to\rho^\circ} < .8$ $(BeV)^2$) to the A mesons ($1000 \leq M_{\rho^\circ\pi^-} < 1350$ MeV). (a) all events of this type, with the shaded area representing the $N^*_{3,3}(1238)$ overlap, and (b) the distribution of (a) with all $N^*_{3,3}(1238)$ events subtracted.

are still evident, it is quite apparent that the 1688 MeV isobar has been completely eliminated by the cutoff.

How the above observations should be interpreted is not at all clear. R. Deck[62] has tried to explain the A_1 as a kinematical consequence of a one-pion-exchange mechanism in reaction (4.2), but in his model the A_2 is considered to be a real particle. The data from this experiment suggests the possibility that both A peaks may be kinematical reflections of reactions (4.6), (4.7), (4.11), and (4.12). But if this is so, why should one isobar produce an M_π-ρ° enhancement around 1090 MeV while another causes the (π^-,ρ°) mass to peak at 1310 MeV? There is no obvious correlation between the isobar and A meson masses. The $N^*_{1,-1}(1512)$ is associated with the A_2, the heavier $N^*_{1,-1}(1688)$ is connected with the A_1, the still heavier $N^*_{3,-1}(1920)$ can be related to the A_2, and the $N^*_{3,-1}(1238)$ can be associated with both A peaks. Furthermore, if this hypothesis is valid, why are A mesons found in the final state (ρ°,π^+,p)?[59] Here the isobar contamination is not bothersome, as the A mesons are still seen after all events of the type

$$\pi^+ + p \rightarrow \rho^\circ + N^*_{3,3}(1238) \rightarrow \pi^+ + p \qquad (4.13)$$

are subtracted, while the 1512 and 1688 MeV resonances do not exist in the (π^+,p) state.

Another possible interpretation is that the A mesons cannot be experimentally separated from the (π^-,p) resonances for the simple

reason that they are not produced independently of the isobars. It could be that the π^- is somehow shared by the ρ° and p in such a way that both the (π^-,p) and (π^-,ρ°) combinations form resonant states in the same physical event. The $N^*_{3,-1}(1238)$, $N^*_{1,-1}(1512)$, and $N^*_{3,-1}(1920)$ are produced in conjunction with the A_2, while the $N^*_{3,-1}(1238)$ and possibly the $N^*_{1,-1}(1688)$ share a π^- with the A_1.

Finally, because of the small number of events involved, one cannot eliminate the possibility that the entire N* effect is no more than a statistical fluctuation. This is especially true for the A_2. It is seen from Figure 25(c) that very few events would be required to change the apparently isobar-dominated distribution to one which follows phase space.

5. THE $N^*_{3,3}(1238)$ CHANNEL

5.1 Introduction

In this section the analysis will be devoted to the reaction

$$\pi^- + p \rightarrow \pi^- + \pi^- + N^*_{3,3}(1238) \qquad (4.3)$$
$$\rightarrow \pi^+ + p.$$

Using the one-pion-exchange model,[11] the (π^-,π^-) scattering cross section $\sigma_{\pi^-\pi^-}$ will be calculated as a function of center-of-mass energy by means of the Salzman-Salzman[63] approximation to the Chew-Low[32] formula. The differential cross section will also be investigated, but because of a statistically insufficient sample, no attempt will be made to extrapolate this to the pole at $\Delta^2_{p\rightarrow N^*_{3,3}} = M_\pi^2$.

5.2 The $(\pi^-,\pi^-,N^*_{3,3}(1238))$ Masses

For this reaction there are only two mass combinations to be studied. $M_{\pi^-\pi^-}$ and $M_{\pi^-N^*_{3,3}}$ are shown in Figures 28(a) and 28(b), respectively. It is obvious that both distributions follow phase space quite closely. This is also true when momentum transfer cutoffs are imposed. The shaded areas in both plots correspond to the ρ° overlap. Since only forty-five of these actually belong to the ρ° channel (see Section 2.), it is clear that this contamination does not affect the conclusions derived from either histogram.

5.3 A Study of the (π^-,π^-) Elastic-Scattering Cross Section

As a first step in this study, it is necessary to examine the validity of the one-pion-exchange model of Figure 3(a) as the proper tool for analyzing reaction (4.3). In Figure 29 the $\Delta^2_{p\to N^*_{3,3}}$ distribution is presented. This shows a strong accumulation of events at low momentum transfer and is therefore consistent with the model. The Trieman-Yang angle for the dipion system is plotted in Figures 30(a) and 30(b) as a function of $\Delta^2_{p\to N^*_{3,3}}$ and $M_{\pi^-\pi^-}$, respectively. Both of these indicate a definite sparseness of points in the region of 90°, an effect which is found to be independent of $\Delta^2_{p\to N^*_{3,3}}$ and dependent on $M_{\pi^-\pi^-}$. At mass values above approximately 900 MeV the Trieman-Yang distribution is quite isotropic, while for the mass region $M_{\pi^-\pi^-} < 900$ MeV it is peaked at 0° and 180°, a result which still persists when only the low momentum transfer events are considered. Finally,

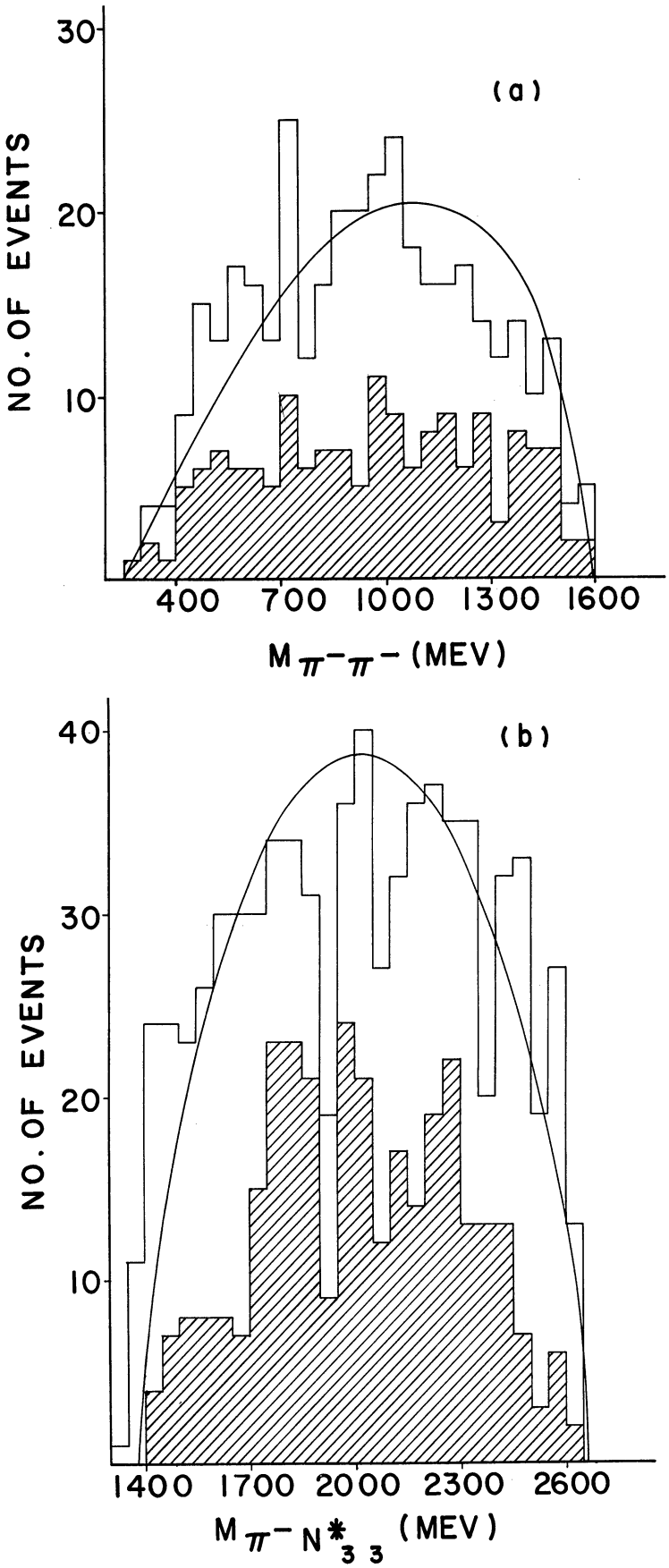

Figure 28. $M_{\pi^-\pi^-}$ and $M_{\pi^-N^*_{3,3}}$ for the final state $(\pi^-,\pi^-,N^*_{3,3}(1238))$. The shaded areas correspond to the ρ° overlap.

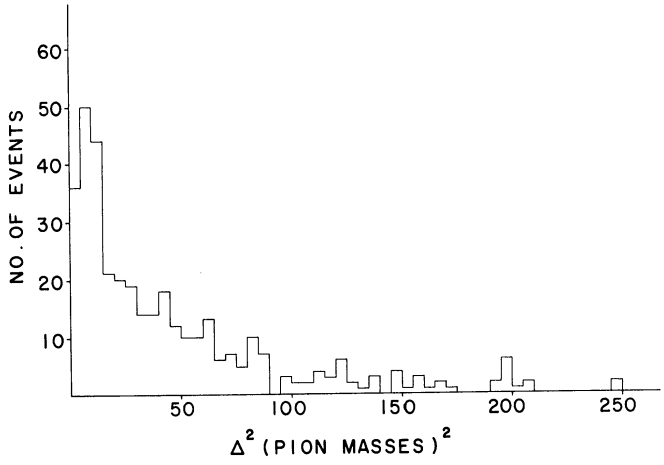

Figure 29. $\Delta^2_{p\to N^*_{3,3}}$ for the $(\pi^-,\pi^-,N^*_{3,3}(1238))$ final state.

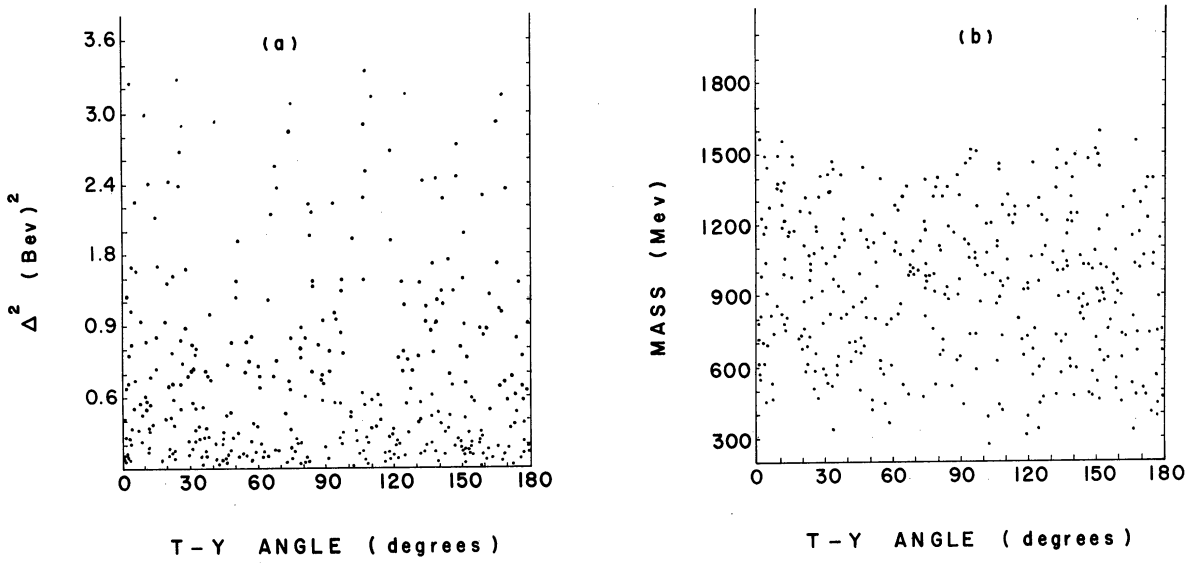

Figure 30. The Trieman-Yang angle for the negative pions in the final state $(\pi^-,\pi^-,N^*_{3,3}(1238))$. (a) $\Delta^2_{p\to N^*_{3,3}}$ vs. TY angle, and (b) $M_{\pi^-\pi^-}$ vs. TY angle.

a subtraction of the ρ° contamination does not change the above conclusions significantly, because these show almost the same Trieman-Yang distribution as do the non- ρ° events.

Because of the relatively poor Trieman-Yang test the following calculations, which are based on the unmodified one-pion-exchange model, must be regarded with considerable suspicion at low dipion masses. It is worth noting, however, that identical experiments[14,15] at different beam momenta have found a more isotropic distribution, and the poor result found here could, therefore, be more statistical than physical.

The method which will be used to compute $\sigma_{\pi^-\pi^-}$ was first proposed by Chew and Low.[32] Their procedure uses information obtained from a beam interaction on an unstable target particle to analyze the scattering properties of the target's "decay products." Thus it is possible to study the scattering processes

$$\pi^- + \pi^- \rightarrow \pi^- + \pi^- \tag{4.14}$$

and

$$\pi^+ + p \rightarrow N^*_{3,3}(1238) \rightarrow \pi^+ + p \tag{4.15}$$

in terms of reaction (4.3), provided the one-pion-exchange diagram of Figure 3(a) can be assumed. According to Chew and Low, the total cross section for reaction (4.3) is given in terms of $\sigma_{\pi^+p}(\Delta^2, W)$ and $\sigma_{\pi^-\pi^-}(\Delta^2, V)$ by

$$\frac{\partial^3 \sigma_{\pi^-\pi^-N^*}}{\partial\Delta^2\partial V^2\partial W^2} = \lim_{\Delta^2\to-\mu^2} \frac{1}{16\pi^3 k^2 M^2}\ \sigma_{\pi^-\pi^-}(\Delta^2,V)\ \frac{k_V V}{(\Delta^2+\mu^2)^2}\ . \qquad \text{(IV.3)}$$

$$\times\ \sigma_{\pi^+p}(\Delta^2,W) k_W W,$$

where V is $M_{\pi^-\pi^-}$, W is M_{π^+p}, μ is the pion mass, k is the momentum of the incident pion in the laboratory, k_V is the momentum of one of the pions in the (π^-,π^-) rest frame, k_W is the momentum of the proton in the (π^+,p) rest frame, M is the mass of the target nucleon, and Δ^2 is $\Delta^2_{p\to N^*_{3,3}}$. In the limit $\Delta^2\to-\mu^2$, $\sigma_{\pi^-\pi^-}(\Delta^2,V)$ and $\sigma_{\pi^+p}(\Delta^2,W)$ approach the values $\sigma_{\pi^-\pi^-}(V)$ and $\sigma_{\pi^+p}(W)$ which are the real total elastic cross sections at the energies V and W.

With the aid of the experimentally determined value for $\sigma_{\pi^+p}(W)$ and a careful measurement of the quantity $(\Delta^2+\mu^2)\cdot(\partial^3\sigma_{\pi^-\pi^-N^*}/\partial\Delta^2\partial V^2\partial M^2)$ for given values of V and M, it is possible to find $\sigma_{\pi^-\pi^-}(V)$ by means of an extrapolation to the pole at $\Delta^2 = -\mu^2$. However, in order to do this a prohibitively large number of events is required, and it is therefore necessary to resort to certain approximations which make Formula IV.3 applicable in the physical region without the limit. One such approximation is furnished by Salzman and Salzman.[63] They suggest that Formula IV.3 can be applied at low Δ^2 when the substitutions

$$\sigma_{\pi^+p}(\Delta,W) = \left[\frac{(W-M)^2+\Delta^2}{(W-M)^2-\mu^2}\right]\sigma_{\pi^+p}(W)$$

and $\qquad \text{(IV.4)}$

$$\sigma_{\pi^-\pi^-}(\Delta^2,V) = \sigma_{\pi^-\pi^-}(V)$$

are made and the limit is ignored. These approximations are made in an attempt to correct for the fact that the exchanged pion is virtual and does not behave as a real particle except at $\Delta^2 = -\mu^2$. With these assumptions the Chew-Low formula can now be written

$$\frac{\partial^3 \sigma_{\pi^-\pi^-N^*}}{\partial\Delta^2 \partial W^2 \partial V^2} = \left(\frac{1}{16\pi^3 k^2 M^2}\right) \cdot V \cdot \left(\frac{V^2}{4} - \mu^2\right)^{1/2} \cdot W \cdot \left[\left(\frac{W^2+\mu^2-M^2}{2W}\right)^2 - \mu^2\right]^{1/2} \cdot \tag{IV.5}$$

$$\times \left(\frac{1}{\Delta^2+\mu^2}\right)^2 \cdot \left[\frac{(W-M)^2+\Delta^2}{(W-M)^2-\mu^2}\right] \sigma_{\pi^+p}(W)\sigma_{\pi^-\pi^-}(V).$$

To find $\sigma_{\pi^-\pi^-}(V)$ all that is needed is to integrate the right-hand side of IV.5 over Δ^2 and W^2. The W^2 range of integration is $1130 \leq W < 1330$ MeV, and the Δ^2 region extends from a lower limit dependent on W to an upper limit which is determined by the Δ^2 cutoff. For $\sigma_{\pi^+p}(W)$ a Breit-Wigner fit to the experimental cross section[64] is used. After performing the double integration the expression

$$\frac{d\sigma_{\pi^-\pi^-N^*}}{dV^2} = K\, \sigma_{\pi^-\pi^-}(V^2) \tag{IV.6}$$

is obtained, where K is just a number. From the experimental values for $(d\sigma_{\pi^-\pi^-N^*}(V^2)/dV^2)$ it is now possible to determine $\sigma_{\pi^-\pi^-}(V^2)$. The results of this determination are shown in Figure 31(a) for two upper limits on Δ^2: $\Delta^2 < 20\mu^2$ and $\Delta^2 < 40\mu^2$. The corresponding histograms for $(d\sigma_{\pi^-\pi^-N^*}(V^2)/dV^2)$ are shown in Figure 31(b). These results are in good agreement with those obtained by N. Schmitz[15] and a Saclay-Orsay-Bari-Bologna collaboration.[14] Both of these experiments used the same final state considered here with π^- beam momenta of 4.00 BeV/c

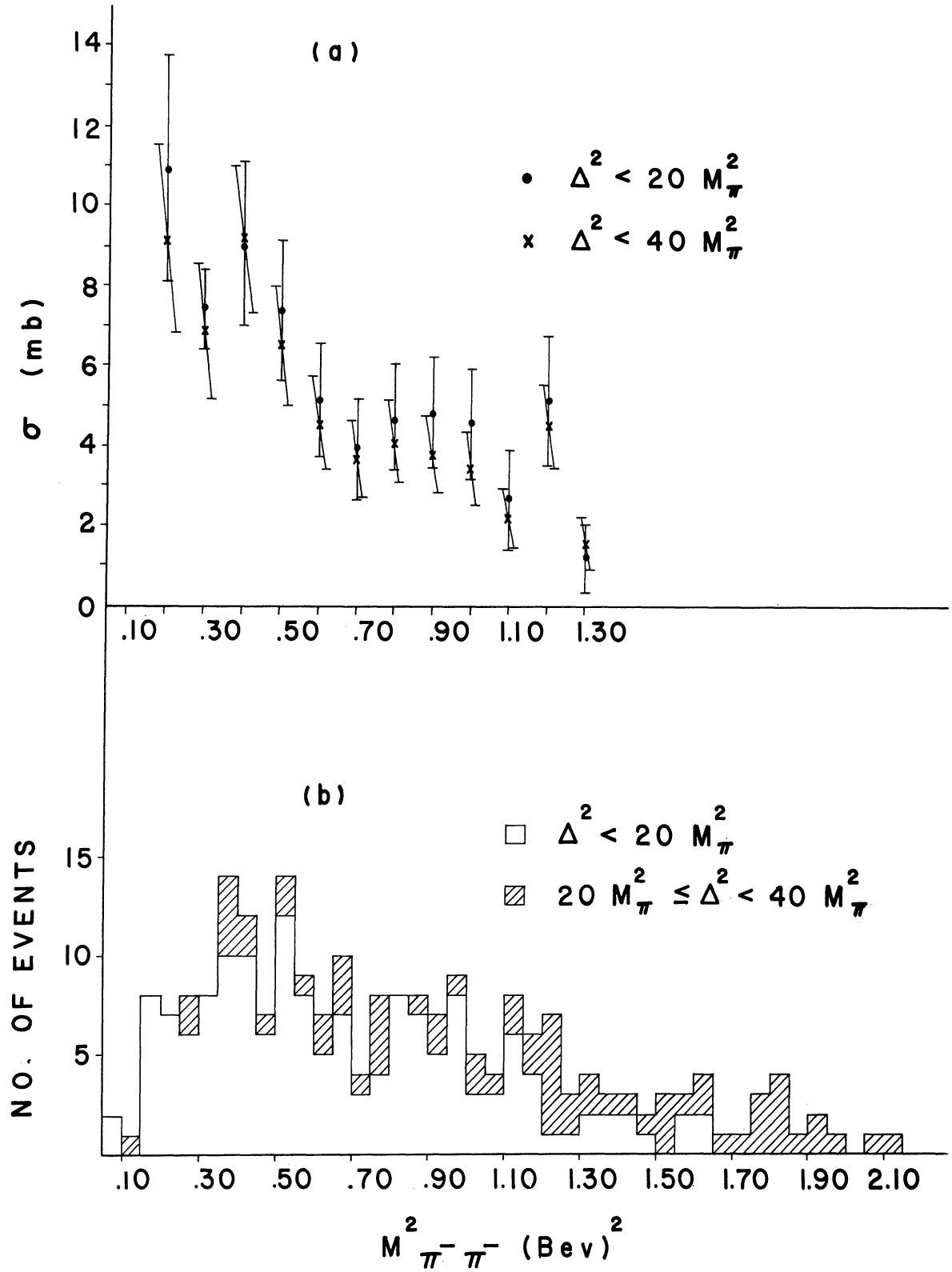

Figure 31. The (π^-,π^-) cross section as a function of center-of-mass energy.

and 2.75 BeV/c, respectively. The calculations of Schmitz were also based on the Salzman-Salzman formula, and the other group used the expression given by Ferrari and Selleri[65] for the nucleon-vertex approximation.

5.4 The (π^-,π^-) Scattering Angle Distribution

Let it be assumed that reaction (4.3) is governed by the one-pion-exchange model and that the exchanged π^- is real. Then, since the generalized Pauli Principle requires that even isotopic spin be accompanied by even angular momentum, the differential cross section for (π^-,π^-) scattering can be written

$$\frac{d\sigma}{d(\cos\Theta)} = \frac{2\pi}{k^2}\left|\sum_{\ell=\text{even}}(2\ell+1)e^{i\delta_\ell}\sin\delta_\ell\, P_\ell(\cos\Theta)\right|^2 \qquad \text{(IV.7)}$$

Although this expression is valid only in the limit $\Delta^2_{p\to N^*_{3,3}} = -M_\pi^2$, it will be applied in the physical region at low momentum transfer. The statistical sample is just too small to attempt a more refined calculation based on an extrapolation to the pole. Also, all angular momenta greater than L = 2 will be ignored. This allows (IV.7) to be written in the form

$$\frac{d\sigma}{d(\cos\Theta)} = A + B\cos^2\Theta + C\cos^4\Theta, \qquad \text{(IV.8)}$$

where

$$A = \sin^2\delta_0 + 25/4\cdot\sin^2\delta_2 - 5\cdot\cos(\delta_2-\delta_0)\cdot\sin\delta_2\sin\delta_0,$$

$$B = -75/2\,\sin^2\delta_2 + 15\cos(\delta_2-\delta_0)\sin\delta_2\sin\delta_0,$$

and

$$C = 225/4 \sin^2\delta_2.$$

In Figures 32(a-e) the cos Θ distribution is shown for five $M_{\pi^-\pi^-}$ regions: (1) 280-500 MeV, (2) 500-700 MeV, (3) 700-900 MeV, (4) 900-1200 MeV, (5) $M_{\pi^-\pi^-} \geq$ 1200 MeV. These regions are chosen simply to agree with those picked by the European collaboration[14] at a beam momentum of 2.75 BeV/c. The first two distributions are isotropic, and the next two show an increasing dependence on the cos Θ terms. This indicates that higher angular momentum states reach significant proportions at approximately 800 MeV. The last mass region shows a drop in the cos Θ dependence, but this is probably a consequence of poor statistics rather than a physical effect. These results agree very well with other experiments[14,66] which have studied $\vec{T}$=2 scattering in this reaction and also in the reaction

$$\pi^+ + p \rightarrow \pi^+ + \pi^+ + n. \qquad (4.16)$$

The summary of a χ^2 fit to the data for the curve represented by (IV.8) is given in Table VI.

From the table below it is seen that the errors in the fitted coefficients are very large. This, coupled with the fact that the coefficients cannot be evaluated at $\Delta^2 = -M_\pi^2$, makes it impossible to compute the phase shifts δ_0 and δ_2. It is probably safe to conclude that δ_2 does become significant at approximately 800 MeV, but nothing can be said with any certainty about its sign or magnitude.

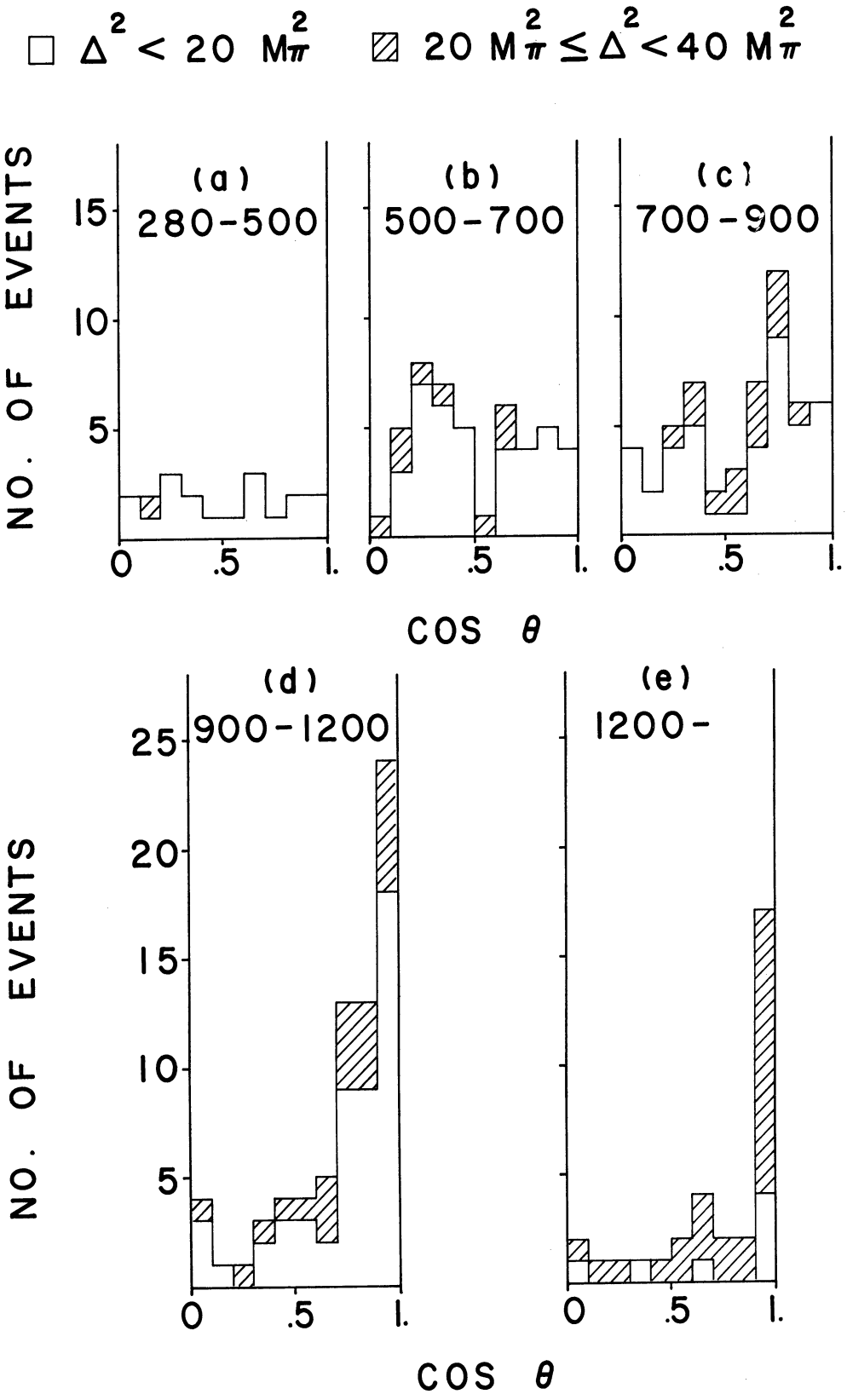

Figure 32. The π^- scattering angle in the (π^-,π^-) center of mass for (a) $280 \leq M_{\pi^-\pi^-} < 500$, (b) $500 \leq M_{\pi^-\pi^-} < 700$, (c) $700 \leq M_{\pi^-\pi^-} < 900$. (d) $900 \leq M_{\pi^-\pi^-} < 1200$, and (e) $1200 \leq M_{\pi^-\pi^-} < 1670$.

TABLE VI

THE RESULTS OF χ^2 FITS TO (IV.8) FOR VARIOUS $M_{\pi^-\pi^-}$ REGIONS

Mass (MeV)	a) $\Delta^2 p \to N^*_{3,3} < 20\ M_\pi^2$				b) $\Delta^2 p \to N^*_{3,3} < 40\ M_\pi^2$			
	A	B	C	χ^2	A	B	C	χ^2
280-500	1.7±1.0	-1.8±6.2	2.4± 7.1	97%	2.2±1.1	-3.7±6.4	4.1± 7.2	98%
500-700	1.2± .9	1.1±5.8	3.1± 7.1	2%	2.9±1.2	1.8±7.4	-0.1± 8.5	12%
700-900	2.9±1.2	-5.3±7.9	11.3± 9.2	40%	2.8±1.3	6.9±9.0	-2.8±10.3	32%
900-1200	1.2±0.9	-4.3±8.1	23.8±11.1	65%	1.7±1.1	0.1±9.5	25.7±12.9	83%
1200-1670	0.5±0.7	-3.8±4.9	5.7±6.2	88%	1.7±1.0	-6.8±7.6	15.2±10.0	26%

6. PRODUCTION ANGLES

With the knowledge that both the ρ° and $N^*_{3,3}(1238)$ are produced in peripheral interactions, the distributions of the production angles for the individual particles of reaction (4.1) are exactly what one would expect. These are shown in Figures 33-35 in the following order:

1) Figure 33—This corresponds to all events.
(a) the π^-, (b) the p, (c) the π^+.

2) Figure 34—This corresponds to just those events in which an $N^*_{3,3}(1238)$ is produced. The shaded area represents the ρ° overlap. (a) the π^-, (b) the p, (c) the π^+.

3) Figure 35—This corresponds to just those events in which a ρ° is produced. The shaded area represents the $N^*_{3,3}(1238)$ overlap. (a) the π^- associated with the ρ°, (b) the π^- not associated with the ρ°, (c) the p, (d) the π^+.

Since both ρ° and $N^*_{3,3}(1238)$ production involve an incident π^- at the upper vertex and a proton at the lower vertex in the one-pion-exchange model, the π^- has a strong forward preference and the proton likes the backward direction. The π^- is not peaked as strongly as the proton because of the extra π^- whose production angle is fairly random in both the ρ° and $N^*_{3,3}(1238)$ channels. The π^+ distribution is quite flat, because the π^+ is produced slightly in the forward direction for the ρ° channel and slightly backward for the $N^*_{3,3}(1238)$ reaction.

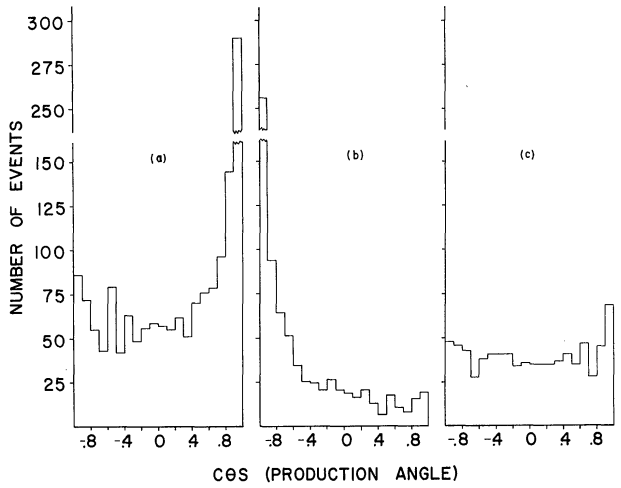

Figure 33. Particle production angles for the $\pi^- + p \rightarrow \pi^- + \pi^- + \pi^+ + p$ reaction.

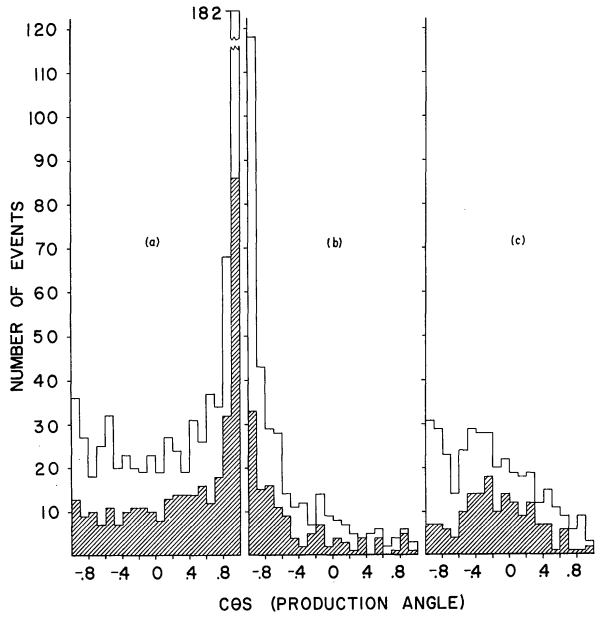

Figure 34. Particle production angles for the $\pi^- + p \rightarrow \pi^- + \pi^- + N^*_{3,3}(1238)$ reaction.

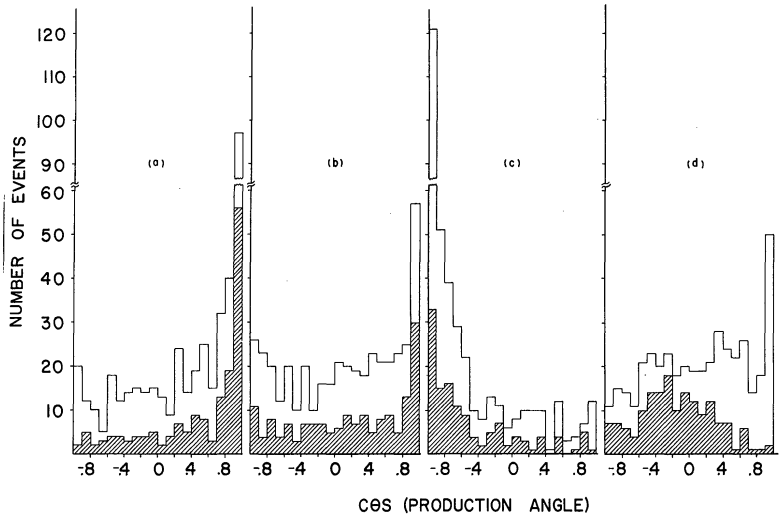

Figure 35. Particle production angles for the $\pi^- + p \rightarrow \pi^- + p + \rho^\circ$.

CHAPTER V

THE REACTION $\pi^- + p \rightarrow \pi^- + \pi^- + \pi^+ + p + \pi^\circ$

1. INTRODUCTION

Here the report will be almost entirely devoted to the ω° and ρ^- mesons. There will be strong evidence presented which indicates that both of these resonances are produced in quasi two - body reactions via the modes

$$\pi^- + p \rightarrow \rho^- + N^* \qquad (5.1)$$

and

$$\rightarrow \omega^\circ + N^*. \qquad (5.2)$$

These initial two - body states then decay through various channels to the final five - particle state. There will also be some discussion of the B meson which is produced in the reaction

$$\pi^- + p \rightarrow p + B^- \rightarrow \pi^- + \omega^\circ. \qquad (5.3)$$

2. THE MASS PLOTS

From the five particles produced in the reaction

$$\pi^- + p \rightarrow \pi^- + \pi^- + \pi^+ + p + \pi^\circ, \qquad (5.4)$$

eighteen different mass combinations can be constructed. The mass spectra for all of these have been investigated for the following cases: (1) all events, (2) low momentum transfer, (3) all ω° events subtracted, (4) all ω° and ρ^- events subtracted, (5) with and without the 121 events ambiguous with the neutron final state. In addition to the four to be

discussed below, only the (π^-,p) and (π°,p) combinations show any evidence for resonance production. In both of these cases there is a slight peaking in the region of the 1238 MeV isobar, while all other plots follow phase space quite closely.

$M_{\pi^-\pi^\circ}$, M_{π^+p}, $M_{\pi^-\pi^+\pi^\circ}$, and $M_{\pi^-\pi^+p}$ are shown in Figures 36 and 37 with the ambiguous events plotted separately. The shaded areas in each histogram correspond to the ω° events, and therefore, the unshaded areas represent the various distributions after a complete ω° subtraction. $M_{\pi^-\pi^+\pi^\circ}$ shows a very strong ω° peak centered at 790 MeV, $M_{\pi^-\pi^\circ}$ peaks in the region (750 MeV) of the ρ^- meson, and M_{π^+p} shows a definite enhancement corresponding to the 1238 MeV isobar. Although $M_{\pi^-\pi^+p}$ seems to follow phase space, it will be seen later that there is a definite structure associated with this distribution when the analysis is restricted to just the ρ^- events.

3. THE ω° PEAK

3.1 The ω° Cross Section

All events in which at least one (π^-,π^+,π°) mass value falls in the range 760-820 MeV are defined to belong to the ω° sample. In those cases where both (π^-,π^+,π°) mass combinations satisfy the ω° definition, the method of Chapter III, Section 5 is used to choose one of the two as the ω°. Upon fitting the ω° peak to a Breit-Wigner distribution, the central mass is found to be $M_{\omega^\circ} = 789\pm2$ MeV, which is about 6 MeV

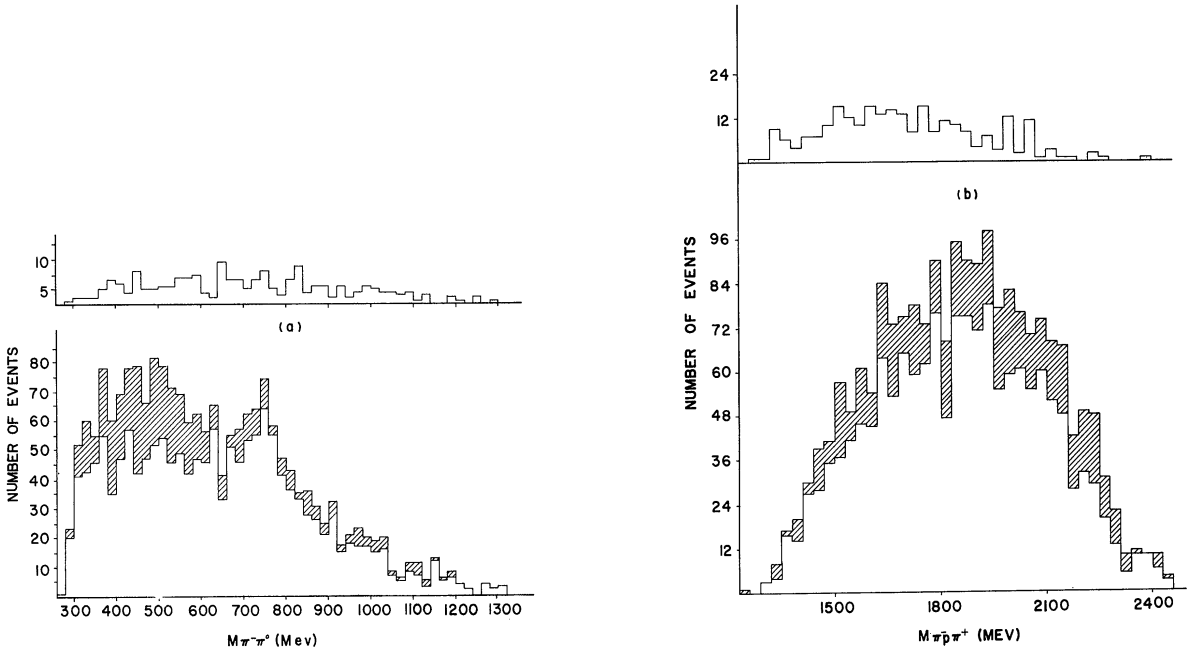

Figure 36. $M_{\pi^-\pi^\circ}$ and $M_{\pi^+ p}$ for the final state $(\pi^-,\pi^-,\pi^+,p,\pi^\circ)$. The shaded areas represent the ω° events. The upper histograms represent those events ambiguous with the final state $(\pi^-,\pi^-,\pi^+,\pi^+,n)$.

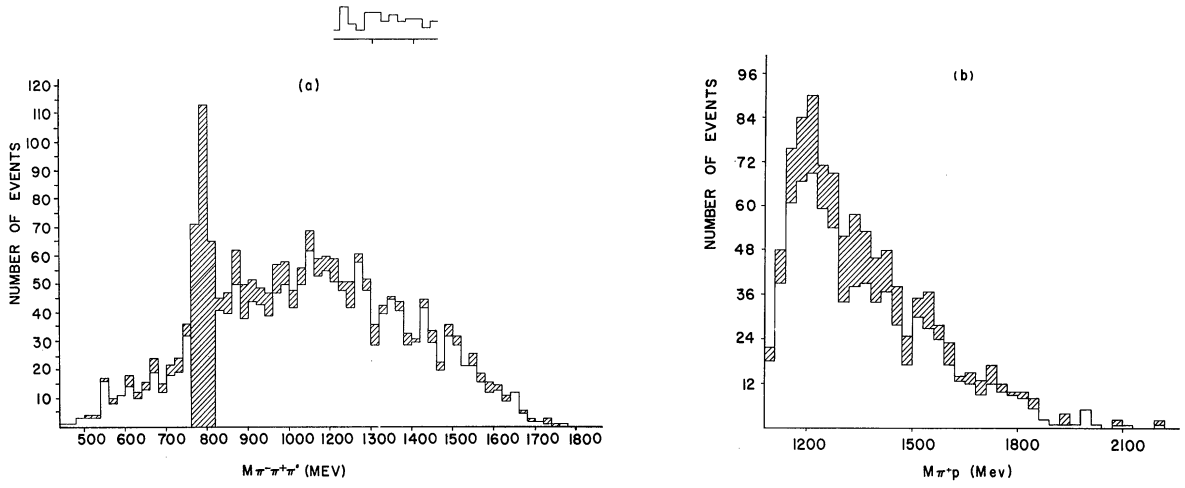

Figure 37. $M_{\pi^-\pi^+\pi^\circ}$ and $M_{\pi^-\pi^+ p}$ for the final state $(\pi^-,\pi^-,\pi^+,p,\pi^\circ)$. The shaded areas represent the ω° events. The upper histograms represent those events ambiguous with the final state $(\pi^-,\pi^-,\pi^+,\pi^+,n)$.

higher than the accepted value.[10] The fitted full width at half maximum is $\Gamma = 36 \pm 4$ MeV. This, of course, is larger than the ω°'s true width because of experimental errors in the mass computations (see Chapter III, Section 4).

The cross section for ω° production through this reaction is estimated to be $\sigma = .28 \pm .04$ mb. This is found by counting the number of events above a smooth background (unshaded area) of Figure 37(a) and then correcting for the double - ω° events. This correction is made by simply taking the total number (142) of ω°'s above phase space and then determining experimentally the number (7) of double - ω°'s in this sample. This cross section, of course, is just for the three - pion decay and is not corrected for neutral modes which are responsible for approximately 10% of the ω° decays.

3.2 The Spin and Parity of the ω°

Since the spin and parity of the ω° are well-known ($J^P = 1^-$), and since the results from this experiment confirm these assignments, only a brief description of the spin-parity analysis will be presented here.

The spin-parity determination is based on the method used by M.L. Stevenson et al.[67] This involves a study of the distribution of points inside the Dalitz plot shown in Figure 38. If the ω° isotopic spin is assumed to be zero and the decay matrix elements are restricted to the simplest ones possible—that is, low internal angular momentum

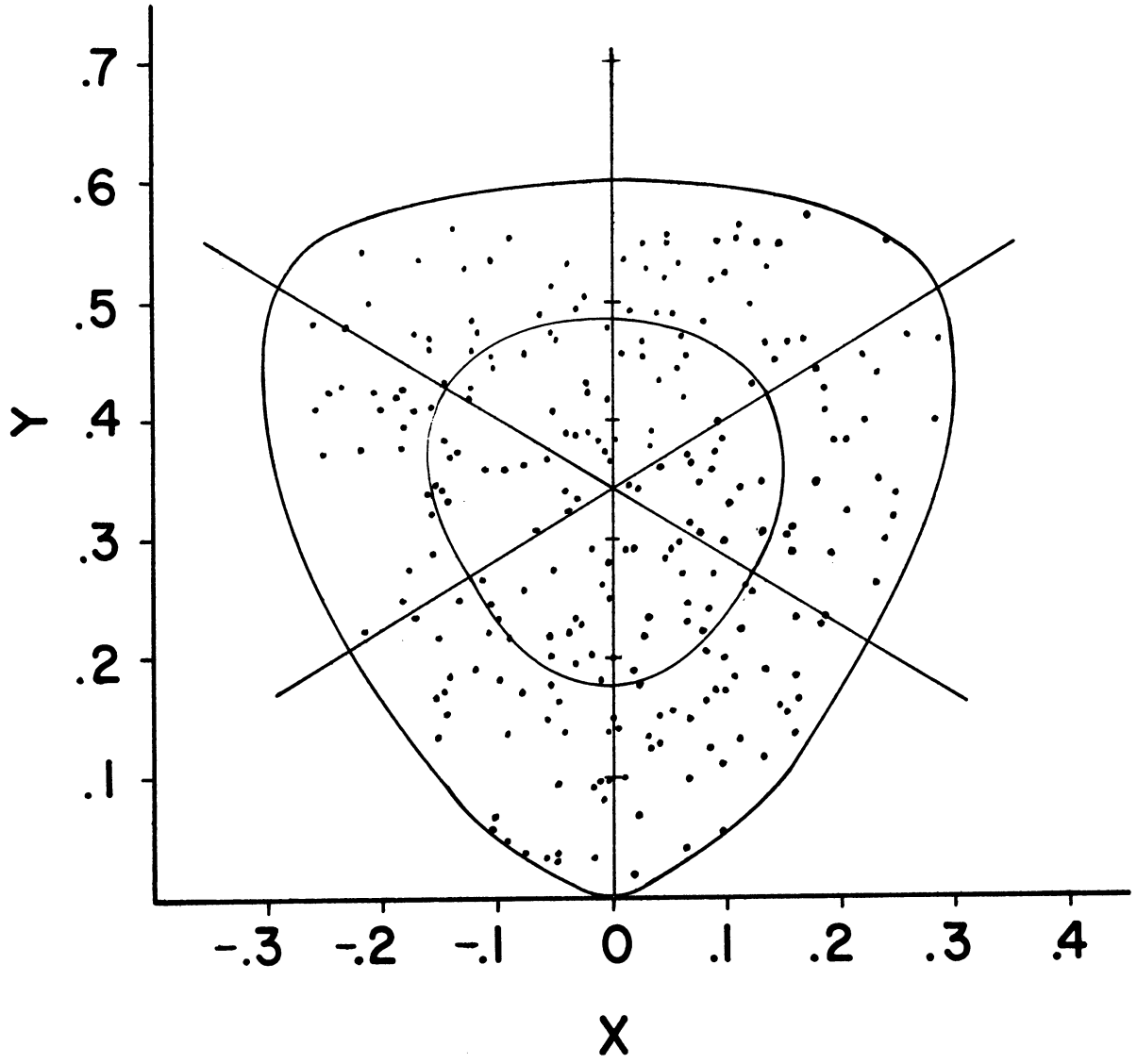

Figure 38. Dalitz plot for the ω° events. $X=(T_{\pi^-} - T_{\pi^+})/\sqrt{3}\ Q$, $Y = T_{\pi^\circ}/Q$, and $Q = T_{\pi^+} + T_{\pi^-} + T_{\pi^\circ}$.

states for the decay pions—then for the assignments $J^P = 0^-$, 1^-, 1^+, 2^-, 2^+, only $J^P = 1^-$ requires a nonzero density at the center of the Dalitz plot. The $J^P = 0^+$ possibility can be ignored because decay into three pions is impossible for such a state if parity is to be conserved.

In Figure 38 a finite population near the center of the plot is seen, and the data is therefore only consistent with $J^P = 1^-$. This is further confirmed upon investigation of the density distribution versus the distance from the center of the Dalitz plot. This has been compared with the predictions for the various assignments and clearly favors $J^P = 1^-$.

Although there are approximately 115 phase-space events in the ω° sample, they do not introduce any serious problems. Because the $J^P = 1^-$ distribution is so much different than that for any other assignment tested, the background could not possibly influence the data to the extent that an incorrect spin-parity determination would result. If the ω° were, for example, a $J^P = 1^+$ particle, the background would probably make it impossible to distinguish between the 1^+ and 0^- assignments, but fortunately, that is not the case.

3.3 The Mass Spectra for the (ω°, π^-, p) State

The Dalitz plot for the reaction

$$\pi^- + p \rightarrow \pi^- + p + \omega^\circ \qquad (5.5)$$

is presented in Figure 39(a). $M^2_{\pi^- p}$ is represented by the horizontal

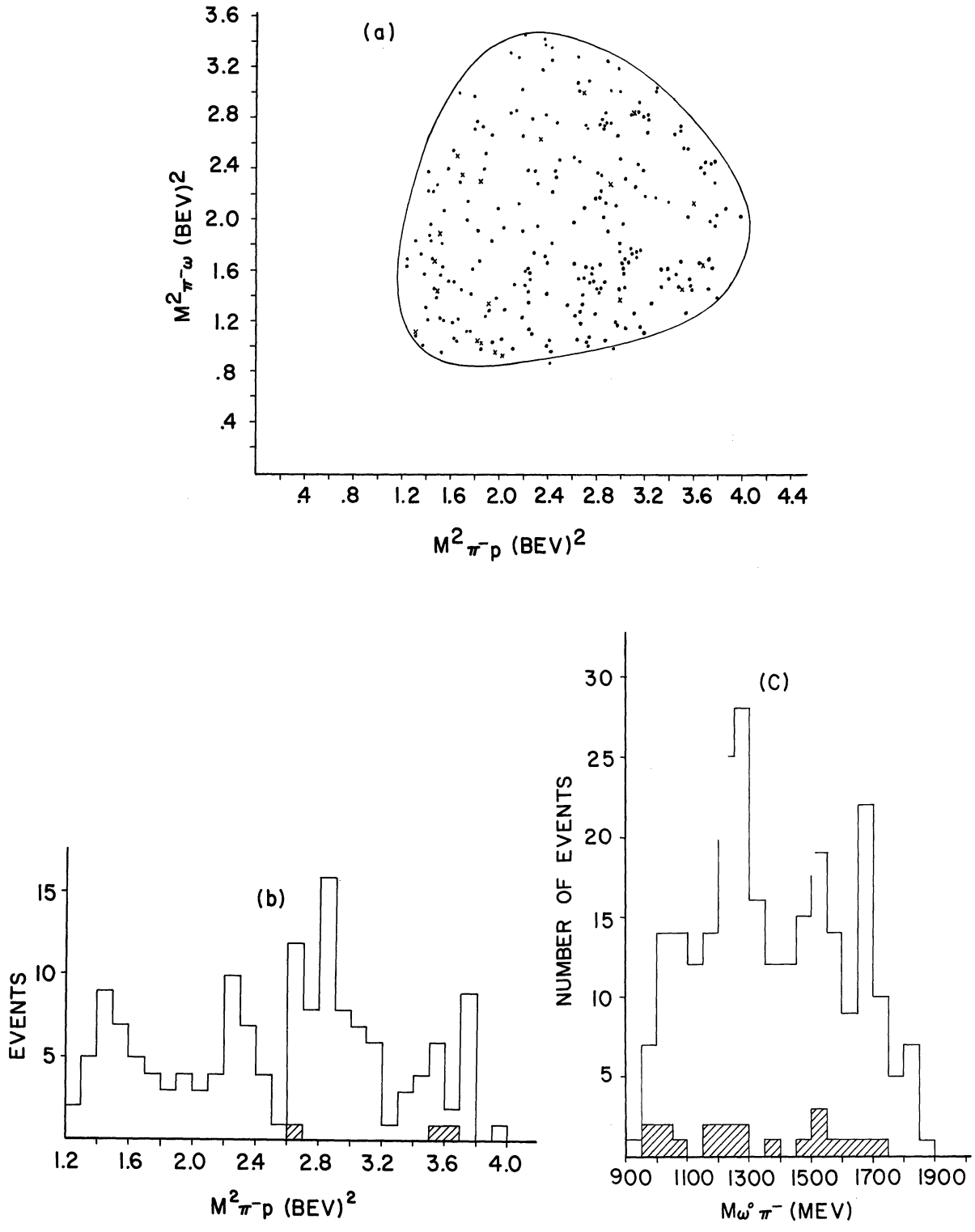

Figure 39. (a) Dalitz plot for the final state $(\omega^\circ,\pi^-.p)$. Those events ambiguous with the $(\pi^-,\pi^-,\pi^+,\pi^+,n)$ state are represented by (x). (b) $M^2_{\pi^-p}$ for the same final state with $\Delta^2_{\pi^-\to\omega^\circ} < 1.5(\text{BeV})^2$. (c) $M_{\pi^-\omega^\circ}$ for all events belonging to the (ω°,π^-,p) state. The events ambiguous with $(\pi^-,\pi^-,\pi^+,\pi^+,n)$ are added to both (b) and (c) and then represented separately by the shaded areas.

axis and $M^2_{\pi^-\omega^\circ}$ by the vertical axis. Here the evidence for resonance production does not seem to be at all favorable. However, both the (π^-,p) and the (π^-,ω°) systems do display very definite mass peaks when the two projections are plotted in the appropriate manner. When the horizontal projection is restricted to just those points for which $\Delta^2_{\pi^-\to\omega^\circ} < 1.5(\text{BeV})^2$ (see Figure 39(b)), the higher nucleon isobars appear. There is strong evidence for ω° production through the channels

$$\pi^- + p \to \omega^\circ + N^*_{3,-1}(1238) \qquad (5.6)$$
$$\to \pi^- + p,$$

$$\to \omega^\circ + N^*_{1,-1}(1512) \qquad (5.7)$$
$$\to \pi^- + p,$$

and

$$\to \omega^\circ + N^*_{1,-1}(1688) \qquad (5.8)$$
$$\to \pi^- + p.$$

In the (π^-,ω°) system there are also clear signs of a mass enhancement. This is seen in Figure 39(c) where $M_{\pi^-\omega^\circ}$ is plotted. The distribution peaks quite strongly in the region from 1200-1300 MeV and can be associated with the B enhancement seen in other experiments.[37,68,69]

The $(\pi^-,\pi^-,\pi^+,\pi^\circ)$ mass distribution has also been investigated for the events not satisfying $760 \leq M_{\pi^-\pi^+\pi^\circ} < 820$ MeV. It is found that there is no evidence whatsoever for a peak in the 1250 MeV region. Thus the B can be associated with the (π^-,ω°) state rather than a pure four-pion combination.

3.4 The B Peak

If it is assumed that the ω° is a $J^P = 1^-$ particle, then the ratio of true ω°'s to background should be much larger near the center of the Dalitz plot of Figure 38 than at the edge. For the inner boundary of this plot, assuming a $J^P = 1^-$ distribution, the calculated number of ω°'s inside and outside are approximately equal. In Figures 40(a) and 40(b) the $M_{\pi^-\pi^+\pi^\circ}$ distribution is shown for all events, with Figure 40(a) restricted to those inside and Figure 40(b) to those outside the inner boundary. By counting the number of events above and below phase space, the ω°-to-background ratio is found to be 65/30 and 70/85 for the inner and outer areas, respectively.

Now, as the data seems to suggest, if the B peak is a consequence of an (ω°,π^-) resonant state, then the larger ω°-to-background ratio for the center of the Dalitz plot should result in a more pronounced $M_{\pi^-\omega^\circ}$ peak for the events on the inside compared with those on the outside. This, however, is not the case. As was first observed by G. Goldhaber et al.,[69] the B peak is obtained almost entirely from the events whose points are situated in the outer area. This is seen very clearly in Figures 41(a) and 41(b) where $M_{\pi^-\omega^\circ}$ is plotted separately for the inside and outside events.

Another disturbing fact about the B enhancement is that every point in the peak $(1.4(\text{BeV})^2 \leq M^2_{\pi^-\omega^\circ} < 1.7(\text{BeV})^2)$ also falls in one of the N^* bands. This is shown in Figure 42 where $M^2_{\pi^-p}$ is plotted for just

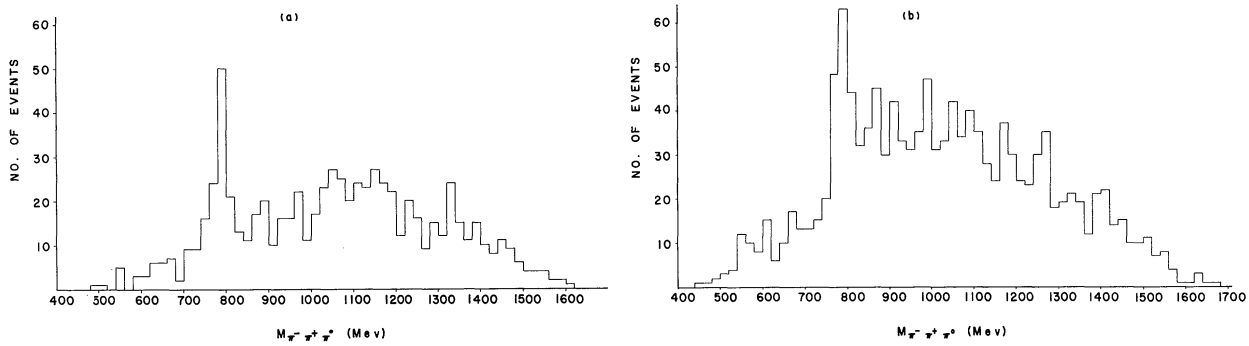

Figure 40. $M_{\pi^-\pi^+\pi^\circ}$ for (a) the inside and (b) the outside events.

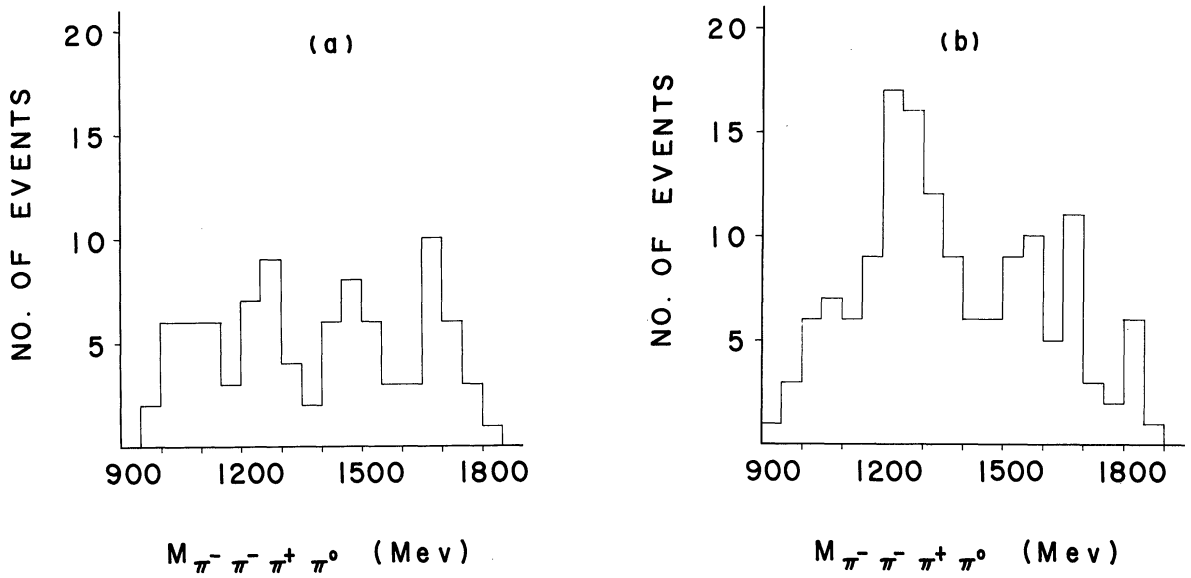

Figure 41. $M_{\pi^-\pi^-\pi^+\pi^\circ}$ for the events satisfying $760 \leq M_{\pi^-\pi^+\pi^\circ} < 820$ MeV. (a) the inside and (b) the outside events.

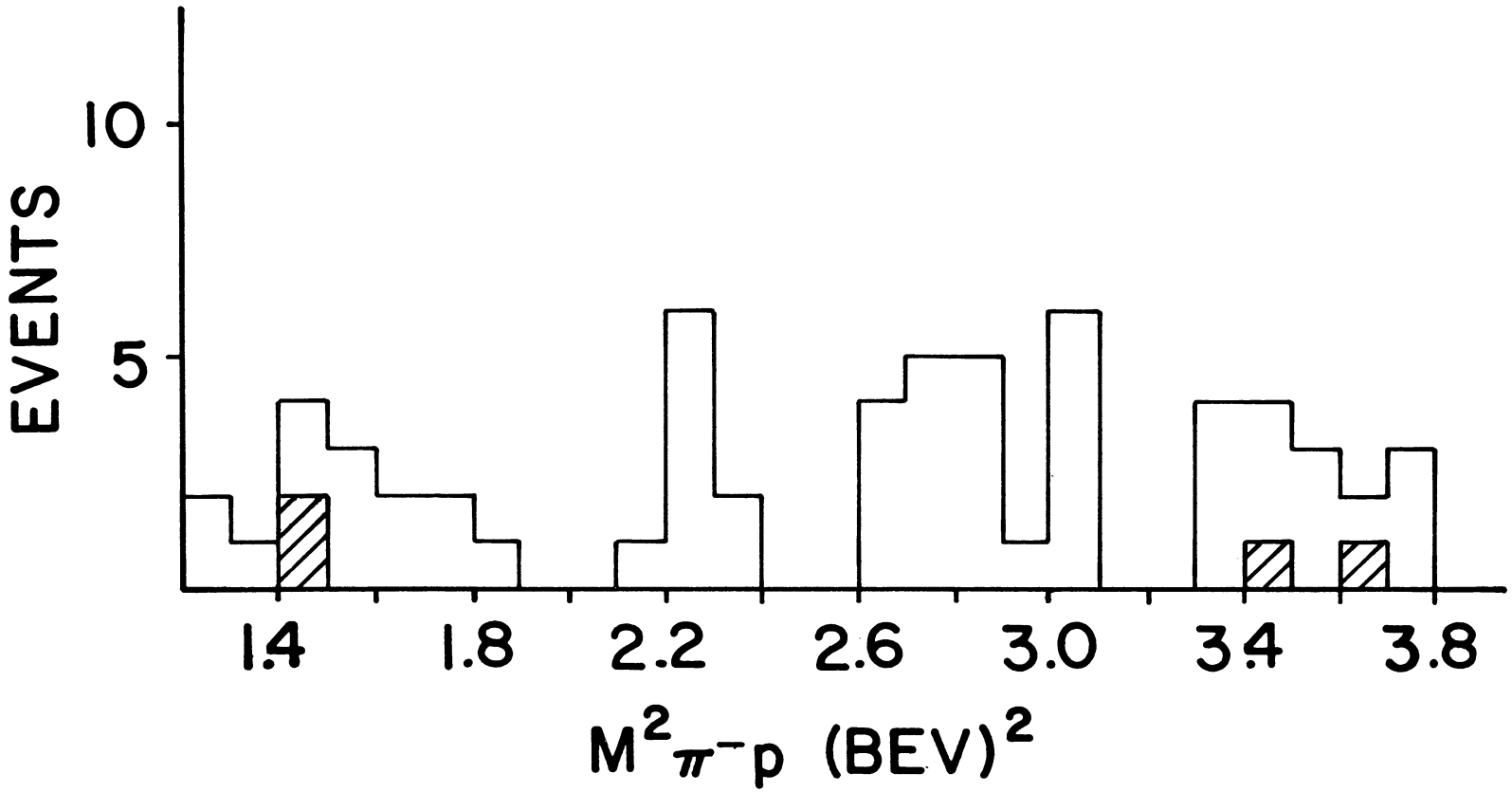

Figure 42. $M^2_{\pi^-p}$ for those events which satisfy $\pi^- + p \rightarrow B^- + p$. The events ambiguous with $(\pi^-,\pi^-,\pi^+,\pi^+,n)$ are added and then represented separately by the shaded area.

the B events. It is seen that the isobars all appear, while the mass intervals outside the peaks are completely empty.

At this point one must ask how the B peak is to be interpreted. Could it just be a four-pion resonance? This is ruled out because the B only appears when $M_{\pi^-\pi^+\pi^\circ}$ is restricted to the interval 760-820 MeV. This is definitely not the result of the phase-space mass distribution for three of four pions produced in the decay of a 1250 MeV particle. But if it is a (π^-,ω°) resonance, why do the B mesons seem to be associated with the sample whose relative ω° enrichment is smaller? Maybe there is another $\vec{T} = 0$ three-pion resonance with a mass close to that of the ω° but with a different spin-parity assignment. The same analysis has been applied to the region $820 \leq M_{\pi^-\pi^+\pi^\circ} < 900$ MeV, and there is no evidence of a B peak for either the inner or outer areas. Therefore, if there is such a particle, its upper mass limit must be approximately 820 MeV. Also, it is very improbable that its lower mass limit could be much less than 760 MeV because of the small number of events with $M_{\pi^-\pi^+\pi^\circ} < 760$ MeV (see Figure 37(a)). Thus, if there is a $\vec{T} = 0$ three-pion resonance with $J^P \neq 1^-$, its width must be such that its mass limits are either inside or equal to 760-820 MeV.

And finally, is it possible that the B peak is somehow related to the isobars? Maybe, with increased statistics, the B peak will be explained in terms of reactions (5.6), (5.7), and (5.8). It is remembered that this same possibility also exists for the A mesons.

4. THE ρ^- PEAK

4.1 Introduction

The investigation of the ρ^- will be restricted to the reactions

$$\pi^- + p \rightarrow \rho^- + N^*_{3,3}(1238) + \pi^- \qquad (5.10)$$

and

$$\rightarrow \rho^- + N^*_{3,-1}(1238) + \pi^+, \qquad (5.11)$$

where the ρ^- and N^* regions are 660-820 MeV and 1140-1340 MeV, respectively. It will be seen that the entire enhancement in the ρ^- region can be associated with these two channels. Since there are possible biases in the data due to the 121 ambiguous events and ω° production, the effects of these will be shown separately whenever necessary. However, it is clear from Figure 36(a) that neither can influence the results greatly because of the small number of events involved.

4.2 (N^*,π) Decay Modes of the Higher Nucleon Isobars

It has already been noted that a significant number of the ρ^- and $N^*_{3,3}(1238)$ states seem to be produced concurrently. This is quite evident when the M_{π^+p} spectrum (Figure 43) for the reaction

$$\pi^- + p \rightarrow \rho^- + \pi^- + \pi^+ + p \qquad (5.12)$$

and $M_{\pi^-\pi^\circ}$ (Figure 44) for the reaction

$$\pi^- + p \rightarrow \pi^- + \pi^- + \pi^\circ + N^*_{3,3}(1238) \qquad (5.13)$$

are examined. These plots show a definite preference for the simultaneous production of the two resonances. In fact, upon examination of the $M_{\pi^-\pi^\circ}$ and M_{π^+p} distributions for reaction (5.4) with all events

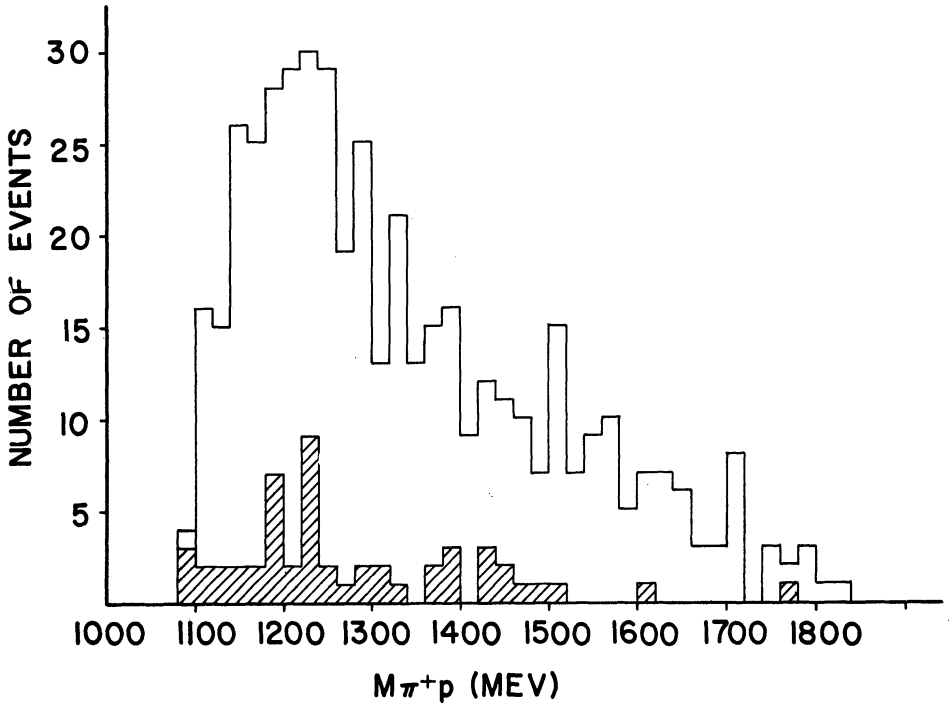

Figure 43. M_{π^+p} for the reaction $\pi^- + p \rightarrow \rho^- + \pi^- + \pi^+ + p$. The ambiguous events are added and then represented separately by the shaded areas.

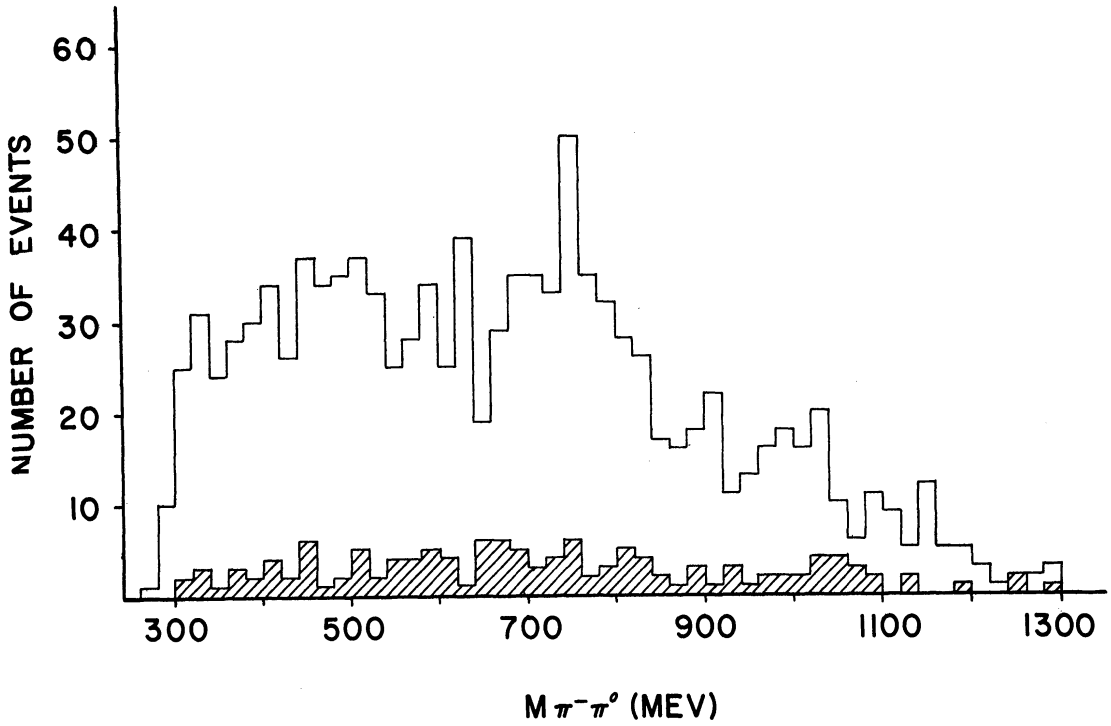

Figure 44. $M_{\pi^-\pi^\circ}$ for the reaction $\pi^- + p \rightarrow \pi^- + \pi^- + \pi^\circ + N^*_{3,3}(1238)$. The ambiguous events are added and then represented separately by the shaded areas.

from (5.10) subtracted (not shown), it is seen that both the ρ^- and the $N^*_{3,3}(1238)$ peaks are no longer prominent. Furthermore, the slight remaining enhancement in the ρ^- region can be associated with reaction (5.11). This is verified by examining the $M_{\pi^-\pi^\circ}$ spectrum (not shown) for the reaction

$$\pi^- + p \rightarrow \pi^- + \pi^\circ + \pi^+ + N^*_{3,-1}(1238). \qquad (5.14)$$

From this point on, in light of the evidence just presented, the investigation of the ρ^- will be restricted to reactions (5.10) and (5.11). The $M_{\pi^-N^*_{3,3}}$ and $M_{\pi^+N^*_{3,-1}}$ distributions for these reactions are shown in Figures 45 and 46. In order to determine the effect of the ω° overlap on the data, the two mass distributions are plotted in three different ways: (1) all events, (2) all ω° events subtracted, (3) an ω° subtraction based on a Monte Carlo calculation. The Monte Carlo subtraction is accomplished by assuming the final state (ω°,π^-,p) and then counting the number of fake events of the type (π,N^*,ρ^-) that are produced by the ω° decay. For the 135 ω°'s above phase space it is estimated that fifteen of the type (5.10) or (5.11) are formed. This number is used to arrive at the plots in Figures 45(c) and 46(c). In the $M_{\pi^-N^*_{3,3}}$ histograms there are three obvious deviations from phase space. These are all located close to known nucleon-resonance mass values at 1512, 1688, and 1920 MeV. In the $M_{\pi^+N^*_{3,-1}}$ plots the peaking again appears at 1512 MeV but there is nothing in the 1688 MeV region. There is also an enhancement in the 1920 MeV region, but its central value is 50 MeV on the low side.

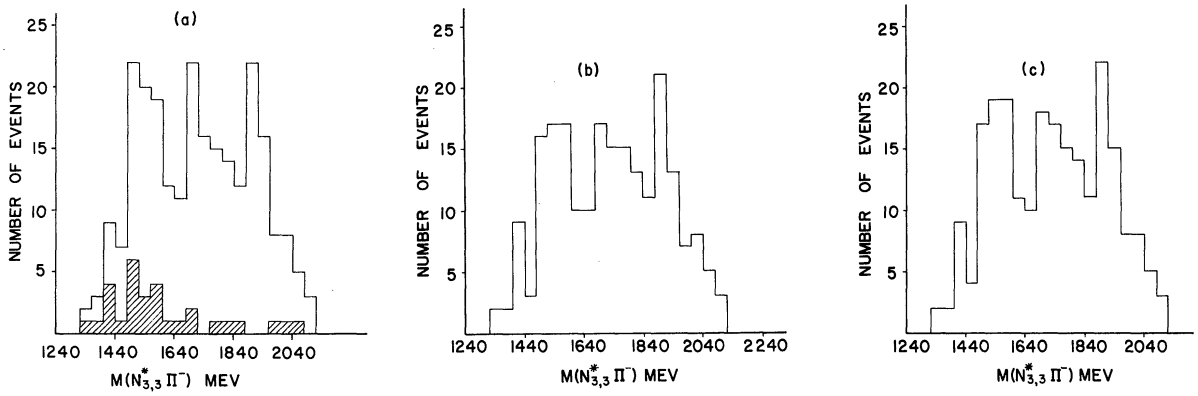

Figure 45. $M_{\pi^-N^*_{3,3}}$ for the reaction $\pi^- + p \rightarrow \rho^- + N^*_{3,3}(1238) + \pi^-$. (a) all events; (b) all ω° events subtracted; and (c) an ω° subtraction based on a Monte Carlo calculation. The shaded area in (a) represents the ambiguous events.

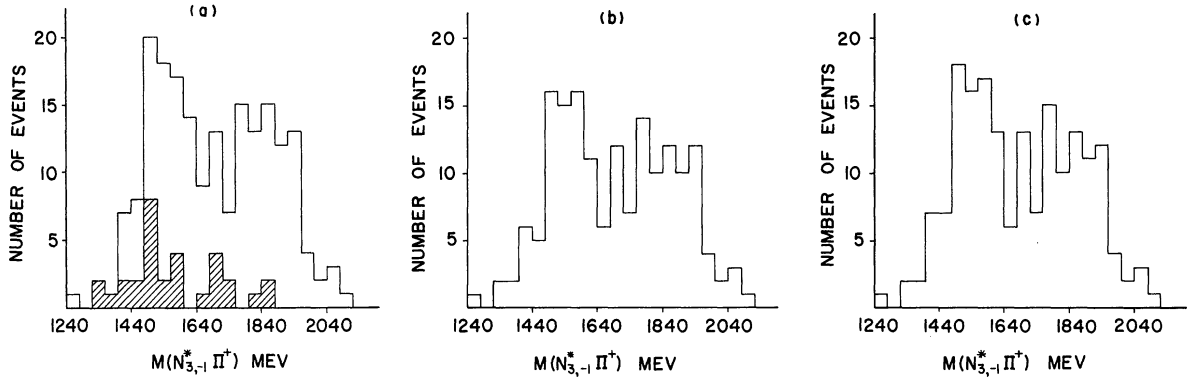

Figure 46. $M_{\pi^+N^*_{3,-1}}$ for the reaction $\pi^- + p \rightarrow \rho^- + N^*_{3,-1}(1238) + \pi^+$. (a) all events; (b) all ω° events subtracted; (c) an ω° subtraction based on a Monte Carlo calculation. The shaded area in (a) represents the ambiguous events.

If one now hypothesizes the processes

$$\begin{aligned} \pi^- + p &\rightarrow \rho^- + N^*_{1,1}(1512) \\ &\rightarrow \pi + N^*(1238) \\ &\rightarrow \pi + p, \end{aligned} \qquad (5.15)$$

$$\begin{aligned} \pi^- + p &\rightarrow \rho^- + N^*_{1,1}(1688) \\ &\rightarrow \pi + N^*(1238) \\ &\rightarrow \pi + p, \end{aligned} \qquad (5.16)$$

and

$$\begin{aligned} \pi^- + p &\rightarrow \rho^- + N^*_{3,1}(1920) \\ &\rightarrow \pi + N^*(1238) \\ &\rightarrow \pi + p, \end{aligned} \qquad (5.17)$$

then isotopic spin conservation demands that (see Appendix B)

$$\frac{\sigma(N^*_{1,1} \rightarrow \pi^- + N^*_{3,3} \rightarrow \pi^- + \pi^+ + p)}{\sigma(N^*_{1,1} \rightarrow \pi^+ + N^*_{3,-1} \rightarrow \pi^+ + \pi^- + p)} = 9/1 \qquad V.1$$

and

$$\frac{\sigma(N^*_{3,1} \rightarrow \pi^- + N^*_{3,3} \rightarrow \pi^- + \pi^+ + p)}{\sigma(N^*_{3,1} \rightarrow \pi^+ + N^*_{3,-1} \rightarrow \pi^+ + \pi^- + p)} = 9/4. \qquad V.2$$

The data presented here is consistent with these ratios as will now be shown.

At 1688 MeV there is a peak in the $M_{\pi^-N^*_{3,3}}$ plot which does not appear in the $M_{\pi^+N^*_{3,-1}}$ histogram. Also, a Dalitz plot (Figure 47(a)) of $M^2_{\pi^-p}$ versus $M^2_{\pi^+p}$ for all (π^-,π^+,p) masses of reaction (5.12) in the interval 1600-1760 MeV shows that the $N^*_{3,3}(1238)$ is definitely favored over the $N^*_{3,-1}(1238)$. There are 44 points in the $N^*_{3,3}(1238)$ region

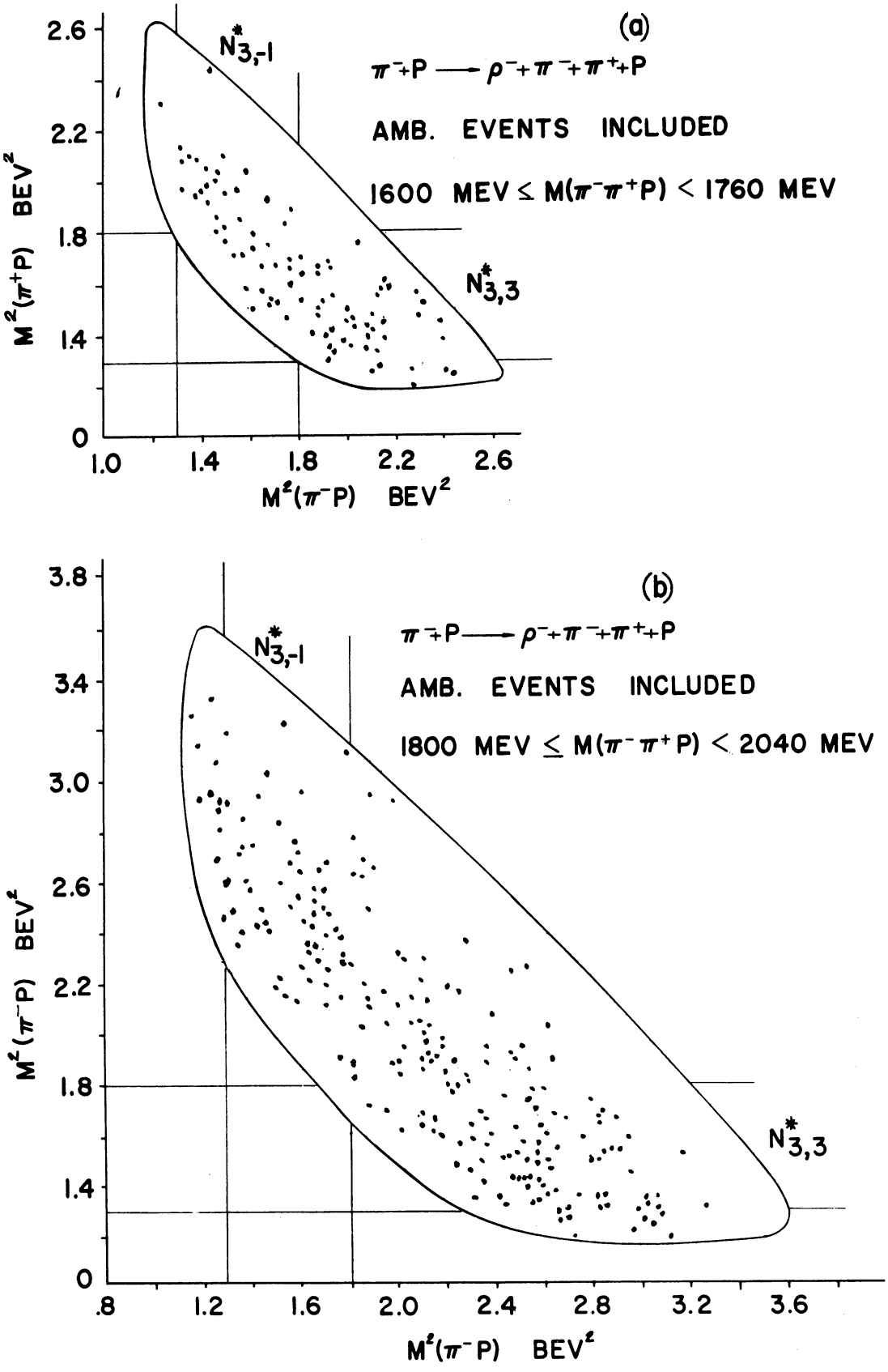

Figure 47. Dalitz plots for (a) 1600 ≤ $M_{\pi^-\pi^+p}$ < 1760 MeV, and (b) 1800 ≤ $M_{\pi^-\pi^+p}$ < 2040 MeV. These are just for the reaction $\pi^- + p \rightarrow \rho^- + \pi^- + \pi^+ + p$ and also include the ambiguous events.

with no $N^*_{3,-1}(1238)$, 24 points in the $N^*_{3,-1}(1238)$ region with no $N^*_{3,3}(1238)$, and 19 points in the overlap between the two isobars. Since the difference between the number of points in the two bands is approximately equal to the number of events above phase space in the $M_{\pi^-}N^*_{3,3}$ distribution, the data agrees very well with the 9/1 ratio.

At 1512 MeV the branching ratio cannot be checked because the available kinetic energy for the decay products is too small. When the Dalitz plot limits are drawn, it is found that most of the area is in the overlap region of the two (π,p) resonances. This is also responsible for the 1512 MeV peak in the $M_{\pi^+}N^*_{3,-1}$ histogram. If this enhancement were real—instead it is a reflection of the $(\pi^-,N^*_{3,3})$ decay mode—the ratio given by V.1 would not be satisfied.

The Dalitz plot for $1800 \leq M_{\pi^-\pi^+p} < 2040$ MeV is shown in Figure 47(b). Here there are two bands, one corresponding to the $N^*_{3,3}(1238)$ and one for the $N^*_{3,-1}(1238)$. The ratio of points in these two intervals is very close to 3/2. Considering the large amount of background, this is in good agreement with the predicted value of 9/4.

4.3 The Production Mechanism for the ρ^-

It has just been demonstrated that almost the entire ρ^- peak can be associated with reaction (5.10), and furthermore, a significant number of these events can be placed with (5.15), (5.16), and (5.17). These results lead one to suspect that the ρ^- may be produced by means

of a π°- or ω°-exchange mechanism (see Figure 48).

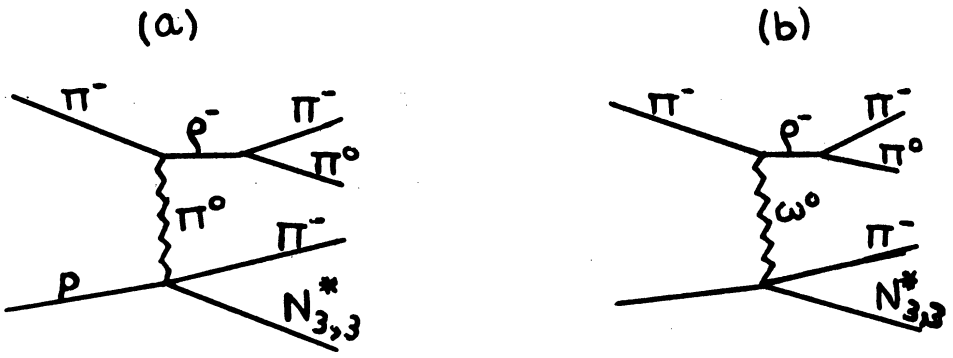

Figure 48. Possible meson-exchange diagrams for ρ^- production in reaction (5.10).

It will now be shown that neither diagram can be singled out as the primary contributor to ρ^- production in (5.10). This is based on the following results:

a) The Trieman-Yang distribution (not shown) is not favorable for pure pion exchange, as the χ^2 test for isotropy yields a probability of less than 3%. This nonisotropy could be due to absorption, however, so this test alone does not rule out the π° possibility.

b) It is shown in Appendix C that if one-pion exchange is assumed, the cross section for

$$\begin{aligned} \pi^- + p &\rightarrow \rho^\circ + N^* \\ &\rightarrow \pi^+ + N^*_{3,-3} \\ &\rightarrow \pi^- + n \end{aligned} \qquad (5.18)$$

should be twice that of reactions (5.15) and (5.16), and for the $\vec{T} = 3/2$ isobar at 1920 MeV, the cross section in the neutron case should be one-half as large as that of (5.17).

In the reaction

$$\pi^- + p \rightarrow \pi^- + \pi^- + \pi^+ + \pi^+ + n \qquad (5.19)$$

a strong $N^*_{3,-3}(1238)$ peak is found in the (π^-,n) state, but there is no evidence at all for ρ° production. In spite of the fact that the ρ° does not appear, the $(\pi^+,N^*_{3,-3}(1238))$ mass is plotted in Figure 49 for all events that satisfy

$$\pi^- + p \rightarrow \text{"}\rho^\circ\text{"} + \pi^+ + N^*_{3,-3}. \qquad (5.20)$$

The ρ° region is chosen to be 660-820 MeV, and the notation "ρ°" is used in (5.20) to emphasize that there is no evidence for the particle. The histogram does show small peaks in the regions of the heavier isobars, but they are definitely not large enough to agree with the ratios predicted by pion exchange. One might say that there is some contribution from the diagram of Figure 48(a), but it definitely does not dominate the production process.

c) The scattering angle distribution for the π^- in the ρ^- center of mass is shown in Figure 50. If ω° exchange with no absorption is assumed, this plot should behave as $\sin^2\theta$, the possibility of which is nil. If a small amount of $\vec{T} = 2$ amplitude is assumed, this actually agrees quite well with π° exchange. However, absorptive effects are known to change angular distributions drastically, so ω° exchange cannot be excluded by this one result; only ω° exchange with no absorption is eliminated.

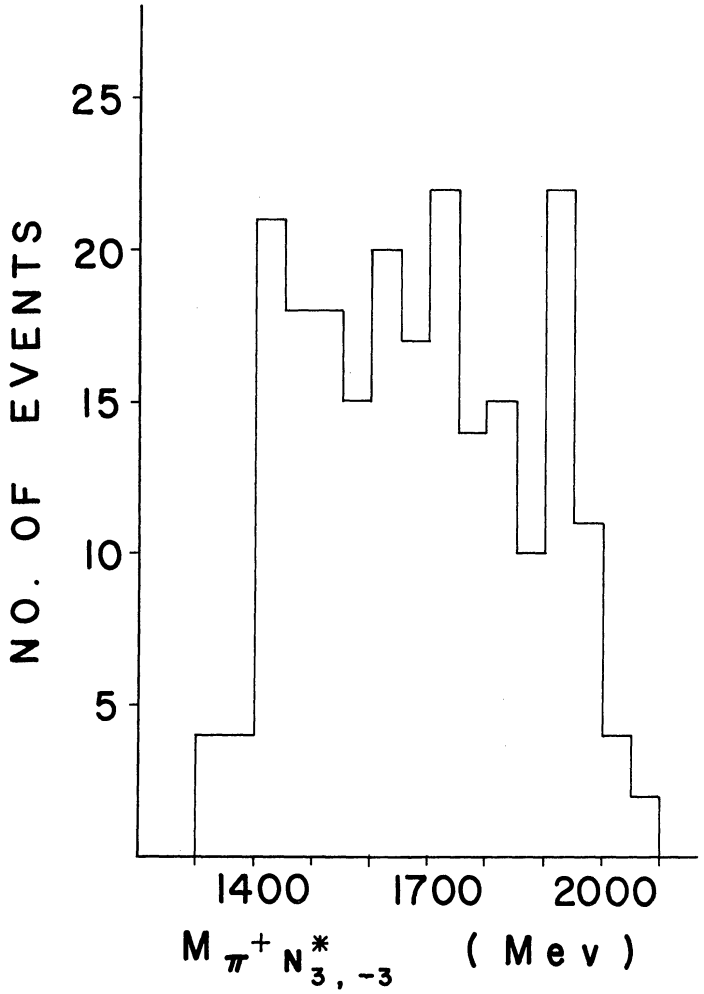

Figure 49. $M_{\pi^+ N^*_{3,-3}}$ for the reaction $\pi^- + p \rightarrow$ "ρ^0" $+ \pi^+ + N^*_{3,-3}(1238)$.

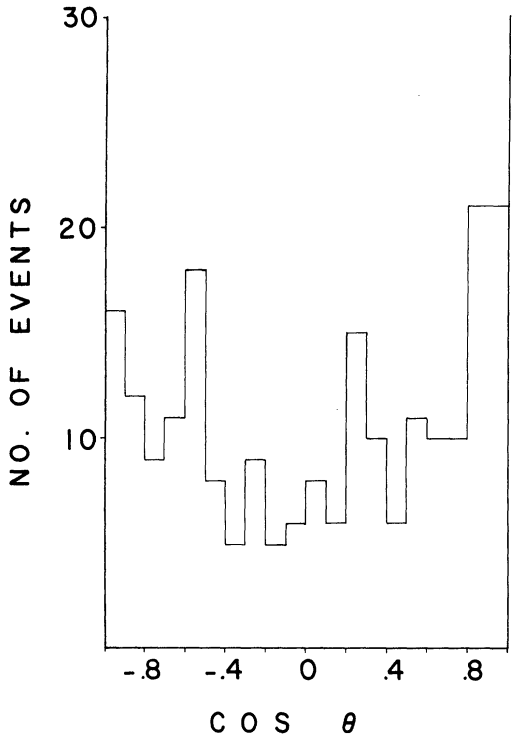

Figure 50. The scattering angle of the π^- in the ρ^- center of mass for the events satisfying $\pi^- + p \rightarrow \rho^- + \pi^- + N^*_{3,3}(1238)$.

d) If the ω° diagram is assumed, then reaction (5.20) is not allowed via this mechanism. This is so because the ω° is an isotopic singlet and does not exist in the charged state. However, neither can (5.17) occur through ω° exchange, as this would violate isotopic spin conservation at the lower vertex. So, at most, only the $N^*_{1,1}(1512)$ and $N^*_{1,1}(1688)$ peaks plus the $\vec{T} = 1/2$ background in (5.10) can be explained by the ω° diagram. But even this is unlikely, as one would not expect (5.10) to proceed by the ω°-exchange process except for that small part satisfying (5.17).

Thus it seems quite certain that neither π° nor ω° exchange completely dominate reaction (5.10). The considerations in (b) make the π° possibility very remote, and the ω° is definitely ruled out for the $\vec{T} = 3/2$ channel by isotopic spin conversation.

5. φ MESON PRODUCTION

In addition to the ω° there is also another vector meson, the φ, whose quantum numbers are $J^{PG} = 1^{--}$. Except for its mass (M_φ = 1020 MeV), this particle is identical to the ω°, and one might expect its principal decay mode to be $\varphi \to \pi^+ + \pi^- + \pi^\circ$. Experimentally, however, the 3π rate of the φ is much less than that for $\varphi \to K + \bar{K}$,[70,71] implying that the physical coupling constant $G_{\rho\varphi\pi}$ is small compared to $G_{\rho\omega^\circ\pi}$. As suggested by Glashow,[72] this can also lead to a small production rate for φ's as compared to ω°'s in pion-proton interactions.

The ratio

$$R = \frac{\sigma(\pi^- + p \rightarrow \pi^- + p + \varphi)}{\sigma(\pi^- + p \rightarrow \pi^- + p + \omega^\circ)}$$

has been determined from the data of this experiment, and it is found that $R \leq .012$, indicating that ω°'s are, indeed, produced much more abundantly than φ's in (π,p) collisions. A more thorough discussion of this can be found in Reference 27.

6. THE PRODUCTION ANGLES

The production angles for the π^-, π^+, p, and π° are shown in Figures 51(a-d). The pion and proton distributions are peaked forward and backward, respectively, with the negative pion and proton showing the more pronounced asymmetry. Most of this asymmetry can be associated with the ω° and ρ^- reactions, although the distributions are still peaked slightly when only events outside these peaks are considered.

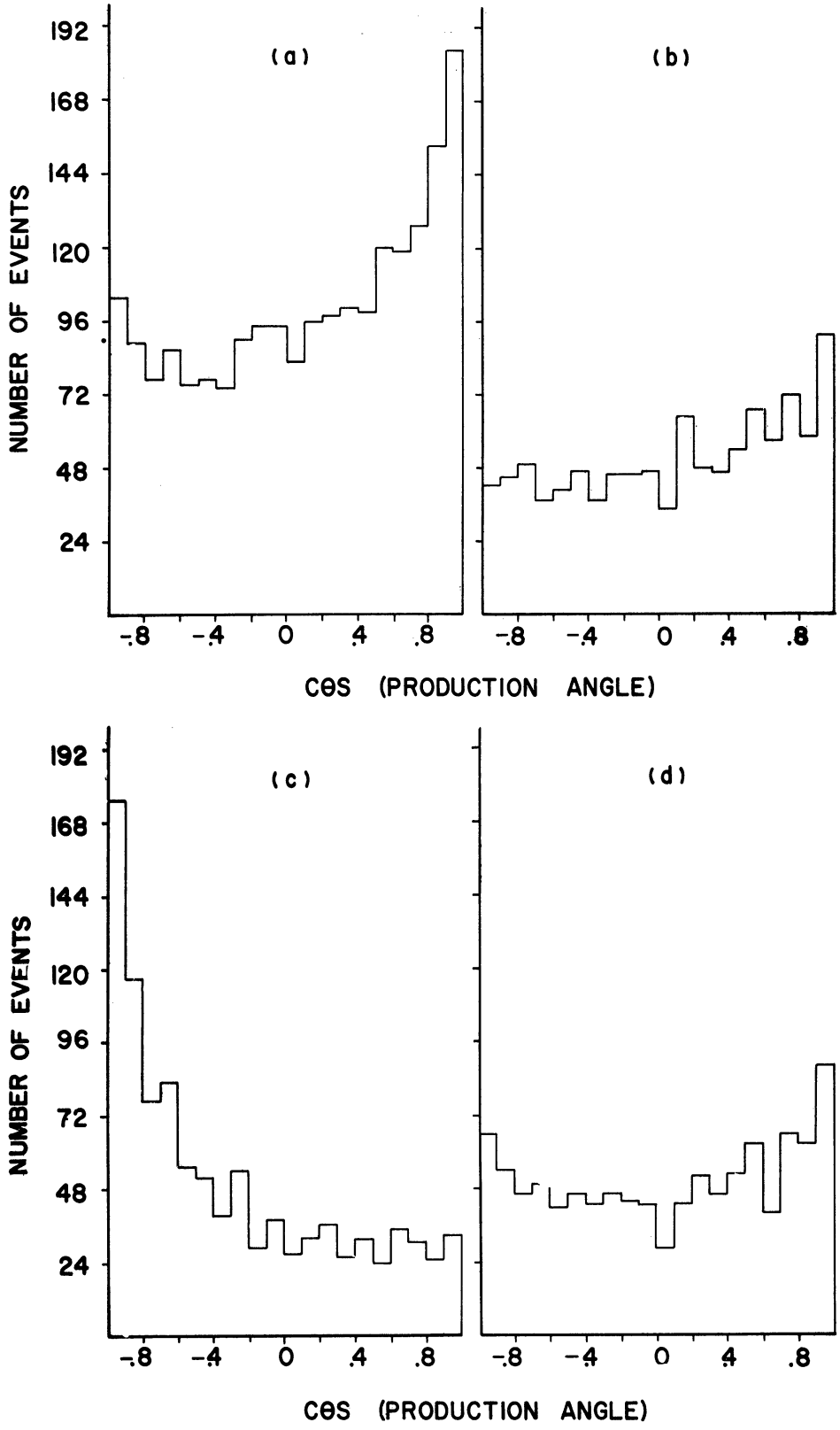

Figure 51. The particle production angles for the reaction $\pi^- + p \rightarrow \pi^- + \pi^- + \pi^+ + p + \pi^\circ$. (a) the π^-. (b) the π^+. (c) the p, and (d) the π°.

CHAPTER VI

THE REACTION $\pi^- + p \rightarrow \pi^- + \pi^- + \pi^+ + \pi^+ + n$

In this reaction there is nothing of interest to report. All possible mass combinations have been studied with various subtractions and momentum transfer cutoffs imposed on the data. The only resonant state to appear is the $N^*_{3,-3}(1238)$ in the reaction

$$\pi^- + p \rightarrow \pi^- + \pi^+ + \pi^+ + N^*_{3,-3}(1238) \qquad (6.1)$$
$$\rightarrow \pi^- + n$$

At first sight, one might consider (6.1) as an ideal reaction to search for three-pion resonances such as the A mesons; however, none are found. This may be due to the fact that the production of such a resonance requires the exchange of a doubly charged particle in any simple meson-exchange process.

The production angles for the particles have also been investigated. With the exception of the neutron whose distribution is peaked in the backward direction, it is found that the particles are produced isotropically.

CHAPTER VII

RESONANCE CROSS SECTIONS

The cross sections for all resonant states discussed in this report are summarized in Table VII. These were obtained by simply counting the number of events above phase space in the given figure. There are no corrections made for other decay modes of the resonances, and these values, therefore, just represent a specific particle combination. For example, the cross section for the reaction

$$\pi^- + p \rightarrow \rho^\circ + N^*_{3,-1}(1238) \qquad (7.1)$$

does not include the contribution from the (π°,n) decay of the $N^*_{3,-1}(1238)$; specifically, it is just the cross section for

$$\pi^- + p \rightarrow \rho^\circ + N^*_{3,-1}(1238)$$
$$\rightarrow \pi^- + p. \qquad (7.2)$$

TABLE VII

THE CROSS SECTIONS FOR THE RESONANCES FOUND IN THIS EXPERIMENT
(The column labelled "Mass Interval" represents the mass width assumed for the given particle combination)

CHANNEL	Mass Interval	Figure	σ(mb.)
$\pi^- + p \rightarrow \rho^\circ + \pi^- + p$	$660 \leq M_{\rho^\circ} < 820$	15(c)	.43
$\rightarrow \rho^\circ + N^*(1238)$	$1140 \leq M_{N^*} < 1340$	17(c)	.069
$\rightarrow A_1 + p$	$1000 \leq M_{A_1} < 1150$	24(c)	.050
$\rightarrow A_2 + p$	$1200 \leq M_{A_2} < 1350$	24(c)	.056
$\rightarrow N^*(1238) + \pi^- + \pi^-$	$1130 \leq M_{N^*} < 1330$	15(a)	.51
$\rightarrow \omega^\circ + \pi^- + p$	$760 \leq M_{\omega^\circ} < 820$	37(a)	.28
$\rightarrow \omega^\circ + N^*(1238)$	$1.3 \leq M^2_{N^*} < 1.8$	39(b)	.031
$\rightarrow \omega^\circ + N^*(1512)$	$2.1 \leq M^2_{N^*} < 2.5$	39(b)	.019
$\rightarrow \omega^\circ + N^*(1688)$	$2.6 \leq M^2_{N^*} < 3.2$	39(b)	.069
$\rightarrow B^- + p$	$1200 \leq M_{B^-} < 1300$	39(c)	.056
$\rightarrow \rho^- + \pi^+ + N^*(1238)$	$660 \leq M_{\rho^-} < 820$ $1140 \leq M_{N^*} < 1340$	43	.23
$\rightarrow \rho^- + N^*(1512)$	$1480 \leq M_{N^*} < 1600$	45(a)	.061
$\rightarrow \rho^- + N^*(1688)$	$1680 \leq M_{N^*} < 1840$	45(a)	.040
$\rightarrow \rho^- + N^*(1920)$	$1880 \leq M_{N^*} < 1960$	45(a)	.033
$\rightarrow N^*(1238) + \pi^- + \pi^+ + \pi^+$	$1140 \leq M_{N^*} < 1340$	Not Shown	.50

APPENDIX A

LORENTZ INVARIANT PHASE SPACE AND THE DALITZ PLOT

Consider an n-body final state in the center-of-momentum frame (CM frame) and let the following variables be defined:

m_i, q_i, $\vec{P}_i$, E_i the rest mass, four-momentum, vector momentum, and the energy of the i'th particle.

Q_T, $\vec{P}_T$, E_T the four-momentum, vector momentum, and the energy of the system. $\vec{P}_T$ vanishes in the reference frame considered.

M_{ij} the effective mass of particles i and j.

$R_m(\vec{P}_T,E_T)$ the number of states (integrated density of states) for a system with total momentum $\vec{P}_T$ and total energy E_T.

Ignoring multiplicative constants, $R_n(\vec{P}_T,E_T)$ is defined as follows:

$$R_n(\vec{P}_T,E_T) \alpha \int \frac{d^3\vec{P}_1}{2E_1} \cdots \frac{d^3\vec{P}_n}{2E_n} \delta^4(Q_T - \sum_{i=1}^{n} q_i). \qquad (A.1)$$

It is easy to show that A.1 is equivalent to

$$R_n(0,E_T) \alpha \int (\prod_{i=1}^{n} d^4q_i \delta(q_i^2 - M_i^2)) \delta(E_T - \sum_{i=1}^{n} E_i) \delta^3(\sum_{i=1}^{n} \vec{P}_i), \qquad (A.2)$$

where the condition $\vec{P}_T = 0$ in the CM reference frame is inserted in the equation.

Rewriting Formula A.2 in the form

$$R_n(0,E) \alpha \int \frac{d^3\vec{P}_n}{2E_n} \left(\int \prod_{i=1}^{n-1} d^4q_i \delta(q_i^2 - M_i^2) \delta^4(\sum_{i=1}^{n-1} q_i + q_n - Q) \right) \qquad (A.3)$$

and using $\vec{P}_T = 0$, $R_n(0,E)$ can be written

$$R_n(0,E) \propto \int \frac{d^3\vec{P}_n}{2E_n} R_{n-1}(-\vec{P}_n, E-E_n). \tag{A.4}$$

Since R_n is constructed to be a Lorentz invariant, it can be expressed in any reference frame. Upon making a transformation to the $\vec{P}_n = 0$ system and in addition, using the relationship

$$(E-E_n)^2 - (-\vec{P}_n)^2 = \epsilon^2, \tag{A.5}$$

then

$$R_n(0,E) \propto \int \frac{d^3\vec{P}_n}{2E_n} R_{n-1}(0,\epsilon), \tag{A.6}$$

a recurrence relation which allows one to calculate the n-dimensional phase-space integral from the (n-1)-dimensional value. Since R_2 can be evaluated quite easily, it is possible to find R_n for any n.

$R_2(0,\epsilon)$ is evaluated as follows:

$$R_2(0,\epsilon) \propto \int \frac{d^3\vec{P}_1}{2E_1} \frac{d^3\vec{P}_2}{2E_2} \delta(E_1+E_2-\epsilon)\delta(\vec{P}_1+\vec{P}_2) \tag{A.7}$$

$$\propto \int \frac{d^3\vec{P}_1}{4E_1E_2} \delta(E_1+E_2-\epsilon), \tag{A.8}$$

where in A.8 it is assumed $|\vec{P}_1| = |\vec{P}_2|$. Now, using

$$\begin{aligned} E_1(P_1) &= \sqrt{P_1^2 + M_1^2} \\ E_2(P_1) &= \epsilon - \sqrt{P_1^2 + M_1^2}, \end{aligned} \tag{A.9}$$

R_2 can be written

$$R_2(0,\epsilon) \propto \int \frac{P_1^2 dP_1}{E_1(P_1)E_2(P_1)} \delta(\sqrt{P_1^2+M_1^2} + \sqrt{P_2^2+M_2^2} - \epsilon). \tag{A.10}$$

This is integrated quite easily and finally,

$$R_2(0,\epsilon) \alpha \frac{P_1}{\epsilon} , \qquad (A.11)$$

a relationship which allows any R_n to be computed by repeated use of Formulas A.5 and A.6.

Now let the effective-mass distribution of m out of n particles be considered. Assume an ordering so that the m particles are numbered 1, 2 ... m, and the other (n - m) are numbered m + 1 ... n. Denote the four-momenta of the two groups by Q_m and Q_{n-m} and their center-of-momentum energies (or effective masses) by M_m and M_{n-m}. Also make the notational change

$$R_n(\vec{P},E) \rightarrow R_n(Q,m_1 \ldots m_n),$$

where Q is the total four-momentum and $m_1 \ldots m_n$ represent the masses of a system of n particles.

The phase space distribution of M_m is given by

$$P(M_m)dM_m^2 = \frac{R_{n-m+1}(Q_T, M_m, m_{m+1} \ldots m_n) R_m(Q_m, m_1 \ldots m_m)}{R_n(Q_T, m_1 \ldots m_n)} dM_m^2 . \qquad (A.12)$$

The derivation of this can be found in RELATIVISTIC KINEMATICS[73] by R. Hagedorn. He starts with $R_n(Q_T; m_1 \ldots m_n)$ in the form of A.2, makes the substitution

$$\delta^4\left(\sum_{j=1}^{n} q_j - Q_T\right) = \int d^4Q_m \delta^4(Q_T - Q_m - \sum_{j=m+1}^{n} q_j) \delta^4(Q_m - \sum_{j=1}^{m} q_j), \qquad (A.13)$$

multiplies the resulting expression for R_n by

$$1 = \int \delta(Q_m^2 - M_m^2) dM_m^2, \qquad (A.14)$$

and is then able to obtain (A.12) quite easily.

The computation of the phase-space distributions for four or more particles was handled in this experiment by the computer program LIMS.[74] This program evaluates the necessary R_n's and then by using relationships similar to A.12, it calculates the mass distributions for the various particle combinations. Since R_n cannot be put in functional form for $n \geq 3$, LIMS has to set up numerical tables to represent the R_n's, which, of course, requires that the integrals of these functions be done numerically.

For the three-body final state the phase-space computations were handled by the program DALPS.[75] In addition to the mass distributions, this program also calculates the kinematical limits for the Dalitz plot, a scattergram of M_{12}^2 vs. M_{23}^2. As will now be shown, this plot should be uniformly populated for a phase-space distribution.

For a three-body final state with center-of-momentum energy M,

$$R_3(M;m_1,m_2,m_3) \propto \int \frac{d^3\vec{P}_1 d^3\vec{P}_2 d^3\vec{P}_3}{E_1 E_2 E_3} \delta(\vec{P}_1+\vec{P}_2+\vec{P}_3)\delta(M-E_1-E_2-E_3) \qquad (A.15)$$

By performing the integration over P_3, the result

$$R_3 \propto \int \frac{d^3\vec{P}_1 d^3\vec{P}_2}{E_1 E_2 E_3} \delta(M-E_1-E_2-E_3) \qquad (A.16)$$

is obtained, where

$$\vec{P}_3^{\,2} = \vec{P}_1^{\,2} + \vec{P}_2^{\,2} + 2\vec{P}_1 \cdot \vec{P}_2. \qquad (A.17)$$

If the integration over the direction of $\vec{P}_2$ is carried out first and then followed by the integration over the direction of $\vec{P}_1$, then

$$d^3\vec{P}_1 = 4\,P_1^2 dP_1$$

and (A.18)

$$d^3\vec{P}_2 = 2\,P_2^2 dP_2 d(\cos\theta),$$

where

$$\cos\theta = \frac{\vec{P}_1 \cdot \vec{P}_2}{|\vec{P}_1||\vec{P}_2|}. \tag{A.19}$$

Thus,

$$R_3 \alpha \int \frac{P_1^2 dP_1 P_2^2 dP_2 d(\cos\theta)}{E_1 E_2 E_3}\ \delta(M-E_1-E_2-E_3). \tag{A.20}$$

Using the energy-momentum formulas

$$E_1^2 = P_1^2 + m_1^2 \tag{A.21}$$

$$E_2^2 = P_2^2 + m_2^2$$

$$E_3^2 = P_3^2 + m_3^2 = P_1^2+P_2^2+2P_1P_2\cos\theta+m_3^2,$$

it is readily seen that

$$dP_1 dP_2 d(\cos\theta) = \frac{E_1E_2E_3}{P_1^2P_2^2}\, dE_1 dE_2 dE_3, \tag{A.22}$$

and therefore,

$$R_3 \alpha \int dE_1 dE_2 dE_3 \delta(M-E_1-E_2-E_3) \tag{A.23}$$

$$\alpha \int dE_1 dE_2,$$

where

$$E_3 = M-E_1-E_2. \tag{A.24}$$

By using

$$M_{12}^2 = (M-m_3)^2 - 2M(m_3+E_3)$$

and (A.25)

$$M_{23}^2 = (M-m_1)^2 - 2M(m_1+E_1),$$

R_3 can also be written

$$R_3 \alpha \int dM_{12}^2 dM_{23}^2. \quad (A.26)$$

Therefore, assuming a phase-space distribution, a scattergram of M_{12}^2 vs. M_{23}^2 is uniformly populated within the prescribed kinematical limits.

The limits can be found by squaring A.24 and substituting A.17 for $\vec{P}_3^{\,2}$. This gives

$$M^2-2M(E_1+E_2)+(E_1+E_2)^2 = E_1^2-m_1^2+E_2^2-m_2^2+2\sqrt{E_1^2-m_1^2}\cdot \quad (A.27)$$

$$x\sqrt{E_2^2-m_2^2}\cos\theta \quad m_3$$

By setting $\cos\theta = 1$ and then solving for the two solutions of E_2 in terms of E_1, the kinematical limits are obtained.

APPENDIX B

THE RELATIVE DECAY RATES FOR THE $\vec{T} = 1/2$ AND $\vec{T} = 3/2$ ISOBARS

The $N^*_{1,1}$ state is given in terms of the pion and T = 3/2 isobar by

$$|N^*_{1,1}> = \sqrt{\frac{1}{2}}\,|\pi^- N^*_{3,3}> - \sqrt{\frac{1}{3}}\,|\pi^\circ N^*_{3,1}> + \sqrt{\frac{1}{6}}\,|\pi^+ N^*_{3,-1}>. \qquad (B.1)$$

Thus the decay rate for

$$N^*_{1,1} \to N^*_{3,3} + \pi^- \qquad (1)$$

is three times that for

$$N^*_{1,1} \to N^*_{3,-1} + \pi^+. \qquad (2)$$

But, since the $N^*_{3,-1}$ state can be decomposed into

$$|N^*_{3,-1}> = \sqrt{\frac{1}{3}}\,|\pi^- p> + \sqrt{\frac{2}{3}}\,|\pi^\circ n>, \qquad (B.2)$$

only one-third of the $N^*_{3,-1}$ decays are observed when the (π°, n) state is not considered. Therefore,

$$\frac{\sigma(N^*_{1,1} \to N^*_{3,3} + \pi^- \to \pi^+ + p + \pi^-)}{\sigma(N^*_{1,1} \to N^*_{3,-1} + \pi^+ \to \pi^- + p + \pi^+)} = 9/1. \qquad (B.3)$$

For the $N^*_{3,1}$, using B.2 and

$$|N^*_{3,1}> = \sqrt{\frac{2}{5}}\,|\pi^- N^*_{3,3}> + \sqrt{\frac{1}{15}}\,|\pi^\circ N^*_{3,1}> - \sqrt{\frac{8}{15}}\,|\pi^+ N^*_{3,-1}>, \qquad (B.4)$$

the ratio

$$\frac{\sigma(N^*_{3,1} \to N^*_{3,3} + \pi^- \to \pi^+ + p + \pi^-)}{\sigma(N^*_{1,1} \to N^*_{3,-1} + \pi^+ \to \pi^- + p + \pi^+)} = 9/4 \qquad (B.5)$$

is obtained very easily.

APPENDIX C

ρ^- AND ρ° PRODUCTION IN THE ONE-PION-EXCHANGE MODEL

Let it be assumed that the reactions

$$\pi^- + p \rightarrow \rho^\circ + N^* \rightarrow N^*_{3,-3} + \pi^+ \qquad (1)$$

and

$$\pi^- + p \rightarrow \rho^- + N^* \rightarrow N^*_{3,3} + \pi^- \qquad (2)$$

are governed by the one-pion-exchange diagrams of Figure 52, where N* represents any one of the $\vec{T} = 1/2$ or $3/2$ nucleon resonances.

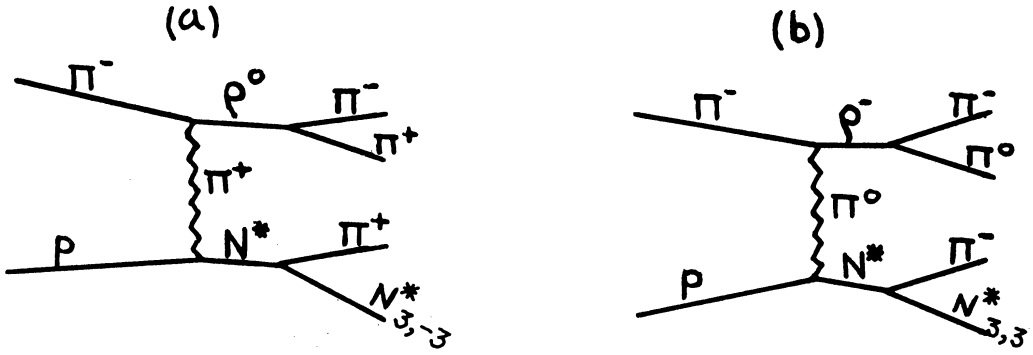

Figure 52. One-pion-exchange diagrams for reactions (1) and (2). $T_z = -1/2$ for the N* of (a) and $T_z = +1/2$ for the N* of (b). $\vec{T} = 1/2$ or $3/2$ for the N*'s in both (a) and (b).

At the upper verticies, since

$$|\pi^-\rangle = |1,-1\rangle = \frac{1}{\sqrt{2}}\left(|\pi^\circ\rho^-\rangle - |\pi^-,\rho^\circ\rangle\right), \qquad (C.1)$$

the cross sections for ρ° and ρ^- production are equal. Thus the ratio of the cross sections for reactions (1) and (2) is solely dependent on the relative rates of the processes at the lower verticies.

For the combination of a $\vec{T} = 1/2$ N* and a pion, the proton state is given by

$$|p\rangle = \left|\frac{1}{2}, \frac{1}{2}\right\rangle = \sqrt{\frac{2}{3}}\,|\pi^+ N^*_{1,-1}\rangle - \sqrt{\frac{1}{3}}\,|\pi^\circ N^*_{1,1}\rangle \qquad (C.2)$$

which immediately gives the ratio

$$\frac{\sigma(p \to \pi^+ + N^*_{1,-1})}{\sigma(p \to \pi^\circ + N^*_{1,1})} = 2. \qquad (C.3)$$

Furthermore, since the rates for

$$N^*_{1,-1} \to \pi^+ + N^*_{3,-3}$$
$$\to \pi^- + n \qquad (3)$$

and

$$N^*_{1,1} \to \pi^- + N^*_{3,3}$$
$$\to \pi^+ + p \qquad (4)$$

are equal because of charge symmetry, the cross section for

$$\pi^- + p \to \rho^\circ + N^*_{1,-1}$$
$$\to \pi^+ + N^*_{3,-3} \qquad (5)$$

is <u>twice</u> that for

$$\pi^- + p \to \rho^- + N^*_{1,1}$$
$$\to \pi^- + N^*_{3,3}. \qquad (6)$$

In terms of a $\vec{T} = 3/2$ N* and a pion, the proton state is given by

$$|p\rangle = \left|\frac{1}{2}, \frac{1}{2}\right\rangle = \sqrt{\frac{1}{2}}\,|\pi^- N^*_{3,3}\rangle - \sqrt{\frac{1}{3}}\,|\pi^\circ N^*_{3,1}\rangle + \sqrt{\frac{1}{6}}\,|\pi^+ N^*_{3,-1}\rangle. \qquad (C.4)$$

This furnishes the ratio

$$\frac{\sigma(p \to \pi^+ + N^*_{3,-1})}{\sigma(p \to \pi^\circ + N^*_{3,1})} = 1/2.$$

And finally, since the rates for

$$N^*_{3,-1} \to \pi^+ + N^*_{3,-3} \to \pi^- + n \tag{7}$$

and

$$N^*_{3,1} \to \pi^- + N^*_{3,3} \to \pi^+ + p \tag{8}$$

are equal because of charge symmetry, the cross section for

$$\pi^- + p \to \rho^\circ + N^*_{3,-1} \to \pi^+ + N^*_{3,-3} \to \pi^- + n \tag{9}$$

is <u>one-half</u> that for

$$\pi^- + p \to \rho^- + N^*_{3,1} \to \pi^- + N^*_{3,3} \to \pi^+ + p. \tag{10}$$

REFERENCES

1. H.L. Anderson, E. Fermi, E.A. Long, R. Martin, and D.E. Nagle, Phys. Rev. 85, 934 (1952).

2. M. Alston, L.W. Alvarez, P. Eberhard, M.L. Good, W. Graziano, H.K. Ticho, and S.G. Wojcicki, Phys. Rev. Letters 5, 520 (1960).

3. A.R. Erwin, R. March, W.D. Walker, and E. West, Phys. Rev. Letters 6, 628 (1961).

4. E. Pickup, D.K. Robinson, and E.O. Salant, Phys. Rev. Letters 7, 192 (1961).

5. B.C. Maglić, L.W. Alvarez, A.H. Rosenfeld, and M.L. Stevenson, Phys. Rev. Letters 7, 178 (1961).

6. N.-h. Xuong and G.R. Lynch, Phys. Rev. Letters 7, 327 (1961).

7. W.R. Frazer and J.R. Fulco, Phys. Rev. 117, 1609 (1960).

8. Y. Nambu, Phys. Rev. 106, 1366 (1957).

9. G.F. Chew, Phys. Rev. Letters 4, 142 (1960).

10. A.H. Rosenfeld, A. Barbaro-Galtieri, W.H. Barkas, P.L. Bastien, J. Kirz, and M. Roos, Revs. Modern Phys. 36, 977 (1964).

11. E. Ferrari and F. Selleri, Suppl. Nuovo Cimento 24, 453 (1962).

12. F. Selleri, Phys. Letters 3, 76 (1962).

13. L. Stodolsky and J.J. Sakurai, Phys. Rev. Letters, 11, 90 (1963).

14. J. Alitti, J.P. Buton, A. Berthelot, B. Deler, W.J. Fickinger, M. Neveu-Rene, V. Alles-Borelli, R. Gessaroli, A. Romano, and P. Waloschek, Nuovo Cimento 35, 1 (1965).

15. N. Schmitz, Nuovo Cimento 31, 255 (1964).

16. K. Gottfried and J.D. Jackson, Nuovo Cimento 33, 309 (1964).

17. K. Gottfried and J.D. Jackson, Nuovo Cimento 34, 735 (1964).

REFERENCES (Continued)

18. J.D. Jackson, J.T. Donohue, K. Gottfried, R. Keyser, and B.E.Y. Svensson, Phys. Rev. 139, B428 (1965).

19. E.E.H. Shin, Phys. Rev. Letters 10, 196 (1963).

20. L.M.Brown, Phys. Rev. Letters 13, 42 (1964).

21. M. Gell-Mann and Y.Ne'eman, The Eightfold Way (W.A. Benjamin, Inc., New York and Amsterdam, 1964).

22. R.E. Behrends, J. Dreitlein, C. Fronsdal, and W. Lee, Revs. Modern Phys. 34, 1 (1962).

23. G.M. Pjerrou, D.J. Prowse, P. Schlein, W.E. Slater, D.H. Stork, and H.K. Ticho, Phys. Rev. Letters 9, 114 (1962).

24. V.E. Barnes, P.L. Connolly, D.J. Crennell, B.B. Culwick, W.C. Delaney, W.B. Fowler, P.E. Hagerty, E.L. Hart, N. Horwitz, P.V.C. Hough, J.E. Jensen, J.K. Kopp, K.W. Lai, J. Leitner, J.L. Lloyd, G.W. London, T.W. Morris, Y. Oren, R.B. Palmer, A.G. Prodell, D. Radojičić, D.C. Rahm, C.R. Richardson, N.P. Samios, J.R. Sanford, R.P. Shutt, J.R. Smith, D.L. Stonehill, R.C. Strand, A.M. Thorndike, M.S. Webster, W.J. Willis, and S.S. Yamamoto, Phys. Rev. Letters 12, 204 (1964).

25. Y.Y. Lee, W.D.C. Moebs, B.P. Roe, D. Sinclair, and J.C. Vander Velde, Bull. Am. Phys. Soc. 8, 325 (1963).

26. Y.Y. Lee, W.D.C. Moebs, B.P. Roe, D. Sinclair, and J.C. Vander Velde, Bull. Am. Phys. Soc. 8, 325 (1963).

27. Y.Y. Lee, W.D.C. Moebs, B.P. Roe, D. Sinclair, and J.C. Vander Velde, Phys. Rev. Letters 11, 508 (1963).

28. Y.Y. Lee, B.P. Roe, D. Sinclair, and J.C. Vander Velde, Phys. Rev. Letters 12, 342 (1964).

29. Y.Y. Lee, Investigation of Di-Pion Resonances in 3.7 BeV/c π^-p Collisions (University of Michigan, Dissertation, 1964).

30. W.D.C. Moebs, B.P. Roe, D. Sinclair, and J.C. Vander Velde, "Proceedings of the International Conference on High Energy Physics," Dubna, 1964 (to be published).

31. M.L. Perl, Y.Y. Lee, and E. Marquit, Phys. Rev. 138, B707 (1965).

REFERENCES (Continued)

32. G.F. Chew and F.E. Low, Phys. Rev. 113, 1640 (1959).

33. N.P. Samios, A.H. Bachman, R.M. Lea, T.E. Kalogeropoulos, and W.D. Shephard, Phys. Rev. Letters 9, 139 (1962).

34. C. Alff, D. Berley, D. Colley, N. Gelfand, U. Nauenberg, D. Miller, J. Schultz, J. Steinberger, T.H. Tan, H. Brugger, P. Kramer, and R. Plano, Phys. Rev. Letters 9, 322 (1962).

35. P.H. Satterblom, W.D. Walker, and A.R. Erwin, Phys. Rev. 134, B207 (1964).

36. Aachen-Birmingham-Bonn-Hamburg-London (I.C.)-Munchen Collaboration, Nuovo Cimento 31, 485 (1964).

37. Aachen-Berlin-Birmingham-Bonn-Hamburg-London(I.C.)-Munchen Collaboration, Phys. Rev. 138, B897 (1965).

38. R.L. Lander, W. Mehlhop, N.-h. Xuong, and P.M. Yager, "Production of Nucleon Isobar and Multipion Resonances by 3.5 BeV/c π^+ in Hydrogen," Report to the Ohio University Topical Conference on Recently Discovered Resonance Particles, April 26-27, 1963.

39. W.F. Baker, R.L. Cool, E.W. Jenkins, T.F. Kycia, S.S. Lindenbaum, W.A. Love, D. Luers, J.A. Niederer, S. Ozaki, A.L. Read, J.J. Russell, and C.L. Yuan, Phys. Rev. Letters 7, 101 (1961).

40. G. Benson (Private Communication).

41. J.R. Sanford, "The Separated Beam to the 20-Inch Bubble Chamber at the AGS" (BNL Internal Report, 1962).

42. E. Hart, BNL-BCG Internal Report J-22 (1962).

43. R. Rau, BNL-BCG Internal Report J-18 (1961).

44. J.C. Vander Velde, University of Michigan Bubble Chamber Group Research Notes HI-1 and HI-3 (1963).

45. W.E. Humphrey and A.H. Rosenfeld, "Analysis of Bubble Chamber Data," UCRL-10812 (1963).

46. J. Berge, F. Solmitz, and H. Taft, Rev. of Sci. Instr. 32, 538 (1961).

REFERENCES (Continued)

47. W.J. Willis, E.C. Fowler, and D.C. Rahm, Phys. Rev. 108, 1046 (1957).

48. D.M. Ritson, Techniques of High Energy Physics (Interscience Publishers, Inc., New York, 1961), p. 108.

49. J. Orear, "Notes on Statistics for Physicists," UCRL 8417 (1958).

50. A. Diddens, E. Jenkins, T. Kycia, and K. Riley, Phys. Rev. Letters 10, 262 (1962).

51. R.P. Feynam, Theory of Fundamental Processes (W.A. Benjamin, Inc., New York, 1962) p. 73.

52. N.-h. Xuong, R.L. Lander, W.A.W. Mehlhop, and P.M. Yager, Phys. Rev. Letters 11, 227 (1963).

53. S.B. Trieman and C.N. Yang, Phys. Rev. Letters 8, 140 (1962).

54. P. Pennock, Tuborg Subprogram (ANL Internal Report).

55. P. Pennock, Tribod Subprogram (ANL Internal Report).

56. G. Lütjens and J. Steinberger, Phys. Rev. Letters 12, 517 (1964).

57. W.J. Fickinger, D.K. Robinson, and E.O. Salant, Phys. Rev. Letters 10, 457 (1963).

58. L. Durand, III, and Y.T. Chiu, Phys. Rev. Letters 14, 1039 (1965).

59. G. Goldhaber, J.L. Brown, S. Goldhaber, J.A. Kadyk, B.C. Shen, and G.H. Trilling, Phys. Rev. Letters 12, 336 (1964).

60. S.U. Chung, O.I. Dahl, L.M. Hardy, R.I. Hess, G.R. Kalbfleisch, J. Kirz, D.H. Miller, and G.A. Smith, Phys. Rev. Letters 12, 621 (1964).

61. J. Alitti, J.B. Buton, B. Delei, M. Neveu-René, J. Crussard, J. Gineset, A.H. Tran, R. Gessaroli, and A. Romano, Phys. Letters 15, 69 (1965).

62. R.T. Deck, Phys. Rev. Letters 13, 169 (1964).

63. F. Salzman and G. Salzman, Phys. Rev. 120, 599 (1960).

64. M. Gell-Mann and K.M. Watson, Ann. Rev. Nucl. Sci. 4, 219 (1954).

REFERENCES (Concluded)

65. E. Ferrari and F. Selleri, Nuovo Cimento 27, 1450 (1963).

66. D.D. Carmony, D.N. Hoa, R.L. Lander, P.M. Yager, and N.-h. Xuong, "The T = 2 Pion-Pion Interaction" (Physics Dept., University of California at San Diego, April 24, 1964).

67. M.L. Stevenson, L.W. Alvarez, B.C. Maglic, and A.H. Rosenfeld, Phys. Rev. 125, 687 (1962).

68. M. Abolins, R.L. Lander, W.W. Mehlhop, N.-h. Xuong, and P.M. Yager, Phys. Rev. Letters 11, 381 (1963).

69. G. Goldhaber, S. Goldhaber, J.A. Kadyk, and B.C. Shen, Phys. Rev. Letters 15, 118 (1965).

70. P. Schlein, W.E. Slater, L.T. Smith, D.H. Stork, and H.K. Ticho, Phys. Rev. Letters 10, 368 (1963).

71. P.L. Connolly, E.L. Hart, K.W. Lai, G. London, G.C. Moneti, R.R. Rau, N.P. Samios, I.O. Skillicorn, S.S. Yamamoto, M. Goldberg, M. Gundzik, J. Leitner, and S. Lichtman, Phys. Rev. Letters 10, 371 (1963).

72. S.L. Glashow, Phys. Rev. Letters 11, 48 (1963).

73. R. Hagedorn, Relativistic Kinematics (W.A. Benjamin, Inc., New York, 1962) p. 93.

74. T.E. Kalogeropoulos, LIMS (BNL Internal Report F. 89).

75. G. Moneti, DALPS (BNL Internal Report F. 96).